2008

Development and application of a hybrid femtosecond/picosecond coherent Raman probe designed for study of excited state systems

Benjamin Douglas Prince
Iowa State University

Development and application of a hybrid femtosecond/picosecond coherent Raman probe designed for study of excited state systems

by

Benjamin Douglas Prince

A dissertation submitted to the graduate faculty

in partial fulfillment of the requirements for the degree of

DOCTOR OF PHILOSOPHY

Major: Physical Chemistry

Program of Study Committee:
Hans U. Stauffer, Major Professor
Mark Gordon
William Jenks
Victor Lin
Xueyu Song

Iowa State University

Ames, Iowa

2008

TABLE OF CONTENTS

ABSTRACT

The conversion from purely femtosecond coherent anti-Stokes Raman spectroscopy (CARS) to a more advantageous hybrid femtosecond/picosecond CARS (fs/ps CARS) probe for time-resolved vibrational dynamics studies is detailed. This probe provides a number of benefits for the use of studying the evolution of electronically excited states, including rapid data acquisition speeds, increased spectral resolution, and discrimination against competing background signals. The high time resolution is shown to depend on the cross correlation of the excitation pulse and initial CARS pulses while the high frequency resolution is shown to depend on the final CARS electric field. The pump-fs/ps CARS probe technique is applied to study the dynamics of several excited state systems, including coumarin 153, where it was shown that complex dynamics exist between hydrogen bonded and non-hydrogen bonded species. Additionally, the complex behavior of the excited state vibrational evolution during solvation is explored. Finally, fs/ps CARS was used to probe the ground and excited state structures of N,N-dimethyl-*p*-nitroaniline to study the effects of the charge transfer character on the ground and excited state molecular structure as well as the relaxation process after internal conversion.

CHAPTER 1: INTRODUCTION

1.1 General Overview

Vibrational spectroscopies have been used to understand molecular structure, structural changes upon perturbation, local solvent environments, and chemical identification throughout the 20th century up to the present. The development of tunable infrared and visible lasers has only broadened the use of these spectroscopies to solve chemically relevant questions. With increasing technology, the laser sources used for these experiments have become increasingly shorter in duration for the use of understanding short-lived phenomena in molecules. These phenomena include chemically relevant processes[4-5] such as charge transfer in conducting polymers or simple organic conjugated species[6,12], keto-enol isomerization[7-8], excited state structural changes[9-11], and excited state relaxation pathways[13].

These newer laser sources have set into motion an amazing amount of experimental work utilizing non-linear spectroscopies (non-linear, in this case, means the use of more than one incident photon on the sample) including the one most discussed in this thesis, coherent anti-Stokes Raman spectroscopy (CARS). CARS has been utilized in the frequency domain via nanosecond (ns) and picosecond (ps)[14-20] laser sources as well as in the time domain using femtosecond (fs) laser sources[21-23]. It has been used primarily as a Raman spectroscopic technique to study relaxed systems (ground electronic state) although has been employed in some cases to the study of excited electronic states under certain conditions.

As quantum mechanical and semi-empirical calculations have done much to aid the assignment of peaks and understanding of dynamics in chemical systems, a fair amount of calculation has also been included where it seems most applicable to the understanding of the

systems under study. In some cases, calculations serve to make us aware of what changes molecules are not undergoing as much as what changes they are.

1.2. Thesis Organization

This thesis is concerned with the development, refinement, and applications of a Raman active vibrational spectroscopy that has been termed fs/ps CARS (or alternatively "fast-pass" CARS). The second chapter is adapted from the first paper published using this technique. It discusses the actual implementation and general experimental techniques behind fs/ps CARS. The third chapter involves currently unpublished material to address time resolution and frequency resolution questions that relate to the use of the technique to study excited state dynamics. The fourth chapter is from submitted material which discusses the excited state Raman spectra of a model dye molecule, coumarin 153 (C153). The particular emphasis is on the use of the technique to study hydrogen bonding in the excited state. The fifth chapter is unpublished material discussing the CARS excited state intensity dynamics of C153, coumarin 35, and coumarin 102 with respect to the input of excess energy and comparison to electronic pump-probe studies. The sixth chapter is adapted from submitted material and discusses the excited state dynamics as well as ground and excited state structures of N,N-dimethyl-*p*-nitroaniline (DMPNA) in the condensed phase.

1.3 Theoretical Background

Before beginning a discussion on the theoretical underpinnings of four wave mixing techniques, it seems prudent to acknowledge the breadth of work applied by others into making the entire theory understandable. Because this author is not a theorist by trade and

there is no need to rehash detail by detail the work of others in this advancement of the theory behind four wave mixing, many of the presented equations are the result of others' work after their labor and application of simplifications to prevent the important information from being spread into pages upon pages for one simple equation. Much of this discussion follows the formalism used by Mukamel.[1] These general equations will be discussed with respect to their applications to the present work, and are generally adapted from reference 1.

CARS is an example of a four-wave mixing process in which three input electromagnetic fields interact with matter to output a fourth wave in a specific direction. The intensity (I_{CARS}) of this output wave is a function of several parameters and governed by the following equations:

$$I_{CARS} \propto \left|P^{(3)}(t)\right|^2 \tag{1.1}$$

$$P^{(3)} \propto \chi^{(3)} E_1(t) E_2(t) E_3(t) \tag{1.2}$$

where $P^{(3)}$ is the third order polarization which is related to the molecule by use of $\chi^{(3)}$ which is the third order susceptibility of the molecule. The $E_x(t)$ are time dependent electric fields of the form

$$E(\vec{r},t) = E(t)e^{i\vec{k}\vec{r} - i\omega t} + c.c \tag{1.3}$$

where the vector **k** defines the direction of the electric field, ω the frequency and E(t) the envelope of the pulse.

The third order susceptibility is a molecular specific term that contains information about the transition dipoles of various potential transitions after interaction with the electric fields and generally has the form[1] where the first summation addresses the different potential time orderings of the electric fields.

$$\chi^{(3)} \propto \sum_{\substack{each\\ time\\ order}} \sum_{a,b,c,d} P(a)\mu_{ab}\mu_{bc}\mu_{cd}\mu_{da} \begin{bmatrix} I_{dc}(\omega_1-\omega_2+\omega_3)I_{db}(\omega_1-\omega_2)I_{da}(\omega_1)+ \\ I_{dc}(\omega_1-\omega_2+\omega_3)I_{db}(\omega_1-\omega_2)I_{ab}(\omega_1)+ \\ I_{dc}(\omega_1-\omega_2+\omega_3)I_{ac}(\omega_1-\omega_2)I_{ab}(\omega_1)+ \\ I_{ba}(\omega_1-\omega_2+\omega_3)I_{ca}(\omega_1-\omega_2)I_{da}(\omega_1)- \\ I_{cb}(\omega_1-\omega_2+\omega_3)I_{db}(\omega_1-\omega_2)I_{ab}(\omega_1)- \\ I_{cb}(\omega_1-\omega_2+\omega_3)I_{db}(\omega_1-\omega_2)I_{da}(\omega_1)- \\ I_{cb}(\omega_1-\omega_2+\omega_3)I_{ca}(\omega_1-\omega_2)I_{da}(\omega_1)- \\ I_{ad}(\omega_1-\omega_2+\omega_3)I_{ac}(\omega_1-\omega_2)I_{ab}(\omega_1) \end{bmatrix} \tag{1.4}$$

where the variables a, b, c and d represent molecular eigenstates, μ_{ij} represents transition dipoles between eigenstates, $I_{ij}(\omega)$ represent complex Lorentzian lineshapes associated with frequency dependent contribution to the third order molecular susceptibility ($\chi^{(3)}$), and P(a) represents the probability of the a^{th} state being occupied. These complex lineshapes ($I_{ij}(\omega)$) have the form:

$$I_{vv'}(\omega) = \frac{1}{\omega - \omega_{vv'} + i\Gamma_{vv'}} \tag{1.5}$$

In general, only a subset of molecular states contribute to the frequency-dependent third order susceptibility. Therefore, this response can be simplified by looking at pictorial representations developed to make the actual four wave mixing process considerably simpler. A density matrix approach was developed which simplifies the transitions into a single change in bra or ket for each electric field interaction. Under this approach, the only requirement is that the bra and ket states end at the same final state. There can be pure ket evolution, pure bra evolution as well as combinations of the two, so long as they end at the same final state. There is no actual requirement that each state is real and instead can be a "virtual state" which can be thought of as an extremely fast dephasing state which only exists

during the duration of the electric field populating it. Pure ket evolution follows the path from initial state |a><a| to |d><a| after first field interaction to |c><a| after the second interaction and |b><a| after the third interaction and the fourth field returns the bra and ket to |a><a| in this case. Pure bra evolution follows the pattern a → b → c → d on the bra side of the notation.

To apply molecularly relevant states and the time ordering of the pulses employed in a scheme, a common method of portraying the density matrix evolution is through the use of ladder diagrams[3]. An example ladder diagram for a few different four wave mixing schemes is shown in figure 1.1. Ladder diagrams provide a useful tool to understanding both the directionality of the signal but also the relative energetics of each individual outputted 4WM signal. In the ladder diagrams a solid vertical line is used to denote a ket evolution, and if the transition is with an upward arrow, the electric field k vector is acting in a positive fashion, where as a solid line downward transition has the electric field acting in a –k fashion. The dashed lines are used to denote bra evolutions and have the upward and downward fashion k vectors reversed (i.e. bra down is +k, bra up is –k). The energetics of the scheme are determined in the same fashion. In the case of the left side of the figure, we have $k_{FWM} = k_1 - k_2 + k_3$ which results in signal $\omega_{FWM} = \omega_1 - \omega_2 + \omega_3$ (this is the CARS signal in cases where $\omega_1 > \omega_2$. The right hand side has $k_{FWM} = -k_1 + k_2 + k_3$ and has signal $\omega_{FWM} = -\omega_1 + \omega_2 + \omega_3$.

By separating the three input lasers into some fixed input geometry, one can pre-determine where all possible FWM signals will be found. Selecting to detect one component (via their respective k_{FWM} vectors) allows exact knowledge of the possible energetic orderings of the outputted signal in that direction and consequently the real vibrational states that could scatter light in that direction.

The lineshapes of the obtained signal in the frequency domain for CARS signal are determined by the relationship between two molecular quantities and follow the following equation[1]

$$S_{CARS}(\omega_1 - \omega_2) = \left| \sum_{a,c} [P(a) - P(c)] \frac{|\alpha_{ac}|}{\omega_1 - \omega_2 - \omega_{ca} + i\Gamma_{ca}} \right|^2 \qquad (1.6)$$

P(a) and P(c) are the probability of a state a or c being occupied and α_{ac} collects transition dipoles associated with the three pulse CARS sequence. The denominator states that signal will only strongly exist in the case of vibrationally resonant CARS signal when $\omega_{CA} = \omega_1 - \omega_2$ where ω_{CA} are the real vibrational mode frequencies of the chemical under study. The intensity obtained is a function of the strength of the transition dipoles, μ via the numerator term, and in the absence of the dephasing rate, Γ, would have infinite narrowness. Γ then becomes an important measurable quantity because it contains information about the relaxation and dephasing time of the vibrational modes which detail how efficiently energy flows out of the mode. If it can be assumed that each solvent environment affects each solute molecule in an identical fashion, the molecules under study undergo homogenous broadening which has a precise relationship in the frequency and time domain via a Fourier transform. The result of this type of pure homogeneous broadening is a Lorentzian lineshape in the frequency domain with 2Γ related to $\Gamma = (\tau_{decay})^{-1}$ in $\exp(-t/\tau_{decay})$ in the time domain. This relationship is only exact in the case of pure homogenous broadening and continuous wave beams. Differences in the relationship between Γ and the measured fs/ps CARS linewidths will be further addressed in this thesis. Alternative lineshapes also exist, which for the results discussed in this thesis can be limited to the case of inhomogeneous broadening and

its consequential Gaussian lineshape. Gaussian lineshapes are a result of having a collection of molecules each with a unique set of observable frequencies that form a bell shaped distribution. Typically these frequencies do not have identical time-domain decays and thus cannot be fit easily to a single exponential timescale. Typical forms of Gaussian lineshapes follow this relationship:

$$I(\omega) = Ae^{\left(-\left(\frac{\omega-\omega_0}{2\sigma^2}\right)^2\right)} \qquad (1.7)$$

where A is the intensity, ω_0 is the central frequency of the vibrational mode, and σ is the standard deviation of the normalized probability distribution which is used to define the full width at half max of:

$$FWHM = 2\sqrt{2\ln 2}\sigma \qquad (1.8)$$

Vibrational linewidths can be useful in helping to determine electronically excited state lifetimes for systems that undergo rapid relaxation because vibrational mode lifetimes in the excited state are often tied directly into the electronic dephasing time of the excited potential. The time-energy uncertainty principle states that:

$$\Delta E \Delta t \geq \frac{\hbar}{2} \qquad (1.9)$$

Thus, the uncertainty in energy, full width at half maximum, can be used to predict the minimum lifetime in the time domain of both the vibrational and electronic states.

1.4 References

1. S. Mukamel, *Principles of Nonlinear Optical Spectroscopy*, Oxford University Press, **1995**, p 149-159 and 419.

2. J. L. McHale. *Molecular Spectroscopy*, Prentice Hall, *1st ed*., **1999**.

3. Lee, D. and A.C. Albrecht, *Advances in Infrared and Raman Spectroscopy;* Clark, R. J. H. and R. E. Hester, Eds., Wiley: New York, 1985, vol 12.

4. *Ultrafast Infrared and Raman Spectroscopy*, M. D. Fayer ed., Marcel Dekker: New York, 2001.

5. J. C. Wright, *Int. Reviews in Physical Chemistry*, 2002, **21**(2), p. 185-255.

6. Grabowski, Z. R.; Rotkiewicz, K. and W. Rettig, *Chem. Rev.*, 2003, **103**(10), p. 3899-4031.

7. Rine, M.; Kummrow, A.; Dreyer, J.; Nibbering, E.T.J. and T. Elsaesser, *Faraday Discussions*, 2003, **122**, p. 27-40.

8. Poor, B.; Michniewicz, N.; Kallay, M.; Buma, W. J.; Kubinyi, M.; Szemik-Hojniak, A.; Deperasinska, I.; Puszko, A. and H. Zhang, *J. Phys. Chem. A,* 2006, **110**, p. 7086-7091.

9. A. M. Moran and A. M. Kelley, *J. Chem. Phys.*, 2001, **115**(2), p. 912.

10. E. T. J. Nibbering and T. Elsaesser, *Chem. Rev.*, 2004, **104**, p. 1887-1914.

11. Albrecht, M.; Bohne, C.; Granzhan, A.; Ihmels, H.; Pace, T. C. S.; Schurpfeil, A. Waidelich, M. and C. Yibwa, *J. Phys. Chem. A*, 2007, **111**, p. 1036.

12. M. Dekhtyar and W. Rettig, *J. Phys. Chem. A.*, 2007, **111**, p. 2035-2039.

13. T. Elsaesser and W. Kaiser, *Annu. Rev.*, 1991, **42**, p. 83-107.

14. Popp, A.; Ujj, L. and G. H. Atkinson, *PNAS*, 1996, **93**(1), p. 372.

15. Toich, A. M.; Melton, D. W. and W. B. Roh, *Optics Communications*, 1985, **55**(6), p. 406-408.

16. Heinrich, C.; Meusburger, C.; Bernet, S. and M. Ritsch-Marte, *J. Raman Spec.*, 2006, **37**(6), p. 675-679.

17. W. Kiefer, *J. Raman Spec.*, 2007, **38**(12), p. 1538-1553.

18. Masiello, T.; Vulpanovici, N.; Barber, J.; Chrysostom, E. T. H.; Nibler, J. W.; Maki, A.; Blake, T. A.; Sams, R. L. and A. Weber, *J. Mol. Struct.*, 2004, **227**(1), p. 50-59.

19. Huisken, F.; Ramonat, L.; Santos, J; Smirnov, W.; Stelmakh, O. M.; and A. A. Vigasin, *J. Mol. Struct.*, 1997, **410**, p. 47-50.

20. Oberle, J.; Abraham, E.; Ivanov, A.; Jonusauskas, G. and Rulliere, C., *J. Photochem. Photobiol. A.,* 1997, **105**(2-3), p. 217-223.

21. Dantus, M.; Bowman, R. M. and A. H. Zewail, *Nature*, 1990, **343**(6260), p. 737-739.

22. Dantus, M. and W. Lozovoy, *Chem. Rev.*, 2004, **104**(4), p. 1813-1859.

23. Scmitt, M.; Heid, M.; Schlucker, S. and W. Kiefer, *Biopolymers*, 2002, **67**(4-5), p. 226-232.

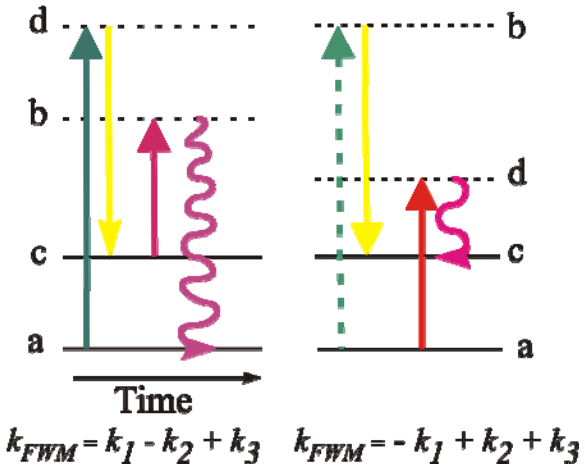

Figure 1.1: Example ladder diagrams for two different four wave mixing processes. In these diagrams, dashed horizontal lines denote "virtual" states while solid horizontal lines denote resonant (either vibrational or electronic) states. Solid lines denote ket transitions while dashed denote bra transitions (see text). The pulse ordering in time is read from left to right with the left most pulse interacting first and the right hand side interacting last. Scatter beams are shown by curved vertical lines. The only requirements in these diagrams are that all pulses are accounted for and that the final ket and bra states match. The k vector directions are determined by the transition type (bra or ket) and whether the arrow points down or up (see text).

CHAPTER 2: DEVELOPMENT OF SIMULTANEOUS FREQUENCY AND TIME RESOLVED COHERENT ANTI-STOKES RAMAN SCATTERING FOR ULTRAFAST DETECTION OF MOLECULAR SPECTRA

Benjamin D. Prince, Abhijit Chakraborty, Beth M. Prince, and Hans U. Stauffer

A paper published in the *Journal of Chemical Physics*

2.1 Abstract

The development of a time-resolved coherent anti-Stokes Raman scattering (CARS) variant for use as a probe of excited electronic state Raman-active modes following excitation with an ultrafast pump pulse is detailed. Application of this technique involves a combination of broadband fs-timescale pulses and a narrowband pulse of ps duration that allows multiplexed detection of the CARS signal, permitting direct observation of molecular Raman frequencies and intensities with time resolution dictated by the broadband pulses. Thus, this nonlinear optical probe, designated fs/ps CARS, is suitable for observation of Raman spectral evolution following excitation with a pump pulse. Because of the spatial separation of the CARS output signal relative to the three input beams inherent in a folded BOXCARS arrangement, this technique is particularly amenable to probing low-frequency vibrational modes, which play a significant role in accepting vibrational energy during intramolecular vibrational energy redistribution within electronically excited states. Additionally, this spatial separation allows discrimination against strong fluorescence signal, as demonstrated in the case of rhodamine 6G

2.2 Introduction

Recent experimental developments have made it possible to detect the temporal dynamics of vibrational energy flow in the condensed phase on increasingly fast timescales. For example, infrared transient absorption spectroscopy and the related terahertz spectroscopy[1,2] have recently been used as tools to probe the time evolution of molecular vibrational levels in electronically excited states with sub-picosecond time resolution and vibrational resolution limited predominantly by detector resolution.[3-5] Such approaches provide a wealth of information previously unavailable on these short timescales; however, they are often difficult to implement given the challenges of producing and detecting infrared radiation in the vibrational fingerprint spectral region and at lower frequencies.

The complementary Raman techniques have not evolved as quickly,[5] due predominantly to the inherent time-energy uncertainty associated with subpicosecond pulses. Thus, spontaneous Raman and resonant Raman probe techniques with sufficient resolution (~15 cm^{-1}) to reasonably distinguish vibrational modes of interest have an inherent temporal resolution limit of ~1 ps,[6-8] and more complex experimental configurations are necessary to exceed this time-energy uncertainty limit. However, recent development of the femtosecond stimulated Raman scattering (FSRS) technique by Mathies and coworkers,[9-13] along with its precursors,[14-16] have begun to allow spectrally resolved studies of the 600 – 2000 cm^{-1} region of the Raman spectrum with ~100 fs resolution.

An alternative approach to this FSRS technique involves the use of time-resolved coherent anti-Stokes Raman scattering (tr-CARS) as a subpicosecond probe of excited state vibrational evolution following electronic excitation. This and related degenerate four wave mixing (DFWM) spectroscopies have been used in several pump-CARS experimental

schemes to probe short-time evolution of both solute[17-25] and solvent[26] following solute electronic excitation. The CARS method typically involves three broadband input pulses: a pump pulse with frequency ω_1, a Stokes pulse with frequency ω_2, and a probe pulse with frequency ω_3 (the pump and probe pulse frequencies are typically degenerate, although this is not a necessary condition). The coherences created by the temporally overlapped ω_1 and ω_2 pulses are thus probed with the broadband ω_3 pulse as a function of time delay. One well-acknowledged advantage of the CARS technique is the background-free nature of signal detection afforded by the phase-matching conditions associated with the third-order polarization.[27] The spatial separation of signal beam from the three input pulses allows detection of signal free of background fluorescence and input beam scatter that often hinders Raman spectral detection.[28]

Here, we introduce a variant of tr-CARS, deemed fs/ps CARS, that allows multiplexed detection of the Raman active modes observable with CARS techniques, while maintaining the ultrafast time resolution necessary to use fs/ps CARS as a simultaneously time- and frequency-resolved probe of vibrational evolution following electronic excitation. This method involves the replacement of the scanning, broadband ω_3 pulse typically associated with tr-CARS and related FWM detection schemes with a narrowband pulse, which alleviates the need to deduce Raman frequencies from measured quantum beats.

In this paper, following a brief description of the experimental layout and the theoretical basis for the time- and frequency-resolved CARS signal described here, we demonstrate the use of the fs/ps CARS technique to provide a spectrally resolved probe of Raman-active vibrations while maintaining temporal resolution that will allow this technique to be used as a sub-100 fs Raman probe. We will first present results of neat toluene,

comparing this technique to the conventional tr-CARS technique. This is followed by results involving resonant excitation of a fluorescent laser dye, rhodamine 6G (R6G), and concluded by demonstrating the utility of this method in probing low frequency modes, as demonstrated in neat chloroform.

2.3 Experiment

2.3.1 Experimental Setup

All experiments described herein have been carried out using a Ti:sapphire oscillator (KMLabs)/amplifier (Spectra Physics Spitfire-HPR) system running at a 1 kHz repetition rate, with an output of 2.1 mJ/pulse centered at 795 nm and a duration of 50-60 fs, as determined by autocorrelation. As shown schematically in Fig. 2.1, approximately 1 mJ is split off to pump an optical parametric amplifier (OPA, Spectra Physics OPA-800CF), which produces both signal (ω_s) and idler (ω_i) pulses via parametric downconversion of the input pump (ω_p) pulse. These two beams are each subsequently mixed in nonlinear crystals (β-BBO) with replicate paths of the pump beam, split off from the residual 1.1 mJ, to produce visible pulses at frequencies $\omega_1 = \omega_p + \omega_s$ and $\omega_2 = \omega_p + \omega_i$. In general, pulse 1 is tunable from ~480 nm to 532 nm and pulse 2 is tunable from 532 nm to ~600 nm. The bandwidths of these visible pulses are typically 300-600 cm^{-1}.

The remainder (450 μJ) of the 795 nm pulse, which is ultimately used as the CARS probe pulse, ω_3, is directed into a 4*f* pulse shaping configuration,[29] equipped with a pair of holographic reflective gratings (1800 l/mm) and a pair of 100.0 mm f.l. cylindrical lenses. A variable-width slit is placed in the focal plane of the pulse shaper to allow continuous adjustment of the pulse 3 bandwidth from <1 nm (~15 cm^{-1}) to its full spectral bandwidth

(~350 cm^{-1}, FWHM). The delay of pulse 3 is scanned relative to those of pulses 1 and 2 by a computer-controlled translation stage (Physik Instrumente M-505.4DG).

All three beams are directed into a sample cell, following reflection off a concave enhanced aluminum mirror (635 mm f.l.), using a folded BOXCARS input configuration.[28,30] Typical pulse powers used in all experiments range from 3 μJ/pulse to 8 μJ/pulse with beam diameters of ~ 250 μm at the interaction region. Samples were placed either in a static 1.0 mm pathlength quartz cuvette (Starna Cells) or in the 1.0 mm gap between two fused silica windows of a motorized rotating cell that allows complete sample refreshment in the laser interaction volume after each amplifier pulse; no significant differences were observed using either sample configuration.

The CARS signal arising in the $\mathbf{k}_{\mathbf{CARS}} = \mathbf{k}_1 - \mathbf{k}_2 + \mathbf{k}_3$ phase-matching direction is spatially filtered via iris and focused into a spectrometer (Ocean Optics USB-2000), which allows spectral dispersion with a resolution of 0.7 nm (~14 cm^{-1} resolution near the ω_{CARS} frequency). Note that ω_1 and ω_3 differ in these experiments, in contrast to conventional CARS spectroscopy, in which the pump and probe beams are typically degenerate. The three-color method employed here allows detection of ω_{CARS} in a spectral region (700 - 800 nm, depending on (ω_1 - ω_2) energy) that provides improved resolution. In an alternative detection scheme used to generate spectrally integrated data as a function of probe delay, the CARS signal is focused onto a Si photodiode detector (Thorlabs DET210) and isolated using a lock-in amplifier (Stanford Research Systems SR810). This lock-in amplifier is triggered at the 500 Hz frequency associated with an optical chopper, synchronized to the amplifier repetition rate, modulating input beam 1. In this integrated signal scheme, additional optical

filters (650 nm long pass and 750 nm short pass) are placed in the path of the detected signal beam to allow further discrimination against the three input beams.

Three samples were studied in these experiments and were used as purchased without further purification. Rhodamine 6G (Acros Organics, 99% purity) was dissolved in spectroscopic grade methanol to a concentration of 8 mM. Toluene (Fisher Scientific, 99.8%) and chloroform (Fisher Scientific, 99.9%) were used without dilution (*i.e.*, neat).

While the relative polarizations of the three input beams are known to play an important role in the degree of non-resonant (*i.e.*, electronic) contribution to the time-resolved CARS signal,[31,32] polarization dependence studies are beyond the scope of these initial experiments; instead, all input beam polarizations were maintained as parallel, and no polarization selectivity was used in ω_{CARS} detection.

2.3.2 Numerical Simulations

To treat the time-resolved nature of the CARS process numerically, we begin by assuming sample interaction with three pulses having complex electric field envelopes, $\varepsilon_j(t)$, (j = 1,2,3), and corresponding frequencies, ω_j. Thus, the external electric field takes the form

$$E(\mathbf{r},t) = \varepsilon_1(t+\tau_{23}+\tau_{12})\exp(i\mathbf{k}_1\cdot\mathbf{r}-i\omega_1 t) + \varepsilon_2(t+\tau_{23})\exp(i\mathbf{k}_2\cdot\mathbf{r}-i\omega_2 t) + \varepsilon_3(t)\exp(i\mathbf{k}_3\cdot\mathbf{r}-i\omega_3 t) + c.c. \quad [1].$$

Each electric field, $\varepsilon_j(t)$, is assumed to be centered about $t = 0$; therefore, the time delays τ_{23} and τ_{12} correspond, respectively, to the delays between pulses 2 and 3 and pulses 1 and 2. The third order polarization arising from an interaction of the sample with this electric field,

detected in the phase-matching-defined direction, $\mathbf{k}_{\mathbf{CARS}} = \mathbf{k}_{\mathbf{1}} - \mathbf{k}_{\mathbf{2}} + \mathbf{k}_{\mathbf{3}}$, under the rotating wave approximation (RWA),[27] is

$$P^{(3)}(t,\tau_{23},\tau_{12}) = \frac{-i}{\hbar^3}\int_{-\infty}^{t} d\alpha_3 \int_{-\infty}^{\alpha_3} d\alpha_2 \int_{-\infty}^{\alpha_2} d\alpha_1 R_4(t-\alpha_3,\alpha_3-\alpha_2,\alpha_2-\alpha_1)$$
$$\times \varepsilon_3(\alpha_3)\varepsilon_2^*(\alpha_2+\tau_{23})\varepsilon_1(\alpha_1+\tau_{23}+\tau_{12})e^{-i\omega_3\alpha_3}e^{+i\omega_2\alpha_2}e^{-i\omega_1\alpha_1}e^{i(\omega_3-\omega_2+\omega_1)t} \quad [2],$$

where the relevant response function, $R_4(t_3, t_2, t_1)$, has been treated phenomenologically, with each Raman active vibrational level assigned a central frequency and homogeneously-broadened lifetime.[33] For delays τ_{23} long with respect to the durations of pulses 1 and 2, these electric fields can be replaced by δ-functions, resulting in a simplified polarization expression,

$$P^{(3)}(t,\tau_{23},\tau_{12}) = \frac{-i}{\hbar^3}e^{i(\omega_1-\omega_2+\omega_3)t}e^{i(\omega_1-\omega_2)\tau_{23}}e^{i\omega_1\tau_{12}}$$
$$\times \int_{-\infty}^{t} d\alpha_3 R_4(t-\alpha_3,\alpha_3+\tau_{23},\tau_{12})\varepsilon_3(\alpha_3)e^{-i\omega_3\alpha_3} \quad [3].$$

Fourier transformation of this time-dependent polarization with respect to t allows determination of the spectral dependence of the third order polarization, $P^{(3)}(\omega_{CARS},\tau_{23},\tau_{12})$. The detected ω_{CARS} signal, measured at the intensity (rather than the field) level in this homodyned experimental scheme, is proportional to the squared magnitude of this third order polarization.[27] In all simulations described here, τ_{12} was set to zero to match experimental conditions.

2.4 Results and Discussion

2.4.1 Non-resonant CARS: toluene

2.4.1.1 Conventional tr-CARS

Neat toluene was used as a preliminary sample due both to its relative simplicity in the fingerprint region of the Raman spectrum (800 cm^{-1} – 1400 cm^{-1}) as well as its use as an ASTM standard for Raman spectroscopic calibration.[34] Since pulses 1 and 2 are produced by upconversion of the signal and idler outputs from a single OPA, energetic restrictions are placed on the frequencies ω_1 and ω_2. In the case of toluene, pulse 1 is centered at 517 nm (FWHM ~ 250 cm^{-1}) and pulse 2 is centered at 545 nm (FWHM ~ 300 cm^{-1}) to allow access at (ω_1 - ω_2) to the ~1000 cm^{-1} spectral range via non-resonant CARS.

Initially, studies of neat toluene were carried out using conventional tr-CARS, in which the time delay, τ_{23}, of broadband pulse 3 is scanned with respect to the temporally overlapped pulses 1 and 2 (τ_{12} = 0). The total (integrated) ω_{CARS} signal observed as a function of τ_{23} (Fig. 2.2a) shows evidence for decaying beats resulting from the underdamped vibrational coherences prepared by interaction of ω_1 and ω_2 with the sample. The inset of Fig. 2a shows these beat frequencies, determined by Fourier transform (FT), following subtraction of the exponentially decaying backbone associated with this ω_{CARS} signal. Two major beat frequencies at 26.9 cm^{-1} and 216.2 cm^{-1} are evident from this spectrally integrated ω_{CARS} signal. Four Raman active modes are known to be present in this region with frequencies 786.5 cm^{-1}, 1003.6 cm^{-1}, 1030.6 cm^{-1}, and 1211.4 cm^{-1};[34] thus, the 26.9 cm^{-1} beat

is readily assigned to a coherence between the 1003.6 cm^{-1} and 1030.6 cm^{-1} modes, whereas some ambiguity exists in the assignment of the 216.2 cm^{-1} beat.

Spectral dispersion of this tr-CARS signal allows a more complete assignment of these quantum beats to specific regions of the Raman spectrum. A contour plot of this spectrally dispersed signal is shown (Fig. 2.2b) as a function of probe delay time, τ_{23}, and anti-Stokes shift relative to the central frequency of the near-Gaussian broadband ω_3 pulse. From this spectrally dispersed signal, for example, it becomes clearer that the 26.9 cm^{-1} oscillation is centered near 1000 cm^{-1} (dashed line denoted *ii*) in Fig. 2.2b) whereas high-frequency oscillations are observable to the blue side (dashed line denoted *i*) and red side (dashed line denoted *iii*) of the central ω_{CARS} frequency. Fourier transforms of the three frequency slices of the dispersed tr-CARS data, following subtraction of the exponentially decaying baseline, are shown in Fig. 2.3. An additional beat frequency, not discernable in the FT of the fully integrated signal, is observed in Fig. 2.3a at 207 cm^{-1}, readily assignable to a coherence between the known vibrational modes at 1003.6 cm^{-1} and 1211.4 cm^{-1}. This highlights the fact that spectral resolution of the ω_{CARS} signal allows better discernment of the beat frequencies contributing to the total ω_{CARS} signal. Thus, by comparison with the known Raman active frequencies of ground state toluene, it is straightforward using this dispersed tr-CARS data to assign all of the observed beat frequencies to pairs of known vibrational modes of toluene.

Numerical simulation of the tr-CARS data provides further insight regarding the nature of this signal obtained using a broadband ω_3 pulse. Fig. 2.4 shows a contour plot of simulated spectrally-resolved tr-CARS signal, calculated assuming the known vibrational

frequencies of toluene and measured decoherence lifetimes, in close agreement with the experimental results (Fig. 2.2b).

These experimental data and simulations, while demonstrating the ability of tr-CARS to allow assignment of Raman active vibrational frequencies, also highlight several difficulties associated with conventional tr-CARS as a Raman probe. For example, the observation of beat frequencies requires deduction of the vibrational frequencies contributing to the quantum beat and makes it difficult to directly assign relative amplitudes of the contributing vibrational modes to the observed CARS spectrum. More importantly, one particular disadvantage of this conventional tr-CARS method, even when spectral dispersion is used, is the assignment of specific coherence frequencies to vibrational modes with spectral resolution comparable to that attainable using other Raman techniques. In fact, the beat frequency between two modes with frequencies ω_a and ω_b reaches its maximum intensity precisely at the mean anti-Stokes frequency, $(\omega_a + \omega_b)/2$, and the range over which this beat frequency is observed has FWHM proportional to the FWHM of the broadband ω_3 pulse spectrum. This contributes to the uncertainty in assigning observed quantum beats to pairs of vibrational modes within a molecule; in typical tr-CARS experiments, this uncertainty is of the order 50 cm^{-1}.[35] Thus, this technique is particularly challenging to use as an excited state probe in cases where the excited state vibrational frequencies are not well characterized.

2.4.1.2 fs/ps CARS

To remove the experimental disadvantages associated with the broadband ω_3 pulse in the tr-CARS setup, the fs/ps CARS technique involves replacement of this broadband pulse

with a narrowband (~15 cm^{-1}) pulse via the adjustable slit in the focal plane of the pulse shaping setup along the ω_3 pulse path. This spectral narrowing also serves to significantly broaden the temporal profile of this pulse to durations longer than a picosecond, as is evident in Fig. 5, where the integrated ω_{CARS} signal (solid curve) from neat toluene is plotted as a function of probe pulse delay, τ_{23}. In the conventional tr-CARS data (Fig. 2.2), there is a significant contribution near $\tau_{23} = 0$ (not shown) of a strong non-resonant signal that typifies tr-CARS and DFWM signals during temporal overlap of the three input pulses. In general, the ratio of this electronic contribution to the desired resonant vibrational signal can be significantly reduced in the detected signal by careful selection of the relative input pulse polarizations and by selective detection of specifically polarized ω_{CARS} signal;[31,36,37] however, such polarization dependence was not exploited here. As a result, this non-resonant contribution plays a significant role in the integrated fs/ps CARS output signal as well, and the integrated ω_{CARS} signal maps the temporal profile of the narrowband ω_3 pulse. Note that the insertion of a slit into the near-Gaussian spectral profile of the ω_3 pulse results in a spectral profile that is the product of a Gaussian and a square-wave; the time domain pulse therefore exhibits the structure of a Gaussian convoluted with a sinc pulse, as confirmed by the numerically simulated temporal profile of a 16 cm^{-1} square-wave filtered ω_3 pulse (Fig. 2.5, dashed curve). Thus, a small intensity "recurrence" is present in the ω_3 pulse after an initial minimum.

Spectral dispersion of the ω_{CARS} signal resulting from the fs/ps CARS probe setup provides further insight into the relative contributions of resonant and non-resonant signal to the integrated ω_{CARS} signal. It is precisely at the minimum of the integrated ω_{CARS} signal that

the non-resonant contribution is minimized. The time delay of this minimum is 1.93 ps for the slit width used here, and dictates the optimal time delay of this ω_3 pulse relative to the initial ω_1 and ω_2 pulses for fs/ps CARS detection. This optimal delay corresponds to the delay at which the entire ps-duration ω_3 beam (aside from the small post-pulse recurrence) immediately follows the ω_1 and ω_2 pulses in time. At this specific time delay, the non-resonant signal resulting from temporal overlap of the three input beams is minimized, and the ω_3 pulse is optimally overlapped in time with the decaying molecular response function, which contains the vibrational coherences induced by interaction with pulses 1 and 2.

The fs/ps CARS signal for neat toluene is displayed in Fig. 2.6, where the spectrally resolved ω_{CARS} output observed at this fixed optimal delay, τ_{23} = 1.93 ps, is shown in Fig. 6a. The four Raman active modes of toluene present in this spectral range are clearly resolved. Despite the use of a spectrometer that is not optimized for sensitive detection, this fs/ps CARS spectrum was acquired in roughly 20 seconds and requires no background subtraction. This acquisition time is equivalent to that associated with a single time-step of the conventional tr-CARS data acquisition. Thus, a major advantage of the fs/ps CARS technique relative to conventional tr-CARS is its multiplexed nature, associated with simultaneous probing of a significant portion of the full molecular response decay using the narrowband, ps-duration ω_3 pulse at a fixed delay dictated by the duration of the pulse. The accessible range of vibrational frequencies observed using this method depends on the range of frequencies accessible in the (ω_1 - ω_2) bandwidth, and is typically of the order 800 cm^{-1} with the current experimental setup.

The additional advantages of fs/ps CARS relative to conventional tr-CARS are immediately obvious in the observed signal. Whereas quantum beat intensities detected using conventional tr-CARS depend on a product of the amplitudes of each eigenstate in the coherence prepared by the ω_1 and ω_2 pulses, the fs/ps CARS output signal allows direct measurement of the individual mode intensities. Additionally, the mode frequencies can be directly determined by the anti-Stokes shift relative to the narrowband ω_3 pulse and, when fit to Lorentzian peak profiles, are in agreement with known toluene Raman frequencies[34] to within 1 cm^{-1}.

Shown in Fig. 2.6b are simulations of the fs/ps CARS signal using these known vibrational frequencies and vibrational decoherence lifetimes consistent with the observed decay constants from the conventional tr-CARS data. An assumed 16 cm^{-1} slit function was applied to the broadband ω_3 pulse, resulting in the temporal profile shown as a dashed curve in Fig. 2.5, plotted at the optimal fs/ps CARS delay relative to the ω_1 and ω_2 pulses. The dashed curve in Fig. 2.6b is the simulated ω_{CARS} anti-Stokes shift spectrum calculated at the optimal time delay (1.93 ps) dictated by the ω_3 bandwidth; the linewidths associated with this simulation depend on a convolution of the ω_3 bandwidth and the natural linewidths associated with vibrational decoherences, which, based on the tr-CARS data above, are ~2.5 cm^{-1} for toluene. The solid curve in Fig. 2.6b includes an additional convolution of the simulated fs/ps CARS signal with the 14 cm^{-1} Gaussian spectral response function of the spectrometer used in these experiments. This simulation, which compares well with the experimental results, demonstrates that the measured linewidths in this fs/ps CARS scheme depend both on the molecular dephasing timescales as well as on the overall instrument

spectral response function, which in turn depends both on the spectrometer resolution and the bandwidth of the ω_3 probe pulse. In the current experimental configuration, this overall spectral resolution is roughly 15 – 20 cm^{-1}. Note, however, that the ω_3 bandwidth can be reduced experimentally if necessary to provide better spectral resolution.

Additionally, as borne out in simulations, which do not explicitly include the electronic contributions present near $\tau_{23} = 0$, the optimal time delay also provides the optimal spectral resolution of the detected fs/ps CARS signal for a given ω_3 pulse bandwidth. This is the case since the output polarization, $P^{(3)}$, is only nonzero subsequent to interaction of the sample with each of the three input pulses, and the temporal delay (τ_{34}) of the ω_{CARS} output signal relative to the final interaction ω_3 is comparable in duration to $\tau_{12} \approx 0$ due to the fast electronic dephasing time associated with the final non-resonant interaction. Thus, the output polarization timescale roughly correlates to the duration of the ω_3 pulse that is present *subsequent* to the time-overlapped ω_1 and ω_2 pulses. The time-energy uncertainty principle therefore dictates that this optimal time delay, in which the entirety of the ω_3 pulse directly follows the ω_1 and ω_2 pulses in time, also results in the narrowest linewidths associated with the output fs/ps CARS peaks.

2.4.2 Resonant CARS: rhodamine 6G

To demonstrate the application of this probe technique toward a more complex system, we have also carried out both conventional tr-CARS and fs/ps CARS studies on R6G. In this case, the ω_1 pulse, centered at 509 nm (FWHM ~500 cm^{-1}), was chosen to be on electronic resonance with the $S_1 \leftarrow S_0$ electronic transition,[38] whereas pulse 2 was

centered at 556 nm (FWHM ~275 cm^{-1}). The results for both tr-CARS (FWHM of ω_3 pulse ~350 cm^{-1}) and fs/ps CARS (FWHM of ω_3 pulse ~15 cm^{-1}) are shown in Fig. 2.7.

A typical plot of spectrally dispersed tr-CARS signal for R6G is depicted in Fig. 2.7a, revealing a more complicated set of oscillations associated with the vibrational coherences prepared by pulses 1 and 2. Following removal of exponentially decaying baseline signal, Fourier transforms were performed on the time-resolved ω_{CARS} signal for each anti-Stokes shift, and the results are shown in Fig. 2.7b. This contour plot reveals the complexities associated with numerous beat frequencies spaced throughout the spectrally observed range. Given that there are 6 Raman-active modes in this spectral range, there is the possibility to observe 15 beats, although some beat frequencies are expected to exceed the bandwidth of the broadband ω_3 pulse. In fact, we are able to observe 11 separate beat frequencies resulting from the coherences between pairs of these 6 vibrational modes. Still, these results reinforce the fact that it is difficult to assign vibrational frequencies using the conventional tr-CARS method in molecules with several Raman active modes. In contrast, when we convert to a spectrally narrow probe pulse (~15 cm^{-1}) for fs/ps CARS detection (Fig. 2.7c), the Raman-active modes are readily observed with comparable resolution, as the complexities associated with detection of beat frequencies are removed. As above, this spectrum has been generated in just seconds compared to the minutes to hours required to acquire and analyze the tr-CARS data shown in Fig. 2.7a. The detected frequencies are in good agreement with previous studies.[11,38]

An additional benefit associated with the CARS technique is the discrimination against background fluorescence due to the directed nature of the ω_{CARS} output beam;[28] these benefits are also realized in the fs/ps CARS technique, and the data displayed in Fig. 2.7c are

shown without background correction associated with the removal of fluorescence. Additionally, excellent signal-to-noise ratio can be acquired in a fraction of the time that would be required for a full tr-CARS spectrum of R6G.

These R6G data represent a case in which the Raman free induction decay induced by interaction with pulses 1 and 2 has a lifetime (measured to be ~500 fs and homogeneously broadened from the exponentially-decaying integrated tr-CARS signal depicted in Fig. 7a) that is shorter than the ps-duration ω_3 pulse used in the fs/ps CARS scheme. Although the current instrument spectral response limits the resolution to ~15 cm^{-1}, it is clear that the measured linewidths of the fs/ps CARS data (20 – 24 cm^{-1} FWHM assuming Lorentzian lineshapes) are broader than this instrument response and consistent with the vibrational lifetimes measured with the tr-CARS scheme.

2.4.3 Low-frequency modes: chloroform

To highlight a particular advantage of this fs/ps CARS technique relative to other ultrafast time-resolved Raman spectroscopies, we have applied this detection scheme to the low frequency regime of neat chloroform. The application of this technique is not limited to non-degenerate versions of the CARS setup; in cases where ω_1 and ω_2 are nearly or exactly degenerate (*i.e.*, transient grating), the ω_{CARS} output contains Raman active modes in the low-frequency regime (0 - 700 cm^{-1}). In this case, the ω_1 and ω_2 pulses are tuned near their degeneracy point at 532 nm.

The results of these low-frequency fs/ps CARS experiments are shown in Fig. 2.8. Readily observable are the three Raman active modes at 262 cm^{-1}, 368 cm^{-1} and 667 cm^{-1}.[39] More importantly, the scattering from the narrowband ω_3 probe, observed at an anti-Stokes

shift of 0 cm^{-1}, is nearly completely suppressed via spatial filtering of the ω_{CARS} output signal resulting from phase matching.[27,28] Thus, this fs/ps CARS technique shows particular promise for multiplexed detection in pump-CARS experiments probing the short-time evolution of low-frequency Raman active vibrational modes; it is these low-frequency acceptor modes that play a particularly important role in intramolecular vibrational energy redistribution following electronic excitation.

2.4.4 fs/ps CARS as a time-resolved Raman probe

While the focus of this work is on the multiplexed nature of the fs/ps CARS probe and the associated advantages of this method relative to conventional tr-CARS, it is important to note the temporal resolution of this fs/ps CARS probe technique is the same as that used in conventional tr-CARS experiments; pulses 1 and 2 are both broadband ultrafast pulses and contain sufficient bandwidth to support sub-50 fs pulses. As is the case in experiments in which conventional CARS or DFWM are used as time-resolved probes of Raman active modes, the durations of these pulses dictate the temporal resolution of this probe technique when used in a pump-CARS scheme; these initial pulses prepare the vibrational coherences to be probed by the ω_3 pulse. In conventional tr-CARS experiments, this final pulse timing is scanned to probe the response function of the molecular system, whereas the narrowband (and therefore ps-duration) ω_3 pulse used in the fs/ps CARS scheme provides an integrated detection of this molecular response function that does not require scanning of this final pulse and provides direct measurement of the vibrational frequencies and relative intensities. Note that we have not addressed an example here in which the vibrational lifetimes are significantly shorter than the ω_3 pulse duration. While the numerical

simulations suggest that dynamics shorter than the ω_3 pulse will be borne out in the lineshapes measured using the fs/ps CARS probe technique, we will address this issue specifically in future work using an optical setup with improved spectral resolution.

The multiplex nature of this fs/ps CARS technique shows tremendous promise in expanding upon the capabilities of current pump-CARS schemes, and this technique has already been used in our laboratory as an ultrafast probe of excited state dynamical processes, including coumarin dye evolution during solvation[40] and the isomerization of a charge-transfer stilbene.[41] Analogous to the temporal resolution attainable in the FSRS technique in which one probe pulse of sub-100 fs duration dictates the temporal resolution while a narrowband probe defines the spectral resolution,[9-12] this fs/ps CARS technique provides both optimal spectral resolution while maintaining a temporal resolution sufficient to probe subpicosecond dynamics following excitation with an initial pulse, ω_{ex}. As discussed above, an additional advantage associated with this technique results from the spatial separation of signal beam from the three input pulses, which allows detection of background-free signal, making this technique particularly amenable to probing temporal evolution of low-frequency modes.

2.5 Conclusions

The fs/ps CARS technique has been developed to be used as a time-resolved probe of the evolution of Raman active vibrational modes following electronic excitation with an ultrafast excitation pulse. Here, we have described the application of this technique to probe Raman active modes in ground state systems for comparison with the conventional tr-CARS method. While maintaining all of the advantages associated with time-resolved CARS

methods,[28] fs/ps CARS utilizes a narrowband ω_3 pulse to provide a multiplexed detection of the output ω_{CARS} signal. This method has been applied to toluene, in which ω_1 is not resonant with an electronic transition and to R6G, where the initial pulse frequency coincides with an electronic resonance. The fs/ps CARS scheme has also been successfully applied to observe low-frequency modes in chloroform. In all cases, this technique provides sufficient spectral resolution to assign all expected Raman active peaks over a wide spectral range (~800 cm^{-1}) without prior knowledge of the vibrational frequencies.

The spatial separation of the outgoing ω_{CARS} signal from the incoming beams allows essentially background-free detection of the frequency-resolved CARS signal; neither fluorescence nor any of the input beams are observed in this output pulse direction dictated by phase-matching conditions. As a result, this multiplexed CARS detection scheme is particularly unique in its ability to probe the short-time evolution of low-frequency modes.

2.6 Acknowledgments

We are grateful for the experimental contributions of Tse-Ming Hsin to this work. We thank Jacob Petrich, Mintu Halder, and Vasilios Stavros for insightful discussions. Financial support from Iowa State University and Ames Laboratory is gratefully acknowledged.

2.7 References

1. M. C. Beard, G. M. Turner, and C. A. Schmuttenmaer, J. Phys. Chem. B **106**, 7146 (2002).

2. G. Haran, W. Sun, K. Wynn, and R. M. Hochstrasser, Chem. Phys. Lett. **274**, 365 (1997).

3. E. T. Nibbering, F. Tschirschwitz, C. Chudoba, and T. Elsaesser, J. Phys. Chem. A **104**, 4236 (2000).

4. R. McElroy and K. Wynn, Phys. Rev. Lett. **79**, 3078 (1997).

5. E. T. J. Nibbering, H. Fidder, and E. Pines, Annu. Rev. Phys. Chem. **56**, 337 (2005).

6. J. C. Deàk, L. K. Iwaki, and D. D. Dlott, J. Phys. Chem. A **102**, 8193 (1998).

7. H. Chosrowjan, S. Taniguchi, N. Mataga, M. Unno, S. Yamauchi, N. Hamada, M. Kumauchi, and F. Tokunaga, J. Phys. Chem. B **108**, 2686 (2004).

8. Z. Wang, A. Pakoulev, and D. D. Dlott, Science **296**, 2201 (2002).

9. D. W. McCamant, P. Kukura, and R. A. Mathies, J. Phys. Chem. A **107**, 8208 (2003).

10. P. Kukura, D. W. McCamant, P. H. Davis, and R. A. Mathies, Chem. Phys. Lett. **382**, 81 (2003).

11. D. W. McCamant, P. Kukura, S. Yoon, and R. A. Mathies, Rev. Sci. Instrum. **75**, 4971 (2004).

12. S. Lee, D. Zhang, D. W. McCamant, P. Kukura, and R. A. Mathies, J. Chem. Phys. **121**, 3632 (2004).

13. P. Kukura, D. W. McCamant, S. Yoon, D. B. Wandschneider, and R. A. Mathies, Science **310**, 1006 (2005).

14. M. Yoshizawa, M. Kubo, and M. Kurosawa, J. Lumin. **87-89**, 739 (2000).

15. F. S. Rondonuwu, Y. Watanabe, J. Zhang, F. Kentaro, and Y. Koyama, Chem. Phys. Lett. **357**, 376 (2002).

16. M. Yoshizawa and M. Kurosawa, Phys. Rev. A **61**, 013808 (2000).

17. S. Takeuchi and T. Tahara, Chem. Phys. Lett. **326**, 430 (2000).
18. T. Siebert, V. Engel, A. Materny, W. Kiefer, and M. Schmitt, J. Phys. Chem. A **107**, 8355 (2003).

19. T. Siebert, M. Schmitt, V. Engel, A. Materny, and W. Kiefer, J. Am. Chem. Soc. **124**, 6242 (2002).

20. T. Siebert, R. Maksimenka, A. Materny, V. Engel, W. Kiefer, and M. Schmitt, J. Raman Spectrosc. **33**, 844 (2002).

21. R. Maksimenka, B. Dietzek, A. Szeghalmi, T. Siebert, W. Kiefer, and M. Schmitt, Chem. Phys. Lett. **408**, 37 (2005).

22. T. Hornung, H. Skenderovic, and M. Motzkus, Chem. Phys. Lett. **402**, 283 (2005).

23. S. Fujiyoshi, T. Ishibashi, and H. Onishi, J. Phys. Chem. A **108**, 11165 (2004).

24. S. Fujiyoshi, S. Takeuchi, and T. Tahara, J. Phys. Chem. A **108**, 5938 (2004).

25. S. Fujiyoshi, S. Takeuchi, and T. Tahara, J. Phys. Chem. A **107**, 494 (2003).

26. D. F. Underwood and D. A. Blank, J. Phys. Chem. A **107**, 956 (2003).

27. S. Mukamel, *Principles of Nonlinear Optical Spectroscopy*. (Oxford University Press, New York, 1995).

28. J. A. Shirley, R. J. Hall, and A. C. Eckbreth, Opt. Lett. **5**, 380 (1980).

29. A. M. Weiner, Rev. Sci. Instrum. **71**, 1929 (2000).

30. M. Motzkus, S. Pedersen, and A. H. Zewail, J. Phys. Chem. **100**, 5620 (1996).

31. J. Etchepare, G. Grillon, J. P. Chambaret, G. Hamoniaux, and A. Orszag, Opt. Commun. **63**, 329 (1987).

32. A. Y. Chikishev, G. W. Lucassen, N. I. Koroteev, C. Otto, and J. Greve, Biophys. J. **63**, 976 (1992).

33. D. D. Dlott, in *Laser Spectroscopy of Solids II*, edited by W. M. Yen (Springer-Verlag, Berlin, 1988), pp. 167.

34. R. L. McCreery, Raman Shift Frequency Standards; URL: http://www.chemistry.ohio-state.edu/~rmccreer/freqcorr/shift.html#shiftdir (2005).

35. M. Heid, S. Schlücker, U. Schmitt, T. Chen, R. Schweitzer-Stenner, V. Engel, and W. Kiefer, J. Raman Spectrosc. **32**, 771 (2001).
36. J.-L. Oudar, R. W. Smith, and Y. R. Shen, Appl. Phys. Lett. **34**, 758 (1979).

37. J. Cheng, A. Volkmer, L. D. Book, and X. S. Xie, J. Phys. Chem. B **106**, 8493 (2002).

38. S. Matsubara and H. Takahashi, Chem. Phys. Lett. **108**, 475 (1984).

39. B. Schrader, *Raman/infrared atlas of organic compounds*, 2nd ed. (VCH, New York, NY, 1989).

40. B. D. Prince, A. Chakraborty, B. M. Prince, T.-M. Hsin, and H. U. Stauffer, in *Femtochemistry VII: Fundamental Ultrafast Processes in Chemistry, Physics, and Biology*, edited by A. W. Castleman, Jr. and M. L. Kimble (Elsevier, Amsterdam, 2006), pp. 66.

41. B. D. Prince, A. Chakraborty, B. M. Prince, and H. U. Stauffer, in *Femtochemistry VII: Fundamental Ultrafast Processes in Chemistry, Physics, and Biology*, edited by A. W. Castleman, Jr. and M. L. Kimble (Elsevier, Amsterdam, 2006), pp. 70.

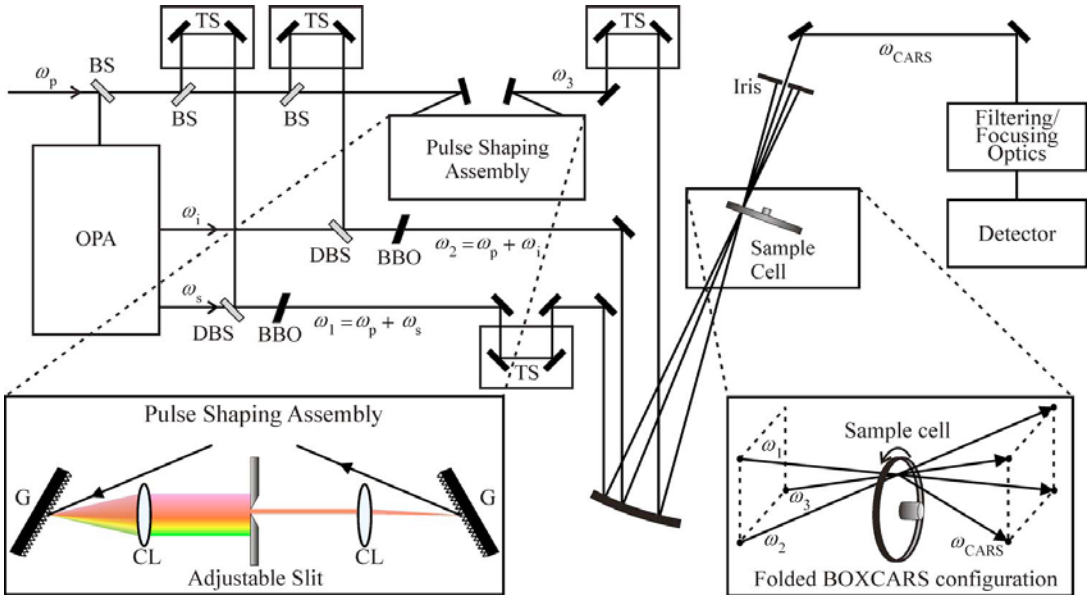

Figure 2.1: Schematic optical layout, as described in text. BBO: Nonlinear optic (β-BBO, for sum-frequency generation); BS: Beam splitter; CL: Cylindrical lens; DBS: Dichroic beam splitter; G: Grating; OPA: Optical Parametric Amplifier; TS: Translation stage

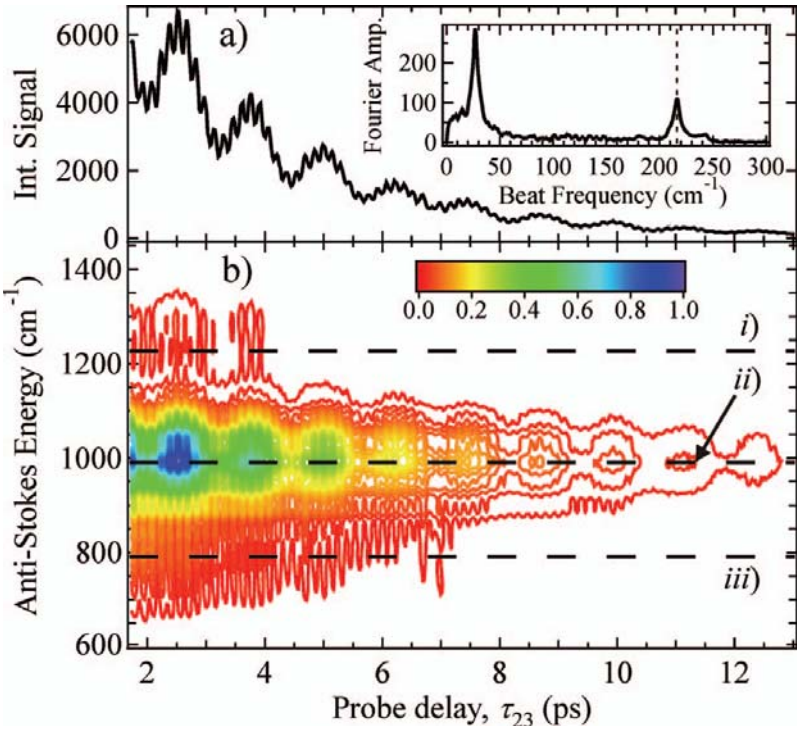

Figure 2.2: (a) Spectrally integrated time-resolved ω_{CARS} signal from neat toluene as a function of probe delay, τ_{23}, with Fourier transform (FT, inset). Dashed line in FT denotes beat frequency that is poorly resolved in integrated signal FT. (b) Spectrally dispersed time-resolved ω_{CARS} signal from neat toluene (contour plot of spectral intensity, normalized to peak near 2.5 ps); anti-Stokes energies measured relative to ω_3 centered at 12610 cm^{-1}. FTs of frequency slices denoted by *(i)-(iii)* are shown in Figs. 3(a)-3(c), respectively, following removal of exponentially decaying baseline.

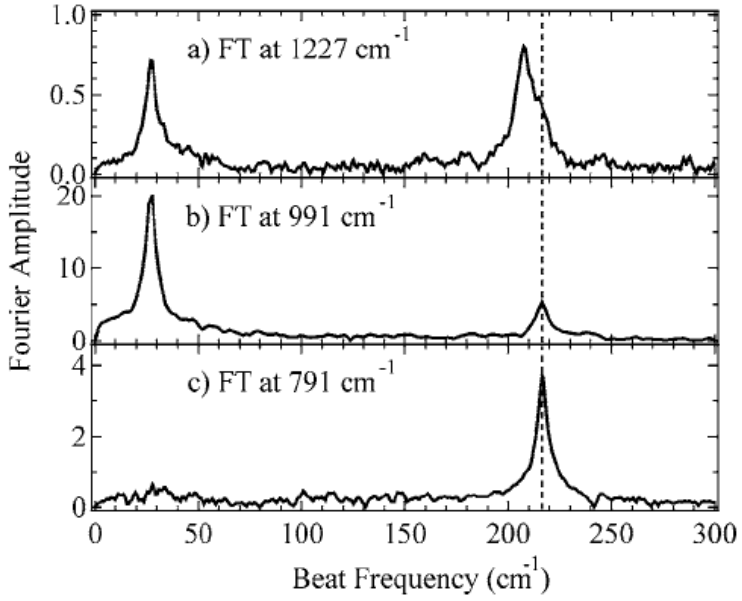

Figure 2.3: Fourier transforms (FTs) of frequency slices shown in Fig. 2(b). Dashed line represents beat frequency poorly resolved in Fig. 2(a), demonstrating a benefit of spectral resolution of tr-CARS signal.

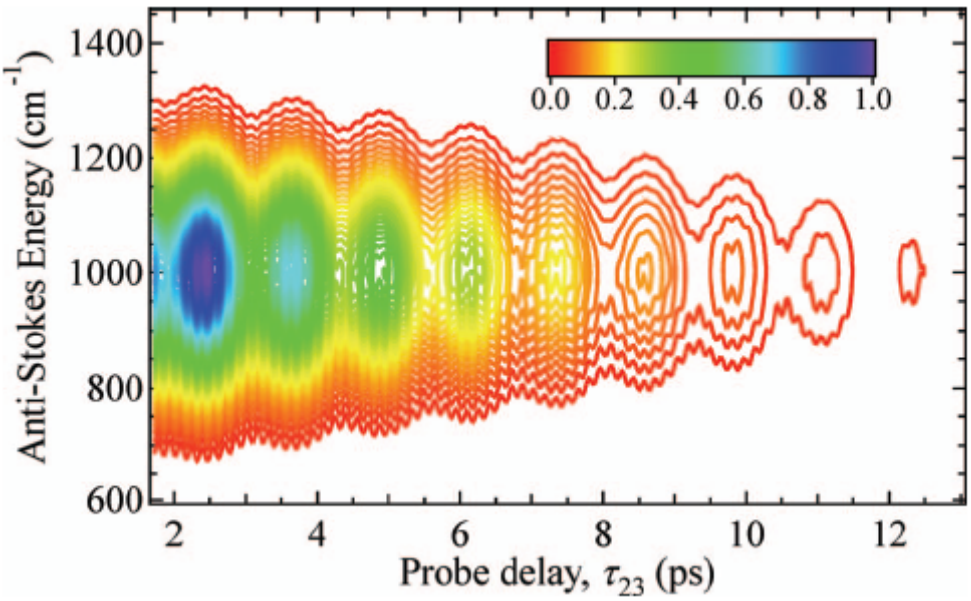

Figure 2.4: Numerical simulation of spectrally resolved tr-CARS data from toluene, shown as contour plot of spectral intensity, normalized to peak near 2.5 ps.

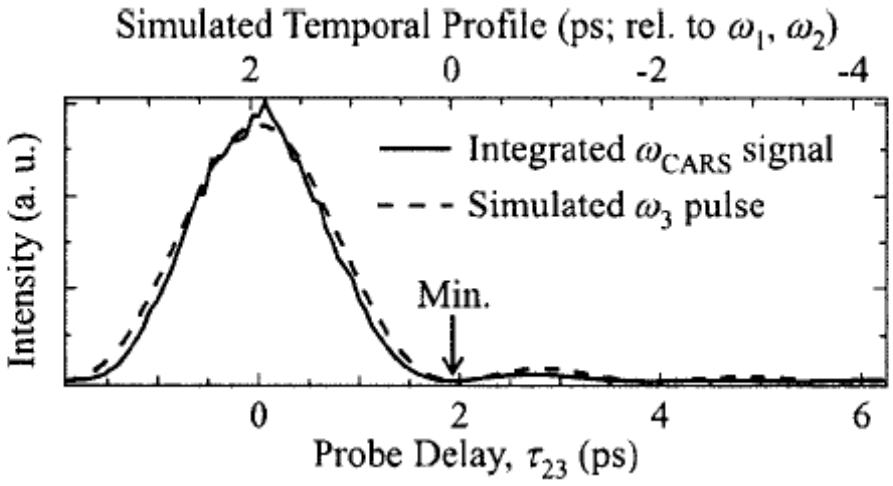

Figure 2.5: Experimental integrated ω_{CARS} signal (solid curve) in fs/ps CARS studies of neat toluene, shown as a function of probe delay, τ_{23} (bottom axis). Arrow denotes optimal timing for spectrally resolved fs/ps CARS data shown in Fig. 6. Pulse duration and profile compare well with numerical simulation (dashed curve) of optimal ω_3 pulse temporal profile, assuming a 16 cm^{-1} square wave slit, plotted at its optimal delay relative to ω_1 and ω_2 pulses (top axis).

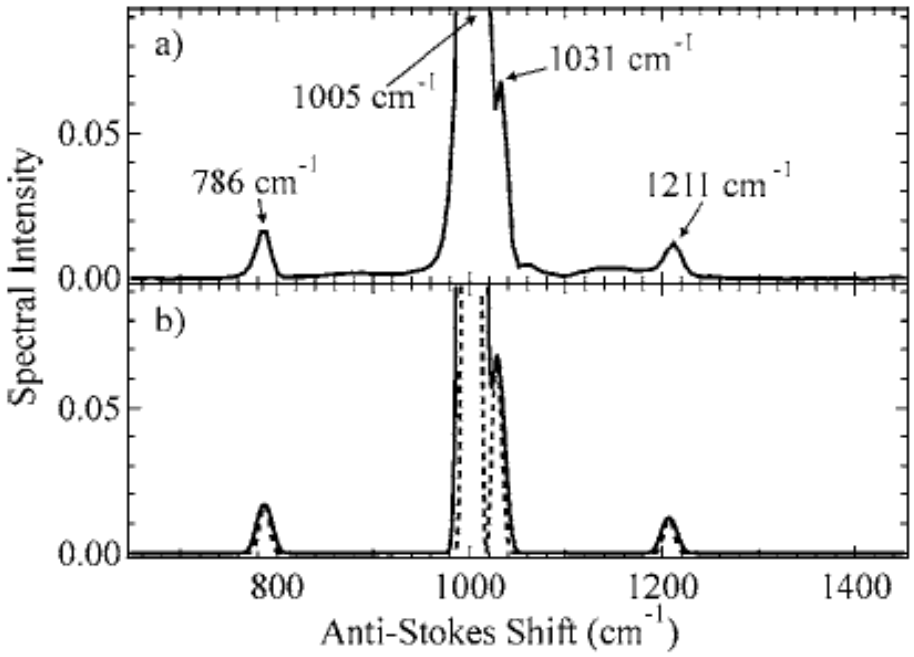

Figure 2.6: (a) Experimental fs/ps CARS signal from neat toluene, normalized to the 1005 cm^{-1} peak intensity (details in text); (b) Simulation of toluene CARS signal using narrowband (16 cm^{-1}) pulse for ω_3. Dashed curve represents simulated spectrum independent of instrument response; solid curve includes convolution with 14 cm^{-1} (FWHM) Gaussian spectrometer response.

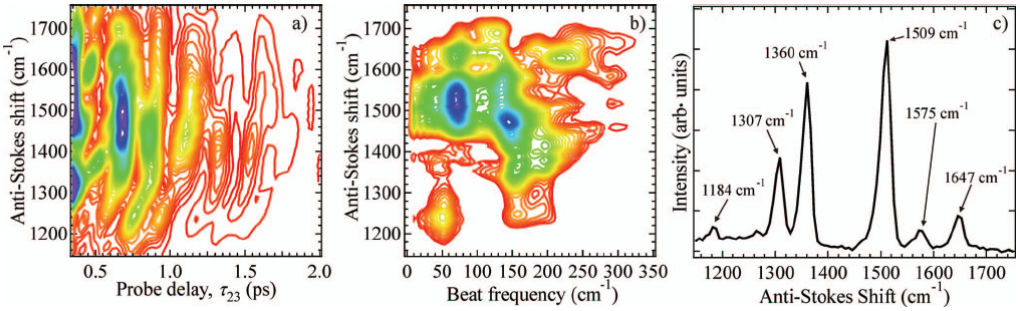

Figure 2.7: (a) Spectrally dispersed time-resolved CARS signal from R6G in methanol, shown as contour plot of spectral intensity (contour color scheme analogous to that of Fig. 4); frequencies measured relative to ω_3 centered at 12 538 cm^{-1}; (b) FT of this spectrally dispersed CARS signal, shown as contour plot; (c) Spectrum of R6G in methanol obtained using fs/ps CARS method.

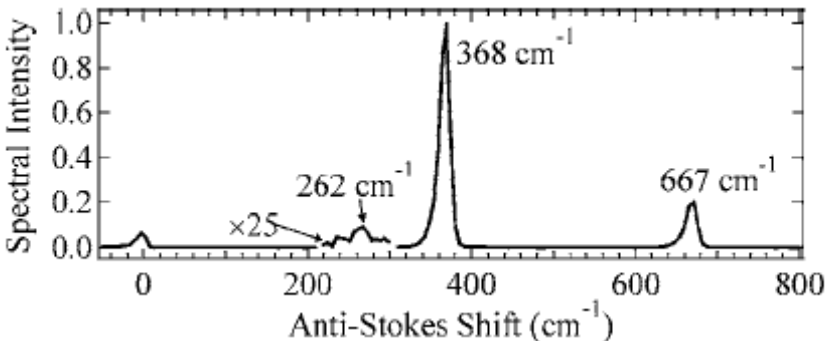

Figure 2.8: fs/ps CARS signal from neat chloroform, normalized to the 368 cm^{-1} peak intensity.

CHAPTER 3: DISCUSSION OF TIME-RESOLUTION, FREQUENCY RESOLUTION AND EXPERIMENTAL FINDINGS USING FS/PS CARS ON EXCITED STATE SYSTEMS

Benjamin D. Prince, Mikhail Slipchenko, Beth M. Prince and Hans U. Stauffer

Department of Chemistry, Iowa State University, Ames, Iowa 50011-3111

3.1 Overview

The development of the fs/ps CARS probe and its dual use of picosecond and femtosecond laser beams to generate a coherent Raman signal have opened interesting and relevant questions about time resolution and frequency resolution when it is applied to a time dependent system (i.e. excited states, particularly those with shorter lifetimes than picoseconds). The advantages and disadvantages of purely femtosecond CARS were discussed in chapter 2 and will not be discussed in great detail in this section.

It should be noted that purely picosecond CARS has seen a great deal of experimental work as well, both in the ground and excited states of chemical systems[1-7]. Techniques were developed utilizing polarization to help separate the fixed contribution of non-resonant signal from that of chemically relevant resonant signal. Typically picosecond CARS used identical beams for ω_1 and ω_3 which required the two field interactions to be overlapped in time. Due to the fact that for CARS beams that are non-resonant (and many resonant cases) the signal is greatest when ω_1 and ω_2 are time overlapped, a large background signal was generated solely from the requirement of three temporally and spatially overlapped beams generating a fourth wave. This background signal competes (and can often be larger) with the molecular specific vibrationally resonant signal. The interactions generated from the competition of the resonant

and non-resonant components of the outputted light lead to interference patterns that are not necessarily straightforward to deconvolute. By controlling the polarizations of each electric field interaction, experiments could utilize the different polarizations of non-resonant and vibrationally resonant signal to allow some suppression of this interference at the cost of some signal strength. The result of these types of experiments allowed for increased frequency resolution (typically 15-30 cm^{-1}) with time resolution on the order of picoseconds.

Because the CARS process requires only two field interactions to actually populate a vibrational mode ($\omega_{hv} = \omega_1 - \omega_2$), utilizing these two fields as femtosecond in duration allows these vibrations to be initially populated only during the very short duration of the pulse. The molecules will then dephase with their respective decay times which is dependent on the molecule under study. These dephasing times are probed by the third field required for generating CARS signal. If this third field is shorter in duration than the dephasing time only a portion of the decay is integrated and the linewidth detected will be broader than the natural linewidth. Conversely, if the field is longer in duration than the dephasing time, for example a continuous wave (CW) laser, then the entire dephasing time is integrated and the outputted signal will have linewidth = 2Γ (assuming CW beam). It will be shown in the following sections that by using a combination of two femtosecond duration pulses followed by a third picosecond duration pulse sequence, with each pulses respective timings controlled, the outputted signal maintains both femtosecond time resolution and has improved frequency resolution over femtosecond CARS.

In addition to improved frequency resolution versus femtosecond CARS, the ability exists to more closely measure the true natural linewidth Γ instead of 2Γ by controlling the time position of the third electric field relative to the first and second. The narrowing of the

linewidth versus, for example ps CARS or spontaneous Raman, allows separation of close lying vibrational modes as well as the possibility of manipulating faster dephasing vibrational modes from the slower dephasing vibrational modes.

3.2 Time resolution

To address the role of the picosecond ω_3 on the time resolution of excited state systems experiments were undertaken to ascertain how the length of this third field interaction actually affects the intensity dynamics of the detected CARS signal. Two model systems that we have chosen are 4-dimethylamino-4'-nitrostilbene (DANS) and N,N-dimethyl-*p*-nitroaniline (DMPNA). Both systems provide relatively short excited state lifetimes with DANS having a solvent dependent lifetime typically on the order of 10-30 picoseconds and DMPNA decaying on an ~600 fs timescale.

Figure 3.1 gives an example of a simple pump-probe transient gain experiment using a 100 fs 400 nm pump and 2 ps 800 nm probe and 100 fs 400 nm pump and 80 fs 800 nm probe for DANS in acetonitrile. The effect of lengthening the pulse (left side panels) on the simple pump-probe experiment is clear as the decay dynamics are quite smoothed out compared to the use of the femtosecond laser pulse. These results are certainly not unpredicted; the use of either a long pump or a long probe pulse will result in faster processes being observed in a smoothed way which muddles the interpretation of the process.

It remains to be seen if lengthening of the ω_3 pulse (sometimes called the "probe" pulse) in CARS will generate much the same effect. To ascertain this, the same system is studied though using pump-fs/ps CARS with all parameters being held identical except the electric field of the ω_3 and the position of the same field to minimize the non-resonant contribution.

The relevant experimental parameters are shown in fig. 3.2 along with the pulse sequence used in these CARS experiments. In the case of DANS, excitation with 400 nm excites the molecule into the first singlet excited state. The first CARS field interaction (ω_1 = 510 nm, $\Delta\omega$ = 300 cm^{-1}) is resonant with a higher lying excited state, the second field (ω_2 = 555 nm, $\Delta\omega$ = 300 cm^{-1}) acts in downward ket fashion to populate vibrational modes in the S_1 potential. The third CARS field (ω_3 = 794 nm, $\Delta\omega$ = 6 and 14 cm^{-1} respectively) is resonant as stimulated emission to a lower lying electronic state and acts in a downward bra transition (+**k** vector).

Scanning the 400 nm excitation beam with the different bandwidth ω_3 beams allows the comparison of the population dynamics of the excited state DANS. The contour maps for the two experiments are shown in fig. 3.3 with the different ω_3 fields. Despite the considerably large difference in time duration of the ω_3 fields, very similar results are seen across the entire experimentally accessible region. As will be shown in later sections, the signal level is a function of both ω_3 duration and the real linewidth of the mode being populated. This is the reason for the apparent increase in signal to noise in A) which is a result of using the 14 cm^{-1} bandwidth ω_3.

Figure 3.4 displays the intensity dynamics of the mode near 1480 cm^{-1} in figure 3.3. The normalized intensity using the two different ω_3 bandwidths is quite similar on the rise time despite the duration of the pulses being considerably different. The decay dynamics of the same peak appear to be slightly different but both fall generally within the typical uncertainty range for other experiments performed on this system in our laboratory (not shown). With particular emphasis on the rise time, it would appear that despite the different time durations, the CARS intensity dynamics appear independent of the duration of the ω_3 pulse.

From these experiments on DANS, a few new questions were formulated. One major concern was that DANS undergoes relaxation in polar solvents through a complicated stepwise scheme that is not yet fully understood which might bias the growth results somehow. Additionally, the non-radiative decay probed for DANS in acetonitrile has a lifetime on the order of 10 picoseconds which is far longer than the duration of the third electric field. We set out a goal of finding a system with a short lived excited state that is amenable to the experimental setup employed in our laboratory. It became clear that a smaller version of DANS was well studied in literature with regards to its vibrationally hot ground state and work had been previously done on the electronic transient gain spectra of the excited state and hypotheses formulated about the structure of the excited state. We settled on N,N-dimethyl-*p*-nitroaniline (DMPNA) as an interesting system to study because it has an unusually fast internal conversion of ~600 fs in nearly all solvents probed by the electronic transient gain experiments as well as having many open questions about the structure of the excited state. For the interested reader, additional information can be found in chapter 6 about DMPNA and its structure in the electronically excited state and internally converted vibrationally hot ground state.

The experimental scheme is very similar for DMPNA as it was for DANS and is shown in figure 3.5. An initial 400 nm pulse excites molecules into the excited state where the ω_2 has a resonance connecting the excited state and ground state. Reabsorption from the ground electronic state populates excited state vibrational modes and the non-resonant ω_3 pulse completes the four wave mixing process. In the case of DMPNA, three unique ω_3 electric fields are used with bandwidths of 7.5 cm^{-1} (red trace), 14 cm^{-1} (orange) and 22.5 cm^{-1} (pink) respectively. A sample ground and excited state spectra are shown for DMPNA

in acetonitrile using the 7.5 cm^{-1} ω_3 electric field in figure 6. The strongest Raman active mode is the symmetric NO_2 stretch and, in the ground state, two lesser modes are observed in the CARS probed region at ~1200 cm^{-1} and 1117 cm^{-1}. When the 400 nm beam is applied at ~100 fs delay before the ω_1 and ω_2 pulses, an excited state spectrum is obtained. A slightly downshifted NO_2 symmetric stretch is clearly observed as well as more intense 1110 cm^{-1} mode. New features appear to manifest themselves at ~1450, 1510, and 1590 cm^{-1}. The frequencies of all of these modes are very similar to those obtained in the ground state (at higher concentrations) and will not be discussed in this chapter but will be further elaborated on in chapter 6.

To probe the effect of the different bandwidths on the intensity dynamics, gaussian lineshapes were applied to the obtained excited state spectra. Because of the large ratio of signal in the excited state to the ground state of the 1510 cm^{-1} mode, it was selected as the best representative mode for displaying the dynamics of this molecule. As will be seen in the next chapter, close lying modes of CARS signal can create very complex intensity dynamics.

Figure 3.7 contains the results of the fitting of this peak for the three separate ω_3 bandwidths as well as the instrument response time (IRF) for the pump-fs/ps CARS setup employed in these experiments (~125 fs IRF). The results are extremely similar in both rise and decay times and fit well to a convolution of the IRF with a simple 250 fs exponential decay. Removing the concentration squared dependence of CARS signal returns a decay time of 540 fs ± 70 fs which is in close agreement with the electronic pump-probe experiments. The linewidth of the narrowest excited vibrational mode (determined in next section) is approximately $1.287*\Gamma = 5.64$ cm^{-1} which puts its 2Γ value at 8.76 cm^{-1}

suggesting a lifetime of the excited state at greater or equal to approximately 600 fs if the vibrational dephasing time is dictated by the electronic dephasing time.

Both of these experiments lend themselves to suggesting the slow rise of the time-shifted ω_3 has no effect on the observed intensity dynamics in the electronic excited state. Two differing experiments were designed with an emphasis on short excited state lifetimes (~10 ps for DANS, and ~500-600 fs for DMPNA) in order to probe the effect of changing the time durations on the observed signal.

3.3 Frequency Resolution

As was developed in the last chapter, the effect of time-shifting the ω_3 electric field to minimize the molecularly non-resonant CARS signal can be well exploited in the fs/ps CARS technique. This time shifting serves two purposes, the first is to minimize the interfering non-resonant component from the resonant vibrational components and secondly to improve upon the 2Γ frequency resolution observed in both spontaneous Raman and conventional ps-CARS.

The purely non-resonant CARS signal obtained using fs/ps CARS on a 150 μm thick microscope cover slip is shown in figure 8. The delay axis is the scanning of the ω_3 pulse by means of a computer controlled delay stage over the initiating CARS pulses, ω_1 and ω_2. This signal was obtained using $\omega_1 - \omega_2$ centered at ~1400 cm^{-1} and ω_3 bandwidth = ~15 cm^{-1}. Purely non-resonant signal is symmetric about the time-overlapped 100 fs ω_1 and ω_2 pulses which are centered at delay = 0 ps. The bandwidth of the non-resonant signal is a function of the bandwidth of the first two CARS pulses and is often shaped much like the top graph of

figure 3.8 except when interference with other signals (i.e. those from vibrationally resonant CARS signal) occurs.

To illustrate the effect of this non-resonant signal on vibrationally resonant signal, DMPNA of 220 μm thickness and 50 mM concentration was placed in a rotating cell with 2 mm thick fused silica windows. The ω_3 pulse was again scanned in the exact same fashion of figure 3.8 and the results are shown in figure 3.9. The result is quite different than the purely non-resonant signal obtained from glass particularly with respect to the very significant NO_2 symmetric stretch intensity in the ground state. For strong Raman active bands (those with very large Raman cross sections), the interfering effect of non-resonant signal is very limited since the relative intensity weightings of the two components favors the resonant signal. By comparing the spectrum obtained at delay = 0 ps to that taken at delay = 2.1 ps (figure 3.10) however, the effect of non-resonant signal on weaker Raman active bands is quite clear. Besides the strong NO_2 symmetric stretch in the ground state, weaker bands as 1200 and 1115 cm^{-1} also exist that only can be observed when the non-resonant contribution is removed. As will be shown in the next few paragraphs, moving this electric field to minimize the non-resonant has other effects, including a considerable loss of signal compared to that at time zero and increasing experimental resolution to separate closer lying peaks. For now, it can be seen (somewhat) from figure 3.10 that the general signal obtained at the "minimum" position is quite lower for the NO_2 symmetric stretch (its intensity is 1.0 at t=0 vs. 0.063 at t=2.1 ps). At the same minimum position, the contribution from non-resonant signal decreased to essentially zero. The decrease in intensity depends on several experimental parameters with the most important being the natural dephasing time of the vibrational mode in question and the width of the ω_3 electric field. Simulations by other members in our group

(not shown in this thesis) suggest that broader peaks will appear to lose far more intensity for a fixed ω_3 bandwidth on moving from zero to the "minimum" non-resonant position than those with narrower line widths.

A better illustration of the benefit of gained experimental resolution by positioning the ω_3 at the "minimum" non-resonant location is found by examining a simpler molecule than DMPNA and instead focusing on its undimethylated relative, *p*-nitroaniline (PNA). In the case of PNA, two NO_2 symmetric stretches exist very close in frequency to one another in the 1300 cm^{-1} region. Figure 3.11 shows a sample ground state obtained for PNA in acetonitrile with the third electric field positioned to minimize non-resonant signal. Figure 3.12 shows the same ground state spectrum zoomed in on the symmetric NO_2 stretch as well as a simulated spontaneous Raman spectrum numerically simulated from fits at the minimum position. As can be clearly seen in the figure, the peaks are quite resolved in the fs/ps CARS case but barely resolvable in the case of the spontaneous Raman signal as well as having frequencies slightly distorted by the interference of the two strong bands with each other. This feature of fs/ps CARS is very useful in attempting to separate close lying Raman bands that would otherwise be covered in the breadth of stronger intensity peaks. This will be used to examine the close lying hydrogen bonded/non-hydrogen bonded frequencies in the excited state of Coumarin 153 in the next chapter of this thesis.

The theoretical reasoning behind this is a subject of an upcoming paper to be published by another member of the group and thus will not be discussed in this thesis, instead as a matter of completeness, experimental work exemplifying the effect of the ω_3 position on the observed signal in the excited state of DANS will be shown to complete this

section. The experimental scheme is identical to that seen in figure 3.2 with the exception of using only one ω_3 bandwidth.

The results of the experiment are contained in figure 3.13. In this case time zero, $\omega_3(t) = 0$, is defined as the max intensity overlapping of the three CARS electric field in the fs/ps setup (the condition for maximum non-resonant signal). The ω_3 field is scanned in time and a fs/ps CARS spectrum is obtained at each delay and summarized in a contour plot (fig 3.13.b). Since stronger resonant signal exists at later times (ω_3 occurring after the other pulses), the remainder of the graphs focus on time delays that are labeled as negative. It has already been established that there exists a difference in linewidths for modes at $\omega_3(t) = 0$ and those at the minimum of the non-resonant contribution, but figure 3.13.c shows an interesting effect that was not foreseen initially and can complicate the use of this technique if data is acquired at delays later than the minimum of non-resonant. The signal at the minimum (red) is considerably narrower than that obtained at time zero (green) but the data taken at times later than the minimum (blue, $\omega_3(t) = -2.5$ ps) appears even broader than time zero. The shape also appears to differ from that of a simple lorentzian and contains an interference pattern at the central frequency. This effect is real and not an experimental artifact and was seen in both theoretical simulation and higher resolution experiments (not shown) and appears to result from the sinc^2 shaped pulse. The "recurrences" of the electric field, the tiny components seen on both sides of the major intensity component of the ω_3, appear to be the major culprit behind this phenomenon and can present some experimental difficulties if care is not taken to minimize the non-resonant signal (i.e. locate the minimum position).

Monitoring the linewidth obtained at each ω_3 delay provides an excellent way to illustrate the effect of different positions of the ω_3 on the obtained fs/ps CARS signal. Figure

3.13.e presents the full width half max results after applying lorentzian fits to every time delay sampled. The time zero linewidth versus the minimum is easily seen but additionally the behavior at other time delays can provide insight into the complex effect of the position of the third electric field to the actual obtained experimental linewidth. These results are in excellent agreement with the theoretical simulations performed (not shown) by other members in the group.

One final experimental note relates to the separation of vibrationally resonant and non-resonant CARS signal when using fs/ps CARS. One stated advantage of chapter 2 is the removal of background non-resonant signal by careful positioning of the ω_3 electric field. Fig 3.13.d illustrates the experimental realities of this. The non-resonant CARS signal can only exist during the time overlap of the three electric fields, if one of them vanishes; the non-resonant contribution vanishes as well so it is therefore advisable to tailor a third electric field to at some point have zero intensity. The non-resonant contribution is shown as a red line in 3.13.d and the intensity of the 1200 cm^{-1} mode (blue line) at every delay. It is clear that the resonant signal from the 1200 cm^{-1} line appears to be offset from the non-resonant signal and intensity still exists where the electric field reaches zero. This offset is a function of the dephasing time of the vibrational mode as well as the duration of the electric field employed but is always non-zero for vibrationally resonant signal.

3.4 Conclusions

Excited state experiments using pump-fs/ps CARS have shown that the most important determinant for time resolution is the cross correlation between the pump and first two CARS beams. It can be shown that in fact, the most important parameters are the cross

correlation between the pump and the shorter of the first two CARS pulses but the consequence of turning one of the two into a picosecond pulse will result in a decreased spectral range that is accessible via CARS. The time resolution was shown using the excited states of DANS and DMPNA in acetonitrile with excited state lifetimes of ~10 ps and ~600 fs respectively.

An in depth look at the frequency resolution has uncovered that positioning a fixed ω_3 pulse at a time delay designed to minimize the non-resonant contribution increases the spectral resolution of detected signal to improve that obtainable by conventional picosecond CARS and spontaneous Raman spectroscopy. In the experimental (and assuming $sinc^2$ pulses) work several other insights were gleaned, most notably: positioning the ω_3 field maximum later than minimum position results in interference of the outputted signal that should be avoided as much as possible. The relationship between resonant and non-resonant CARS signal is also shown to have an offset in time that is exploited to generate non-resonant free CARS signal. Finally, the increased resolution and background free nature of the fs/ps CARS probe allows for simpler analysis of close lying vibrational modes as well simplifying the complex interference patterns that are common with both non-resonant signal and close lying vibrational modes.

3.5 References

1. Oberlé, J.; Abraham, E.; Ivanov, A.; Jonusauskas, G. and C. Ruilliére, *Journal of Photochemistry and Photobiology A-Chemistry*, 1997, **105**(2-3), p. 217-223.

2. Oberlé, J.; Abraham, E. Jonusauskas, G. and C. Rulliére, *J. Raman Spec.*, 2000, **31**, p. 211.

3. Brakel, R., Mudogo, V. and F. W. Schneider, *J. Chem. Phys.*, 1986, **84**(5), p. 2451.

4. S. A. Payne and R. M. Hochstrasser, *J. Phys. Chem.*, 1986, **90**(10), p. 2068.

5. Hetherington, W. M.; Korenowski, G. M. and K. B. Eisenthal, *Chem. Phys. Lett.*, 1981, **77**(2), p. 275.

6. Ho, F.; Tsay, W. S.; Trout, J.; Velsko, S. and R. M. Hochstrasser R. M., *Chem. Phys. Lett.*, 1983, **97**(2), p. 141-146.

7. Hamaguchi, H. and T. L. Gustafson, *Annu. Rev. Phys. Chem.*, 1994, **45**, p, 593-622 and refs within.

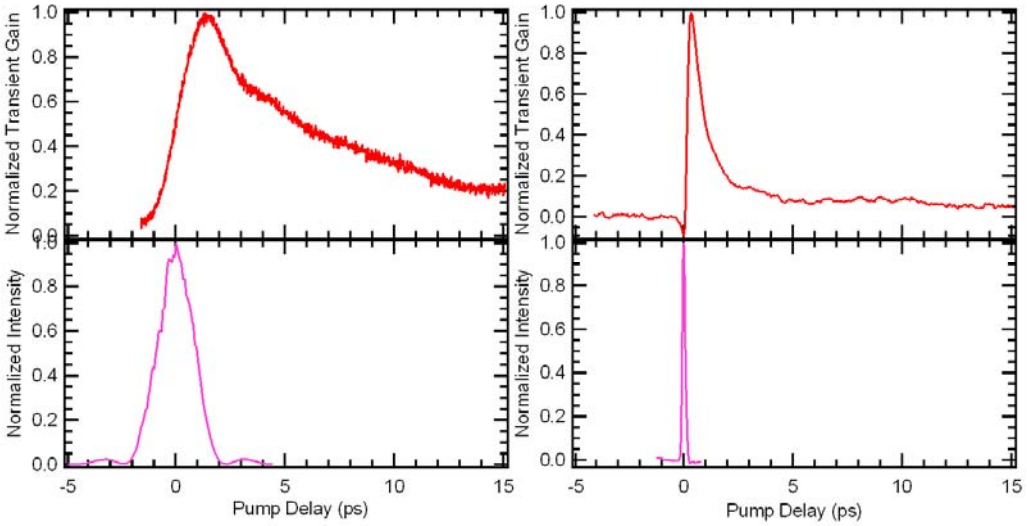

Figure 3.1: Pump-probe transient gain traces (top) of DANS with pump = 400 nm, probe = 800 nm (2.0 ps duration, left panel and 90 fs duration right panels) with electric field traces in bottom panels. With longer probe pulse, the fast decay dynamics observed when using the femtosecond probe are (unsurprisingly) smoothed out over the long duration pulse. Note in this case, the max intensity of the ω_3 field is defined as time zero.

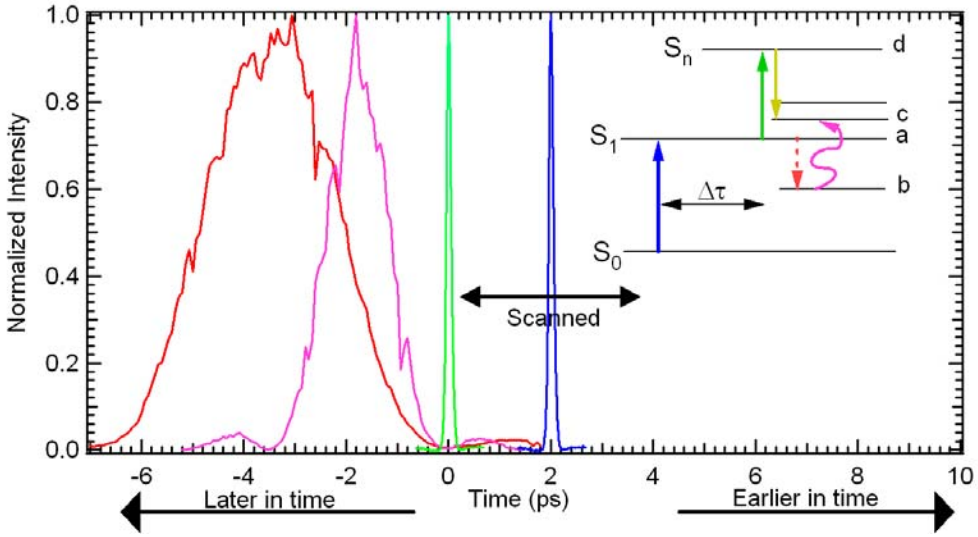

Figure 3.2: Experimental scheme used for observing DANS excited state signal. Main graph shows durations of each electric field used in the pump-CARS experiments. An initial 400 nm (~100 fs) pulse excites DANS into S_1 where some time later (controlled by means of a delay stage) the first two femtosecond pulses (ω_1 and ω_2) populate the excited state vibrational modes of DANS. The final ω_3 pulse then scatters and the fourth wave is generated. Two different ω_3 durations were used. The shorter ω_3 (pink) in the time domain has a bandwidth of about 14 cm^{-1} while the longer duration in the time domain has a bandwidth of about 6 cm^{-1}. The figure in the upper right shows the ladder diagram for this particular molecule. Note in the CARS experiments, the ω_3 field is offset from the ω_1 and ω_2 to reduce non-resonant contributions to the signal, this differs from figure 1 above.

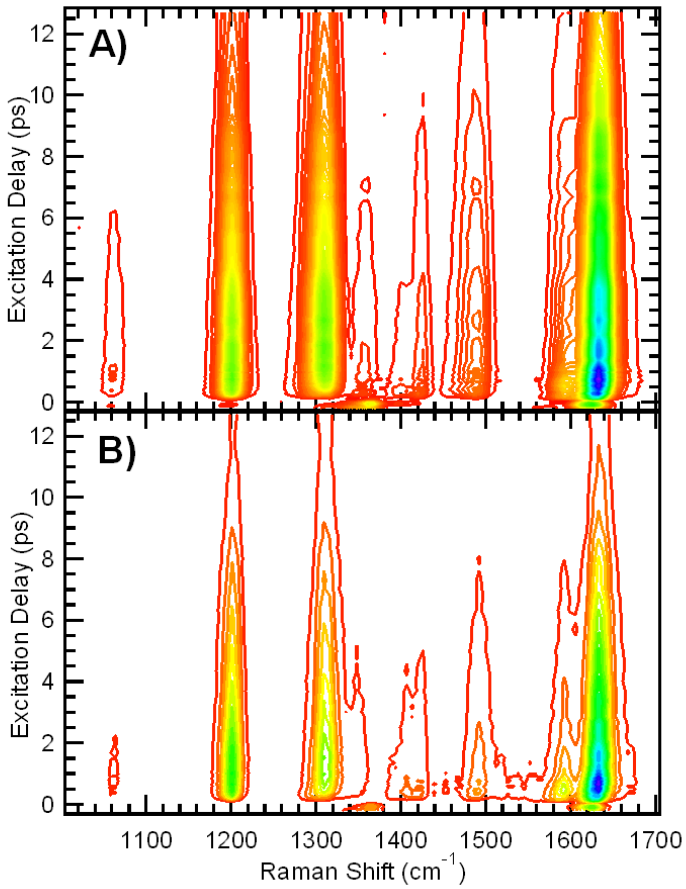

Figure 3.3: Contour plot of excited state DANS signal using the two ω_3 probe pulses. The top contour (A) is the experimental result using the ω_3 bandwidth of 14 cm^{-1} and bottom (B) is for the 6 cm^{-1} bandwidth ω_3. Very similar behavior is observed in intensity dynamics of both experiments.

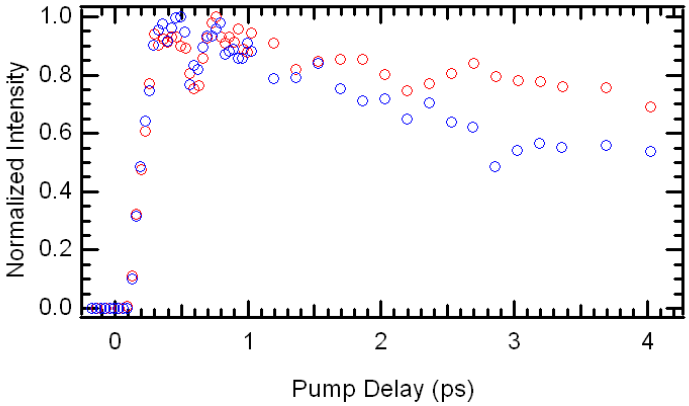

Figure 3.4: Results from fitting the mode near 1480 cm^{-1} to a gaussian lineshape for both experiments. The blue dots are the normalized intensity using $\Delta\omega$ = 6 cm^{-1} and the red dots are using $\Delta\omega$ = 14 cm^{-1}. Of particular emphasis, the rise times of the two separate experiments are very similar despite the slightly noisy decay dynamics.

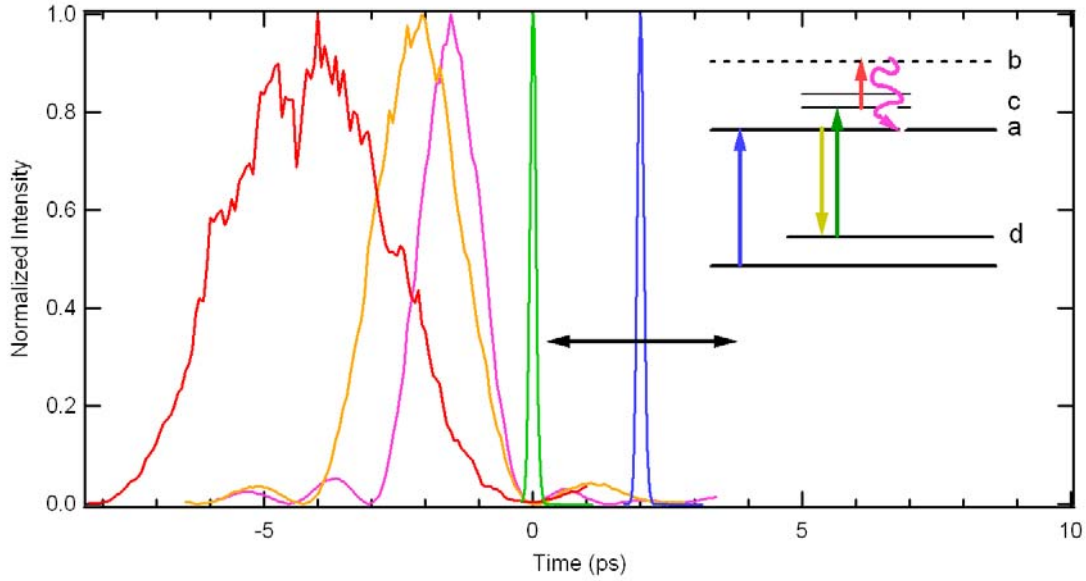

Figure 3.5: Experimental scheme used for the different electric fields of the ω_3 pulse for DMPNA. Three different bandwidths were chosen, 7.5 cm^{-1} (red), 14 cm^{-1} (orange), and 22.5 cm^{-1} (pink). In the upper right is the ladder diagram for obtaining excited state spectra in DMPNA. The 400 nm pulse excites the molecule into its excited state and the two time overlapped ω_1 and ω_2 pulses populate excited state vibrational modes while the ω_3 pulse

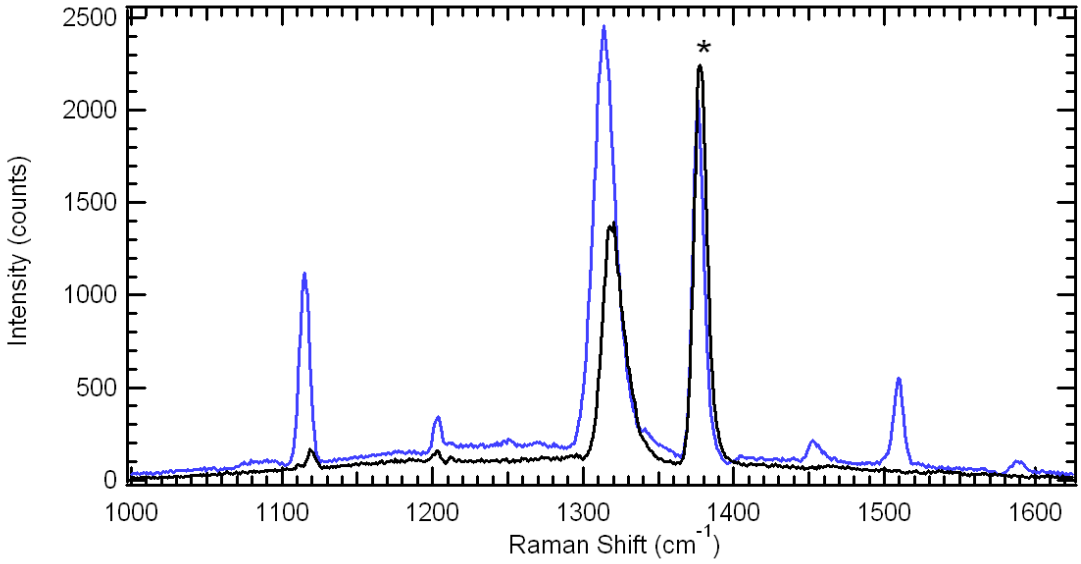

Figure 3.6: Ground (Black) and Excited+Ground(Blue) Spectra of DMPNA in acetonitrile. Excited+Ground State spectrum taken at 110 fs excitation delay with ω_3 bandwidth of 7.5 cm^{-1}. Asterisk denotes solvent band. The excited state features a downshifted NO_2 stretch near 1310 cm^{-1} and strong bands at 1510, 1456, and 1590 cm^{-1}.

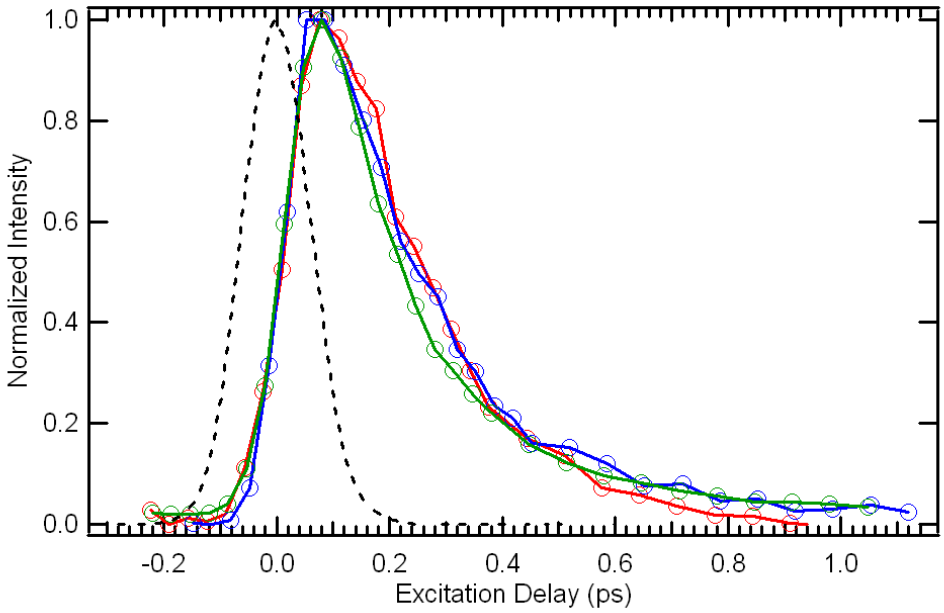

Figure 3.7: Results from fitting the 1510 cm^{-1} band in the excited state to gaussian lineshapes. Different intensities with their respective ω_3 bandwidths are shown with red = 7.5 cm^{-1}, green = 14 cm^{-1}, and blue = 22.5 cm^{-1}. The rise and decay times for this system match quite well despite the significant differences in ω_3 time duration. The black dash is the instrument response function (IRF) and the excited state signal is well modeled as a convolution of a 125 fs IRF and a ~200 fs decay time.

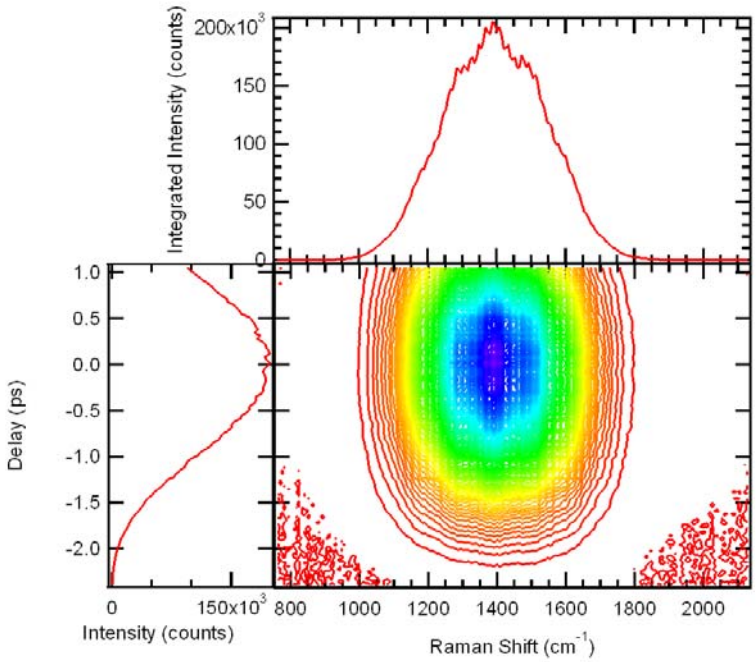

Figure 3.8: Contour plot of pure non-resonant signal obtained using fs/ps CARS in a 150 μm microscope cover slip. Top graph illustrates the spectrum of the non-resonant component (very broad Gaussian-like shape) while the left graph maps out the integrated intensity of the ω_3 electric field relative to its position with respect to the time-overlapped ω_1 and ω_2 pulses at delay = 0 ps.

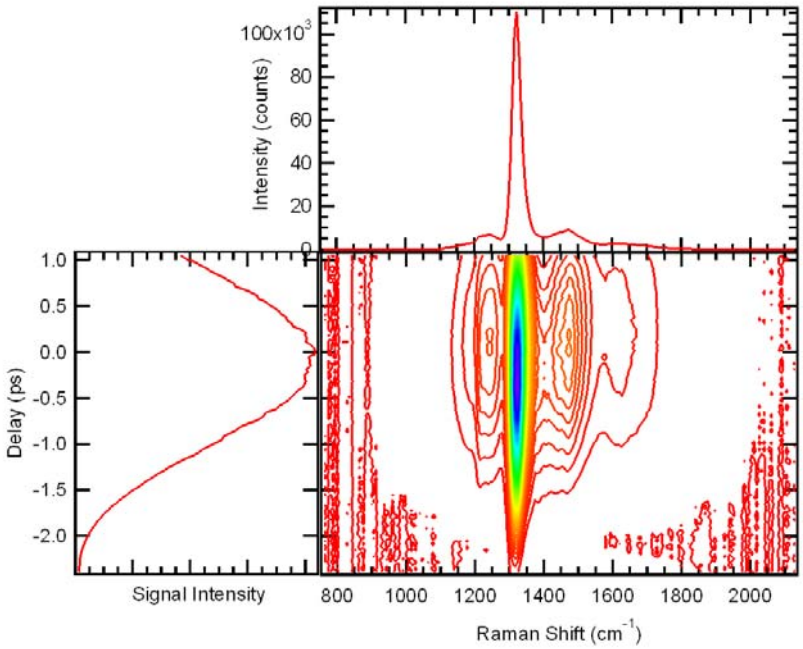

Figure 3.9: Contour plot of the fs/ps CARS experiment scanning the ω_3 electric field in time for DMPNA in the ground electronic state. The strong NO_2 symmetric stretch dominates the signal near 1300 cm^{-1}.

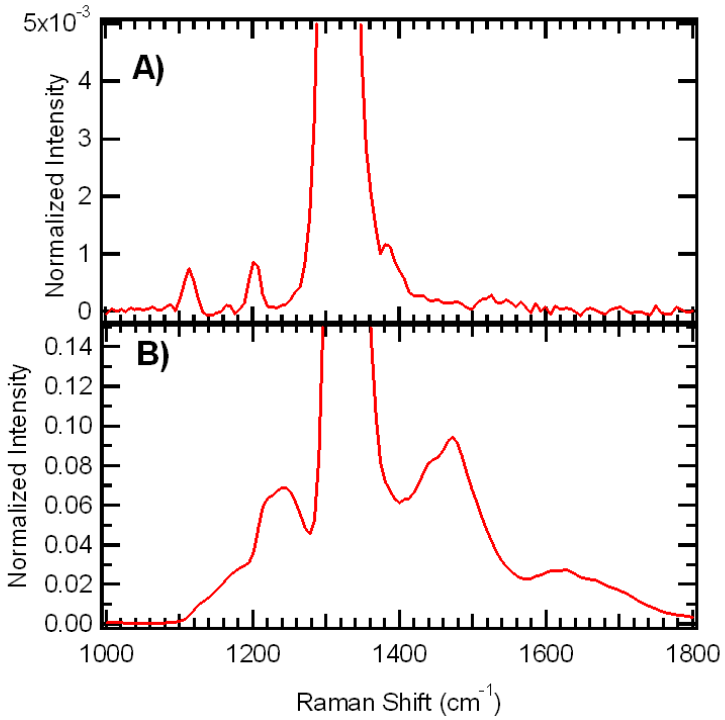

Figure 3.10: fs/ps CARS results for data taken at A) delay = 2.1 ps and B) delay = 0 ps. The weaker contributing Raman bands at 1115 and 1200 cm^{-1} are completely masked in the time zero spectrum under the non-resonant signal.

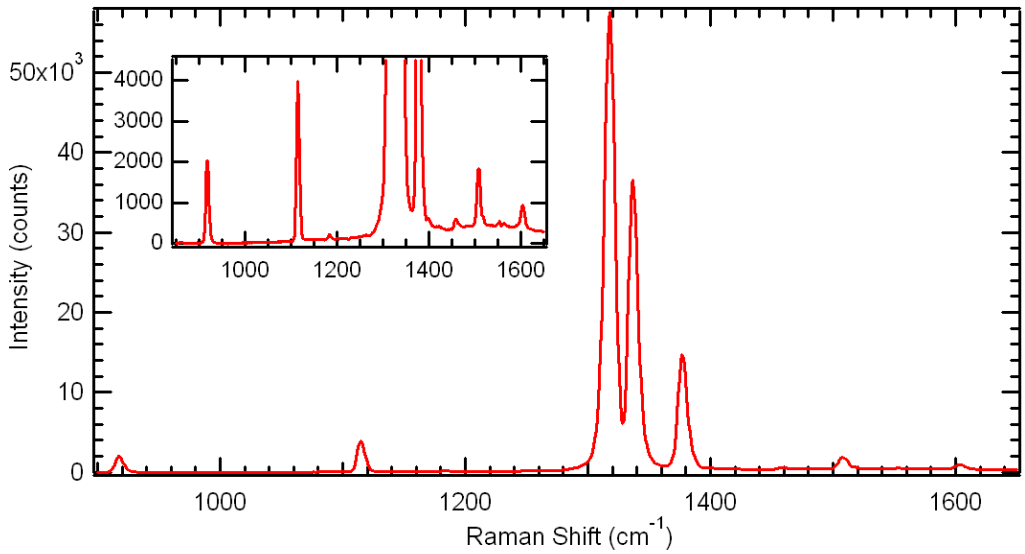

Figure 3.11: Ground state spectrum of PNA in acetonitrile with ω_3 positioned to minimize non-resonant signal. Extremely strong bands are observed at 1318 and 1338 cm^{-1} that relate to NO_2 symmetric stretch frequencies. The inset shows the minor bands of weaker Raman active modes. Acetonitrile bands have not been subtracted and can be seen at 919 cm^{-1} and 1378 cm^{-1}.

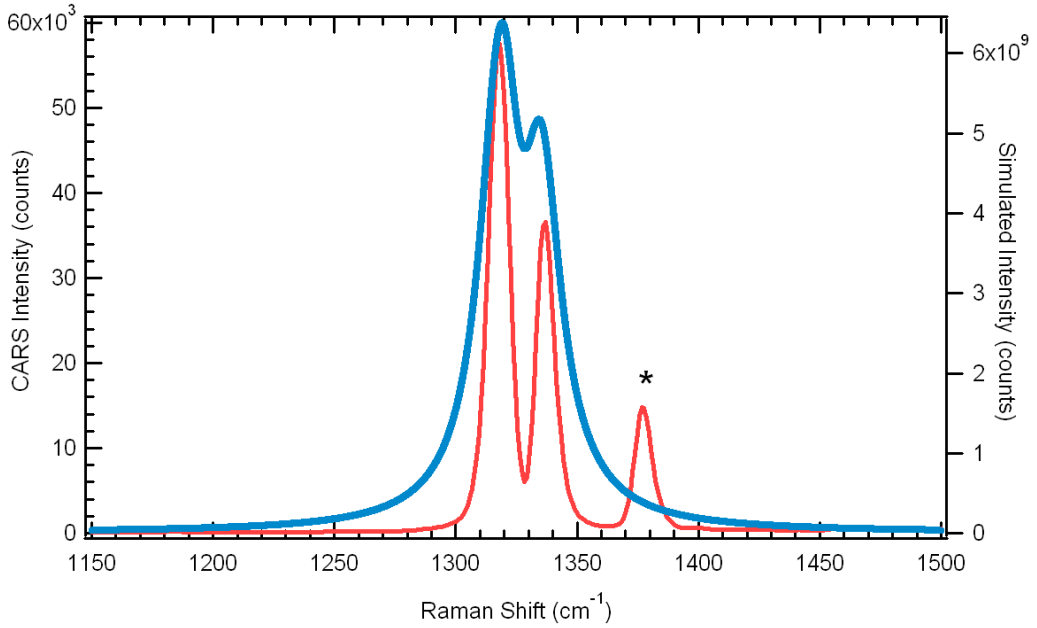

Figure 3.12: fs/ps-CARS data (red, left intensity axis) taken at the minimum non-resonant position and simulated spontaneous Raman result (blue, right intensity axis). When peak intensities are reasonably comparable, the structure can still be somewhat retained at time zero but are far more separate with the increased resolution afforded by fs/ps CARS technique. The acetonitrile is not simulated and is indicated by an asterisk.

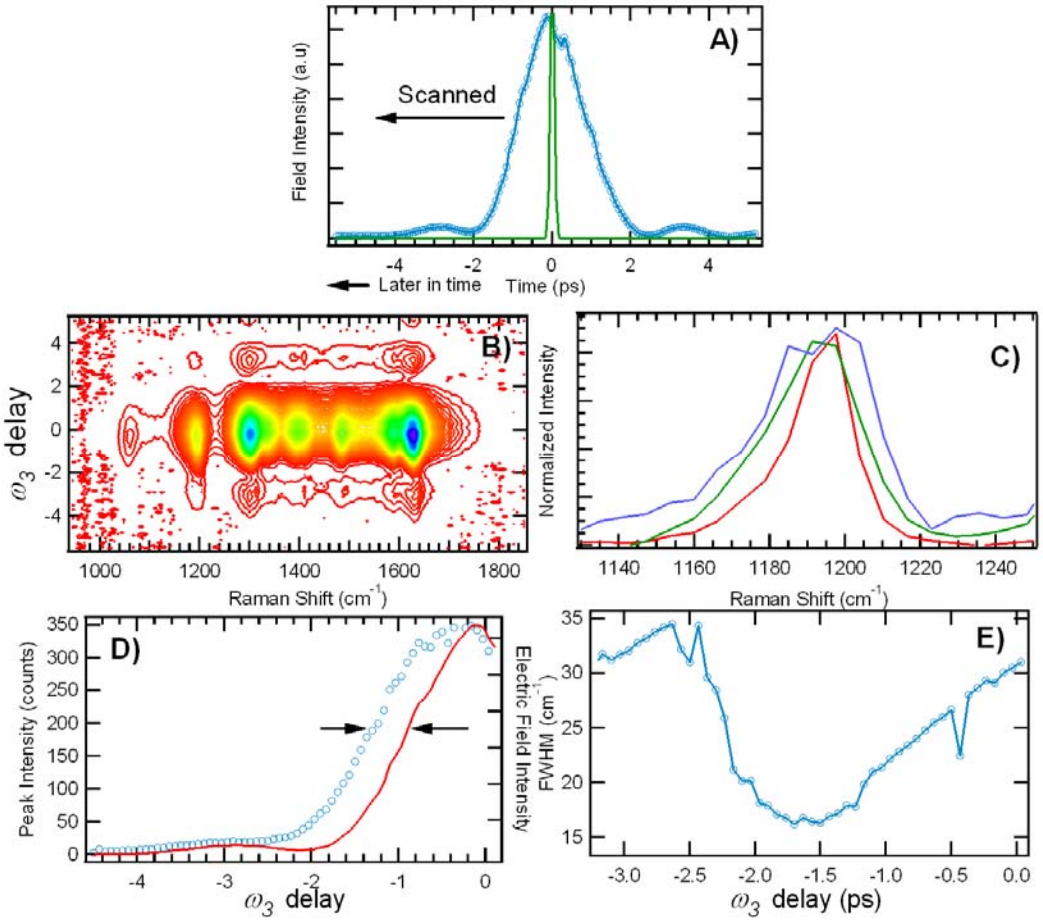

Figure 3.13: fs/ps CARS results for DANS in acetonitrile. In A) the electric field setup used in this experiment is shown. The first two femtosecond CARS pulses and the max intensity overlap of ω_3 are defined as zero. The ps duration field (ω_3) is scanned in time over the fs pulses to generate B). The contour plot displays the resultant spectra acquired at each ω_3 time delay. C) shows the CARS spectra several different delays for the mode near 1200 cm^{-1} (least affected by non-resonant interference). The green curve is taken at $\omega_3(t) = 0$, while the red is taken at $\omega_3(t) = -1.9$ ps, and the blue at $\omega_3(t) = -2.5$ ps. The intensities have been normalized and the double peak behavior observed in the blue is a real effect (see text). D) displays the intensity (blue dots) of the 1200 cm^{-1} mode as a function of ω_3 delay and is plotted with the purely non-resonant component (red line). This offset emphasized by the two arrows allows vibrationally resonant signal to be separated from the non-resonant signal at the $\omega_3(t)$ = "minimum". In E), the fwhm of the 1200 cm^{-1} is shown for each ω_3 time delay to emphasize the difference from time zero and the "minimum". At time zero, the FWHM is ~30 cm^{-1} while at the minimum a value of 17 cm^{-1} is obtained.

CHAPTER 4: ULTRAFAST EXCITED STATE RAMAN INVESTIGATION OF COUMARIN DYES USING A FS/PS CARS PROBE: EXCITED STATE HYDROGEN BONDING DYNAMICS AND AB INITIO CALCULATIONS

A paper submitted to the *Journal of Physical Chemistry A*

Benjamin D. Prince, Abhijit Chakraborty, Beth M. Prince, Mikhail N. Slipchenko,

Mark S. Gordon, and Hans U. Stauffer

4.1 Abstract

The femtosecond/picosecond coherent anti-Stokes Raman scattering (fs/ps CARS) technique is used as a time-resolved probe of electronically excited coumarin 153 (C153) and coumarin 102 (C102) in both hydrogen-bonding and non-hydrogen-bonding solvent environments. The influence of hydrogen bonding on a specific vibrational mode, observed near 1680 cm^{-1} in excited-state C153 and near 1650 cm^{-1} in excited-state C102, is examined in detail. Ab initio calculations at the Hartree-Fock level corroborate the observed frequency differences and allow assignment of this mode to (C=O stretch + lactone ring breathing) in these coumarin species. In both species, this mode shows significant Raman intensity upon electronic excitation and is used as a probe of the time-dependence of hydrogen bonding during excited-state solvation. Particularly for C153 in alcohol solvents (methanol and ethanol), the presence of both H-bonded and non-H-bonded species are directly observed, and the dynamics of the cleaving and subsequent reformation of hydrogen bonds in the excited state (~10 ps timescale in methanol; ~17 ps timescale in ethanol) are addressed.

4.2 Introduction

Given its utility as an essentially rigid solvatochromic species, considerable effort has been devoted to understanding the nature of excited state coumarin 153 (C153, shown in the inset of Fig. 4.1) and its relation to the surrounding solvent environment. Many of these studies focus on the dynamic Stokes shift observed in time-resolved fluorescence measurements, and C153 in particular has been studied extensively in polar and non-polar solvents,[1] ionic liquids,[2-4] micelles,[5,6] and ionic liquids confined within micellar aggregates.[7] A thorough analysis of C153 solvation dynamics monitored via fluorescence upconversion was undertaken by Maroncelli and coworkers[1] for 24 solvents of various characteristics, including aprotic, hydrogen bonding, and aromatic solvents. By monitoring the first moment of the upconverted fluorescence spectrum as a function of time, they followed the spontaneous emission of C153 as a probe of the solvent environment and generated for each solvent a unique set of time constants to quantify the inertial and diffusive components of the solvent response. Notably, timescales associated with protic solvents were found to follow different trends than those observed in aprotic solvents.[1]

More recent studies have focused specifically on the influence of hydrogen bonding networks on the transient solvation dynamics of coumarin dyes. Time-resolved fluorescence studies of several coumarin dyes and Kamlet-Taft analysis of steady-state fluorescence spectra suggest that solvents capable of hydrogen bond donation directly affect the observed solvation timescales.[8-10] While these electronic spectroscopies provide a wealth of information, the dynamics associated with site-specific hydrogen bonds are more directly borne out through direct observation of a select number of vibrational modes directly

affected by H-bonding environments, particularly those involving C=O moieties in C153 and C102.

At a vibrationally state-specific level, Elsaesser and coworkers have carried out pump-transient IR probe experiments on excited state coumarin 102 (C102, inset of Fig. 1), probing the evolution of the pure C=O stretch in H-bonding and non-H-bonding environments.[11-13] They observed a strong ground state redshift of this mode from ~1740 cm^{-1} to ~1700 cm^{-1} in the presence of hydrogen bond donors. Upon excitation in H-bonding solvents, they found a fast (<200 fs) timescale associated with H-bond cleavage.[11] This fast H-bond cleavage has been further corroborated by photon echo experiments.[13] They also observed a continued frequency redshift, which they attributed to a slower solvent-dependent timescale (~1 – 3 ps) associated with solvent rearrangement around the excited state coumarin molecule, but do not discuss any evidence to suggest the reformation of hydrogen bonds in the excited state species. More recently, Palit *et al*. have carried out similar transient IR studies of electronically excited C102 in the hydrogen bonding solvent aniline, also by monitoring the pure C=O stretch.[14] They also observed fast cleavage of the initial H-bond, occurring on timescales faster than their instrumental resolution of 250 fs, but additionally note slower (0.6 ps and 7.2 ps) timescales that they attribute to hydrogen bond reformation with structurally reorganized solvent.

While these transient IR experiments on C102 agree with respect to timescales for H-bond cleavage, differences are noted regarding observed timescales for H-bond reformation during excited-state solvation. Thus, we have carried out studies of the excited states of C153 and C102 using a transient probe designed to detect the complementary Raman active modes in these species, focusing on those modes involving large C=O displacements. These

studies provide further insight into the H-bond accepting nature of these species and the timescales associated with H-bond cleavage and reformation following electronic excitation. We have recently developed the femtosecond/picosecond coherent anti-Stokes Raman spectroscopy (fs/ps CARS) technique in order to probe Raman active vibrations with sub-picosecond time resolution.[15,16] This technique takes advantage of the traditional benefits associated with nonlinear coherent Raman spectroscopies, including the suppression of fluorescence and scattered probe beam light due to the directed nature of the emitted signal beam, dictated by phase matching, as well as the enhancement of excited-state detection sensitivity via multiple electronic resonances. The fs/ps CARS technique provides the additional advantage of non-resonant four-wave mixing signal suppression, by virtue of the optimized timing of the broadband ω_1 and ω_2 probe gating pulses relative to the final ps-duration ω_3 pulse.

In this work, we have used fs/ps CARS to probe the vibrational evolution of C153 following electronic excitation in a variety of solvent environments. In particular, we detail the observation of vibrational modes in electronically excited C153, as well as C102, in the mid-1600 cm^{-1} region that can be clearly attributed to H-bonded species and non-H-bonded species, dependent on solvent environment. These observations are corroborated by ab initio calculations, which allow assignment of the vibrational mode of interest to a strongly Raman-active combined C=O stretch + lactone ring breathing mode in these coumarin species. The dependence of the vibrational frequencies of these modes on solvent environment therefore allows the detection of the evolving (C=O + ring) mode of C153 in the polar protic solvents methanol and ethanol, allowing observation of intermolecular H-bond cleavage and reformation in these H-bonding solvents.

The paper is organized as follows: first, a brief description of the experimental setup, materials, and computational methods used in this work will be presented. Then, evidence is presented for Raman active excited state vibrations in the 1600 cm^{-1} – 1700 cm^{-1} region, existing in both C153 and in C102, the frequencies of which depend strongly on the hydrogen bond donating nature of the solvent environment. These results are then compared to ground electronic state ab initio calculations, which corroborate this solvent-dependent behavior and allow assignment of these modes. Finally, time-resolved studies of C153 evolution in two polar protic solvents are presented, probing this (C=O + ring) mode. These probes allow direct observation of the timescales associated with H-bond cleavage upon initial excitation and subsequent H-bond reformation.

4.3 Experimental Methods

4.3.1 Time-Resolved Optical Probe Technique: Excitation-(fs/ps CARS) Probe

The optical probe setup used in these experiments has been previously described in detail.[15] Briefly, a Ti:Sapphire laser system generates pulses at 800 nm (~50 fs duration) with a 1 kHz repetition rate and pulse powers of ~2 mJ. The pulse is split to generate two ultrafast broadband visible pulses (ω_1 = 19570 cm^{-1} [511 nm]; bandwidth ($\Delta\omega$) = 300 cm^{-1}) and (ω_2 = 18210 cm^{-1} [549 nm]; $\Delta\omega$ = 350 cm^{-1}) via optical parametric amplification and subsequent frequency mixing with the fundamental 800 nm beam. Another portion is used to generate a narrowband, picosecond duration pulse ($\Delta\omega$ = ~8 cm^{-1}) by means of a grating stretcher-compressor setup[17] with an adjustable slit to select the desired bandwidth. A final portion is used to generate a pulse (denoted ω_{ex}) at 400 nm for use as an excitation pulse to allow access to excited state dynamics.

For all of the experimental work described here, the pulse scheme energetics of the excitation-(fs/ps CARS) probe technique are displayed in Fig. 4.1. The ω_{ex} pulse excites the coumarin dye electronically to the S_1 state, whereas a 3-pulse nonlinear optical probe sequence, designated fs/ps CARS, allows multiplexed detection of the excited state CARS spectrum.[15] In these experiments, the ω_1 and ω_2 pulse frequencies are chosen such that the broadband ω_2 pulse is resonant with the $S_1 \rightarrow S_0$ Stokes shifted emission,[1,18] and the broadband ω_1 pulse, which is then resonant with the $S_1 \leftarrow S_0$ transition in the evolving solvent environment, allows access to the 1100 – 1800 cm^{-1} region of the excited-state vibrational spectrum. These resonances therefore enhance the fs/ps CARS detection sensitivity towards the excited state relative to the ground state, since the ω_1 and ω_2 frequencies are preresonant from the equilibrated S_0 state. Finally, the narrowband ω_3 pulse interacts with the sample at a fixed time delay, τ_{23}, relative to the time-overlapped ω_1 and ω_2 pulses. By virtue of the square-pulse frequency-domain mask applied to form the narrowband ω_3 pulse, the time-domain probe pulse envelope, $E_3(t)$, takes the form of a ps-duration sinc function. Thus, τ_{23} is chosen such that the CARS-initiating pulses overlap $E_3(t)$ precisely at the first node preceding the pulse maximum in order to minimize non-resonant contributions to the fs/ps CARS signal.[15] The detected outgoing wave (ω_{CARS}) contains the spectrally resolved vibrational signature of the evolving excited state.[15]

The three fs/ps CARS beams (at frequencies ω_1, ω_2, and ω_3) are directed into the sample using a folded-BOXCARS geometry, and the spatially-filtered output beam is spectrally dispersed and detected using a spectrometer, consisting of a monochromator (Jarrell Ash, f = 300 mm) equipped with a 1200 line/mm grating and a CCD detector

(Princeton Instruments, 1100 element array), resulting in an energy resolution of ~1.2 cm^{-1}/pixel in this frequency range. Spectrometer calibration was carried out using known standard Raman frequencies of toluene and acetonitrile in the 1100 – 1800 cm^{-1} range;[19] absolute measured frequencies reported under these high resolution detection conditions are found to be reproducible to ~2 cm^{-1}. In a few specific cases, described below, a low-resolution detection scheme is used, in which a ~6 cm^{-1}/pixel spectrometer (Ocean Optics USB-2000) is used in place of the high resolution monochromator/CCD detection scheme. The excitation pulse (ω_{ex}) is directed into the sample along the central axis of the BOXCARS geometry, and the delay is adjusted relative to the fs/ps CARS probe pulses via a computer-controlled delay stage. All input beams have parallel polarizations in the experiments described here. Since the ultrafast ω_1 and ω_2 pulses serve as gate pulses to initiate CARS signal output, this scheme allows detection of the CARS spectrum of the evolving system with probe time-resolution dictated by the durations of the ω_{ex}, ω_1, and ω_2 pulses as well as the dephasing lifetimes of the evolving excited state vibrational levels. Therefore, this scheme generates vibrationally-resolved spectra of Raman-active modes while maintaining the sub-picosecond temporal resolution associated with time-resolved CARS.[16,20] In particular, OKE cross-correlation measurements of ω_{ex} with ω_1 and ω_{ex} with ω_2 yield an instrumental response function of 130 fs. The evolution of the detected spectra is monitored as a function of time delay, $\Delta\tau$, between excitation (ω_{ex}) pulse and fs/ps CARS probe initiation pulses (time-overlapped ω_1 and ω_2 pulses).

The optical setup for the fs/ps CARS scheme additionally allows transient gain experiments at the three CARS probe frequencies to be carried out concurrently. In the

transient gain experiments described here, the transmitted ω_2 beam is focused into a Si photodiode detector (Thorlabs DET210) and is isolated using a lock-in amplifier (Stanford Research Systems SR810) triggered at the 500 Hz frequency associated with a mechanical chopper placed in the ω_{ex} beam path.

4.3.2 Materials

All materials were used as purchased. The coumarin dyes C102 and C153 (Exciton) were dissolved to concentrations of 1 – 4 mM in commercially available solvents methanol, (MeOH, HPLC grade), ethanol (EtOH, 99%), *n*-butanol (99.5%), acetonitrile (HPLC grade), acetone (99%) and propylene carbonate (PC, 99%). Additional experiments were performed using 1.0 mM C153 in pure cyclohexane (CH, 99%) as well as 2.3 mM C153 in a phenol (PhOH)/CH mixture containing 150 mM PhOH. To ensure complete sample refreshment on a pulse-to-pulse (1 kHz) basis, sample solutions were placed in the 220 μm gap of a rotating optical cell (~30 Hz) containing two 2″ diam. optical quality fused silica windows. To ascertain the effects of the optical windows on the observed temporal dynamics, additional experiments were carried out employing a windowless, gravity driven liquid jet, based on the design of Tauber, *et al.*[21] No notable differences have been observed in comparing the measured excited-state vibrational frequencies and temporal dynamics results using either the rotating cell or the windowless jet setup.

4.3.3 Computational Methods

Ab initio calculations were performed at the Hartree-Fock (HF) level using the 6-31G(d) basis set[22] to discern the vibrational nature of the ground states of the two coumarin dyes (C153 and C102) studied in this work and to allow assignment of experimentally-observed Raman active modes. All calculations were performed using GAMESS.[23] The basis set was augmented by diffuse functions on selected atoms (numbering scheme and naming scheme of aromatic rings shown in Fig. 4.2) as follows: in both species, diffuse p functions were used on atoms 2, 3, 6-10, 12, 17, 19, and 21; additionally in C153, diffuse p functions were used on fluorine atoms labeled 13-15. The optimized geometries were verified by Hessian calculations, which also yield the relevant harmonic vibrational frequencies; these calculated frequencies were then scaled by 0.8970.[24] Infrared and Raman intensities were determined using the GAMESS default electric field strengths.[25,26]

To approximate H-bonding interactions between C153 and associated solvent molecules, additional calculations were performed in which one ab initio MeOH molecule was located near the expected hydrogen bond location on the carbonyl oxygen (atom 9) of C153. The geometry of the methanol/coumarin system was also optimized at the HF level, again using the 6-31G(d) basis set (augmented by diffuse p functions on the atoms noted above as well as on the methanol C and O atoms); vibrational frequencies were obtained as described above.

4.4 Results and Discussion

4.4.1 Experimental Vibrational Spectra of C153 and C102

Excited state fs/ps CARS spectra of C153 in MeOH and PC in the fingerprint spectral region (1100 – 1750 cm^{-1}) are presented in Fig. 4.3a. These data were taken at an excitation-probe delay, $\Delta\tau$, of ~20 ps; based on time-resolved data discussed in Sec. 4.4.3, these observed frequencies and relative intensities are essentially indicative of the long-time excited state spectra after completion of the molecular response to solvation. These spectra are displayed without subtraction of ground state signal, which is shown in Fig. 4.3b for C153 in MeOH. Note that, due to resonance enhancement associated with the ω_2 and ω_1 pulses (see Fig. 4.1), the measured excited state peak intensities are significantly stronger that those observed in the ground state, particularly in the 1400 – 1800 cm^{-1} region. The excited-state frequencies for C153/MeOH in this region, obtained via first-moment analysis of the observed vibrational peaks, are found to be 1401 cm^{-1}, 1535 cm^{-1}, 1581 cm^{-1}, and 1671 cm^{-1}. In the C153/PC system, the observed excited-state peak frequencies in this region include 1401 cm^{-1}, 1533 cm^{-1}, 1577 cm^{-1}, and 1684 cm^{-1}. Note that the highest frequency peak exhibits the most pronounced solvent dependence, undergoing a 13 cm^{-1} red-shift for C153/MeOH relative to C153/PC. Although not shown here, nearly identical frequencies to that observed in C153/PC are also observed in acetonitrile (at 1685 cm^{-1}) and acetone (at 1686 cm^{-1}), both of which cannot serve as H-bond donors. In contrast, the red-shifted frequency (1671 cm^{-1}) is observed at long excitation-probe delays for C153 in the H-bond donating solvents methanol, ethanol, and *n*-butanol.

Additional experiments were performed to further confirm the solvent dependence on the observed frequency of this C153 vibrational mode. These studies include C153 dissolved in a non-polar solvent (CH) and C153 dissolved in CH in the presence of the H-bond donor PhOH in CH (*i.e.*, C153 in 150 mM PhOH/CH). The fs/ps CARS results for excited state C153 in these solvent environments ($\Delta\tau$ = 30 ps) are shown in Fig. 4.4b, depicted relative to those peaks observed in MeOH and PC, which are reproduced in Fig. 4a. Although these CH and PhOH/CH data were taken under low-resolution spectrometer conditions, the dependence of this vibrational mode on the presence of H-bond donors is clear: C153 in CH shows a non-H-bonding peak near 1684 cm^{-1}, identical to that observed in polar aprotic solvents, whereas the solution spiked with PhOH yields a peak near 1670 cm^{-1}.

As noted above, the time evolution of the pure C=O stretch in electronically excited C102 has been observed via transient IR spectroscopy; this mode is observed near 1740 cm^{-1}, indicating the absence of H-bonding following electronic excitation.[11-14] Given the similarities between C102 and C153 and the results of additional calculations described below, it is not likely that this observed solvent-dependent mode in the 1670 – 1690 cm^{-1} corresponds to a pure C=O stretch. It should also be noted that the 1700 – 1750 cm^{-1} region in the observed excited state spectra (Fig. 4.3) appears completely free of vibrational peaks, suggesting that the pure C=O stretch in the excited state does not exhibit strong Raman activity, in contrast to the strong nature of this peak in the time-resolved IR data.[13] In fact, the pure C=O stretch is also only weakly observed in the ground state of our condensed phase C153 experiments even at greater concentration (~12 mM) and considerable averaging; in MeOH, this ground state peak is observed at 1718 cm^{-1}, whereas a weak pure C=O stretch is

observed near 1740 cm^{-1} in acetonitrile. These observed ground state frequencies are consistent with the analogous C102 frequencies observed by Elsaesser and coworkers.[11-13]

Experiments were also performed for the excited state of C102 in methanol and in PC. The fs/ps CARS results for the excited state at $\Delta\tau = 35$ ps are displayed in Fig. 4.5. The same qualitative solvent-dependent behavior that was observed in C153 is also observed in C102. Most notably, a strong peak is observed near 1642 cm^{-1} for the C102/MeOH system and 1651 cm^{-1} for the C102/PC system. Although this peak frequency is reduced relative to the corresponding peak in C153, it is notable that the hydrogen-bonding redshift observed for this peak in C102 is similar to the ~13 cm^{-1} shift observed in the C153 excited state system.

Comparison of Experimental and Calculated Spectra

To provide further insight regarding the nature of these observed vibrational frequencies in C153, particularly to allow a plausible assignment of the solvent-dependent excited state peaks in the 1670 – 1690 cm^{-1} range noted above, scaled ground state calculated frequencies for gas phase C153 are presented for vibrational modes in the 1500 – 1800 cm^{-1} range in Table 1. The normalized carbonyl oxygen (atom 9 in Fig. 4.2) displacement, here defined as the magnitude (in Å) of the oxygen atom displacement from its equilibrium position in the optimized structure, are also included, since it is expected that modes involving large C=O stretch motions will be most dramatically affected in H-bonding environments. For C153, two calculated modes near 1700 cm^{-1} exhibit large oxygen atom displacement—these include a C=O stretch mode calculated at 1795 cm^{-1} and a C=O stretch + conjugated C=C + lactone ring (labeled by 'L' in Fig. 4.2) breathing motion, hereafter

referred to as (C=O + ring), calculated at 1658 cm^{-1}. The gas phase calculations predict strong IR activity for the pure C=O stretch and strong Raman activity for both of these modes. As noted above, however, the pure C=O stretch in the ground state of the condensed phase C153/MeOH system is particularly weak in the fs/ps CARS spectra, and no analogous frequency is observed within our experimental sensitivity in the excited state spectra. However, similar pure-C=O stretch intensity behavior has been observed by Kiefer and coworkers in studies of both solid and solvated (EtOH solution) coumarin 152 (C152) where observed frequencies are compared with calculations.[27] In the solid phase, the modes involving the C=O stretch vibration are particularly strong, whereas in the condensed phase they exhibit significantly weaker Raman intensities.

Additional ab initio calculations were carried out to approximate a hydrogen-bonding solvent environment and theoretically predict the effect of the solvent on vibrational mode frequencies of the solute. In this case, one MeOH molecule was associated with the C153 or C102 solute, located near the carbonyl oxygen (atom 9 in Fig. 4.2) of C153. The results of these calculations are also displayed in Table 4.1. The most notable effect is the redshift of both the pure C=O stretch and the (C=O + ring) mode. While the calculations generally overestimate the absolute frequency of the pure C=O stretch, the relative hydrogen bond shift (~18 cm^{-1}) in the ground state associated with the presence of MeOH is consistent with experimental observations.[13] Moreover, these calculations suggest that the (C=O + ring) mode is also affected by the presence of MeOH more than is observed for other vibrational modes, although the calculated redshift for this mode in the presence of MeOH is smaller in magnitude than the ~13 cm^{-1} shift observed for the peak appearing the 1680 cm^{-1} range in the observed excited state spectra (Fig. 4.4a). Based on these comparisons of computational and

experimental results, we assign the excited state mode observed at 1671/1684 cm^{-1} to the excited state (C=O + ring) vibrational mode.

The results for the calculated ground state frequencies of gas phase C102 are also presented in Table 4.1 along with differences in mode frequencies between C153 and C102. These calculations predict the combined (C=O + ring) mode frequency in C153 to be 20.6 cm^{-1} greater than that of the analogous mode in C102, whereas the pure C=O stretch frequency is essentially identical for both molecules. This suggests that the nearby fluorine/hydrogen atoms significantly affect the frequency of the (C=O + ring) mode whereas they have little effect on the pure C=O stretch mode. These calculations are consistent with the experimentally observed weak ground state pure C=O stretches for both C102 and C153 (~1718 cm^{-1} observed for both species in H-bonding solvents; ~1736 cm^{-1} observed in non-H-bonding solvents). More importantly, these calculations corroborate the (C=O + ring) mode assignment of the strong excited state peak near 1680 cm^{-1} for C153 and the analogous peak near 1645 cm^{-1} in C102, along with the observed shift in these frequencies associated with H-bonding.

Dynamics of Excited State Hydrogen Bonding in C153

As established above, the excited state C153 vibrational mode observed at ~1684 cm^{-1} in non-hydrogen bond donating solvents and at ~1671 cm^{-1} in H-bond donating solvents, assigned to the (C=O + ring) mode via comparison to ab initio calculations, allows clear discernment of the presence or absence of hydrogen bonds in the electronically excited state. Previous transient IR absorption studies have shown that H-bonds between C102 and protic solvents undergo cleavage in <200 fs following electronic excitation.[13,14] Thus, fs/ps CARS spectra of excited state C153 in MeOH were measured as a function of excitation-

probe time delay, $\Delta\tau$, ranging from $\Delta\tau = 0$ to $\Delta\tau = 60$ ps to discern the temporal dynamics of this C153 vibrational mode in hydrogen bonding solvents. Note that we present here only the temporal dynamics in alcohol solvents, although we have carried out analogous time-resolved experiments for C153 in several polar aprotic solvents, including acetonitrile and PC. In these aprotic solvents, while we observe a slow intensity growth of the observed peaks in this region (~3 ps timescale in acetonitrile and ~15 ps timescale in PC), there are negligible changes in observed peak lineshapes and frequencies throughout the timescales during which dynamic Stokes shifts are observed.[1]

In contrast, complex dynamics involving multiple peaks are observed in the polar protic solvents, MeOH and EtOH. For example, Fig. 6 depicts the excited state fs/ps CARS spectrum of C153 in MeOH in the 1620 – 1760 cm^{-1} region for selected excitation-probe delays. The data near zero excitation times clearly show a pronounced band for the (C=O + ring) mode at the frequency near that observed in C153/PC (1684 cm^{-1}, as depicted by a dashed vertical line in Fig. 6) with a small contribution from a peak near the final frequency observed in MeOH at significantly later excitation times. As the excited state evolves, the ratio of free C153 (*i.e.*, near the final observed C153/PC frequency) to H-bonded C153 (*i.e.*, near the final C153/MeOH frequency) clearly changes to favor the hydrogen bonded (C=O + ring) configuration. Additionally, at early times ($\Delta\tau < 2$ ps), a third peak appears as a shoulder, centered near 1690 cm^{-1}, blue-shifted relative to the non-H-bonded peak.

To quantify the evolution of this mode following electronic excitation in MeOH, the frequency-dependent intensities, $I_{CARS}(\omega)$, in the region of this observed (C=O + ring) mode were fit to the following functional form:

$$I_{\mathrm{CARS}}(\omega) = \left| \sum_{j=1}^{N} \frac{A_j}{\left(i\left(\omega_j - \omega\right) + \Gamma_j\right)^2} \right|^2 \qquad (4.1),$$

where A_j, ω_j, and Γ_j, represent, respectively, the amplitude, frequency, and decay constant of the j^{th} observed vibrational mode, assuming these vibrations exhibit purely homogeneous broadening. Such a functional form is valid for fs/ps CARS signal in which the slowly rising edge of the picosecond duration $E_3(t)$ is approximately linear over the vibrational decay timescales, Γ_j^{-1}.[16] The measured amplitude coefficients, A_j, are in turn proportional to the density of the initial state from which the CARS signal initiates, and the product of the four transition dipole moments associated with the electronic resonances depicted in Fig. 4.1.[28]

Least squares fits were carried out for all observed time delays using the functional form shown in Eq. (4.1); for delays in which three distinct peaks were clearly observed, ($\Delta\tau$ < 2 ps), three sets of parameters, A_j, ω_j, and Γ_j, were allowed to freely vary to obtain optimal fits to the observed data. At longer delays, ($\Delta\tau$ > 5 ps), optimal fits could only be obtained assuming the presence of two distinct peaks, centered near 1671 cm^{-1} (H-bonded (C=O + ring) frequency) and 1684 cm^{-1} (non-H-bonded (C=O + ring) frequency). For intermediate time delays between these two extreme cases, the blue-shifted peak frequency and decay constant were held constant, allowing only the amplitude coefficient of this peak to vary during least squares fitting. An example of a typical fit is shown for the 3.0 ps excitation delay in C153/MeOH (dashed curve in Fig. 4.6). The obtained amplitude coefficients, A_j, for these peaks are depicted in Fig. 4.7b. Example error bars based on the standard deviations obtained from the least squares fits are shown for several representative points. Comparison of these amplitudes to the measured transient gain signal observed at the ω_2 frequency

(depicted in Fig. 4.7a) suggest that the early-time intensity dynamics are modulated at least to some extent by the proximity of the fs/ps CARS probe frequencies, ω_1 and ω_2, to the evolving Stokes-shifted electronic transition between the ground and excited states of C153. The H-bonded peak amplitude dynamics clearly suggest the reformation of H-bonded species following electronic excitation. When normalized by the observed transient gain intensities at the ω_1 and ω_2 frequencies to take into account the evolving Franck-Condon overlaps associated with the Stokes-shifted emission, these amplitudes show a single exponential growth of the purely H-bonded peak governed by a 10.3 ± 0.8 ps rise time.

Similarly, we have measured the temporal evolution of peaks in this spectral range for C153 dissolved in EtOH; the data observed from 1620 – 1760 cm^{-1} are shown for several excitation delays in Fig. 4.8. As was observed in MeOH solvent, three distinct peaks, including one near the equilibrated H-bonded (C=O + ring) frequency (1671 cm^{-1}), one near the (C=O + ring) frequency observed in both CH and PC solvents (1684 cm^{-1}), and an additional blue-shifted third peak near 1690 cm^{-1}, are observed in varying relative intensities during the excited state C153 evolution. This blue-shifted peak is apparent over a much longer time range in EtOH, clearly observable as a shoulder until ~9 ps. This appearance of this additional blue-shifted peak observed in EtOH (and weakly in C153/MeOH at the earliest times, as discussed above) suggests that some fraction of the C153 molecules experience a very weak solvent interaction at the earliest times. At later excitation-probe delays, a disappearance of the non-H-bonded components are readily observed, whereas the final H-bonded component dominates at long times. Comparing Fig. 4.6 to Fig. 4.8, C153 shows a notably slower increase in the ratio of H-bonded to non-H-bonded species in EtOH than in MeOH.

These data were fit in analogous fashion to the C153/MeOH data, using least squares fits to the functional form shown in Eq. (4.1); in this case, the third blue-shifted peak was included for the first 15 ps, at which point the fits were carried out assuming only the presence of two peaks (*i.e.*, near the H-bonded frequency of 1671 cm^{-1} and the non-H-bonded frequency of 1684 cm^{-1}). A typical three peak fit is shown in Fig. 4.8 for the data at 3.0 ps (dashed curve). The evolution of the transient gain-scaled amplitude coefficients for C153 in EtOH is shown in Fig. 4.9. While the dynamics associated with the two highest energy peaks in this region exhibit multiple decay timescales, the rise of the purely H-bonded component fits to a 17.3 ± 1.6 ps timescale.

Fluorescence upconversion experiments performed by Horng *et al.* monitoring the dynamic Stokes shift of C153 in various solvents upon excitation presented the shift in alcohol solvents as a function of a four exponential fit.[1] For MeOH and EtOH, the longest timescales seem to appear closest to the rise observed in this experiment for the appearance with a final component of 15.3 and 29.6 ps respectively. While the timescales of ~10 ps and 17 ps attributed here to H-bond formation are shorter than this longest timescale observed in upconversion experiments they follow similar trends regarding the relative timescales in these two protic solvents.

In transient IR studies of a similar coumarin species, C102, in H-bond donating environments, Elsaesser and coworkers note a <200 fs timescale for H-bond cleavage upon electronic excitation.[13] In our results, the lack of an observable ground state (C=O + ring) mode, along with the dependence of the observed fs/ps CARS signal on the evolving resonance frequencies, make it difficult to ascribe a timescale to this initial cleavage. However, non-H-bonding peaks are present directly upon electronic excitation, and the

intensities of these peaks increase on timescales concomitant with the growth of transient gain signal. This suggests that the data observed here is consistent with an essentially instantaneous cleavage of H-bonds upon electronic excitation. As noted above, Elsaesser *et al*. do not discuss timescales for H-bond reformation within the excited state.

More recently, Palit and coworkers observed a biphasic reformation of intermolecular H-bonds between C102 and aniline solvent, observing a fast (0.6 ps) and a slower (7.1 ps) timescale associated with this process. This fastest timescale is attributed to the initial formation of "dangling" H-bonds due to incomplete early solvation, followed by a secondary timescale associated with diffusive reorientation of the first solvent shell surrounding the H-bond acceptor.[14] In the C153 data described here, the spectral resolution afforded by the fs/ps CARS probe technique allows clear observation of two discrete non-H-bonded peaks in this region. This observation is consistent with the initial formation of "dangling" H-bonds with minimal association with the surrounding solvent at early times. In both C153/MeOH and C153/EtOH, blue-shifted shoulders relative to the peaks observed in non-H-bonding solvents such as PC and CH are clearly observed, decaying on fast timescales (~ 0.9 ps in MeOH; ~2 ps in EtOH). While the two remaining peaks, attributed to H-bonded excited state species (evolving to frequencies of 1671 cm^{-1} in both solvents) and species associated with the surrounding solvent shell but lacking a site-specific H-bond (observed at frequencies near 1684 cm^{-1}), exhibit more complex growth and decay dynamics, the long-timescale appearance of the H-bonded frequency (10.3 ± 0.8 ps in MeOH and 17.3 ± 1.6 ps in EtOH) are consistent with the reformation of H-bonds in these protic solvents during diffusional reorientation of these solvents.

4.5 Conclusions

The fs/ps CARS technique has been used to probe, in the vibrational fingerprint region, the excited state vibrational spectra of C153 and C102 in a variety of solvent environments. In particular, an excited state vibrational mode is observed in these coumarin species that is dependent on the hydrogen bond donating properties of the solvent. Ab initio calculations allow assignment of this mode to a C=O + lactone ring breathing vibration, whereas the pure C=O stretch peak is not observed in the excited states of these species using this probe technique.

Studies of the temporal evolution of the vibrational spectrum of C153 in MeOH and EtOH depict clearly resolved peaks in this region, corresponding to the presence of at least two distinct types of solvated species upon electronic excitation. The excellent spectral resolution afforded by this probe technique allows the observation of these environment-dependent modes, despite the fact that their observed frequencies differ by only 10 – 13 cm^{-1}. In addition to a peak near the equilibrated H-bonded frequency as well as a peak observed at the equilibrated non-H-bonding solvent frequency, an additional blue-shifted peak is observed in both MeOH and EtOH solvents at early excitation-probe delays, suggesting that both a free (C=O + ring) mode and a solvent-associated (C=O + ring) mode are present upon initial excitation. At long delays in both solvents, the reformation of H-bonds with the solvent environment occurs on approximately 10 ps and 17 ps timescales, respectively, in MeOH and EtOH solvent; these timescales follow similar trends to those observed for the longest timescale components observed in fluorescence upconversion experiments, often attributed to diffusive reorientation of the H-bonding solvent around the excited state species.

4.6 Acknowledgments

Support from Ames Laboratory is gratefully acknowledged. We thank Steve Bradforth and his group for assistance in constructing the gravity-driven liquid jet and Tse-Ming Hsin for his contributions to the preliminary studies associated with this work.

4.7 References

1. Horng, M. L.; Gardecki, J. A.; Papazyan, A.; Maroncelli, M. *J. Phys. Chem.* **1995**, *99*, 17311.

2. Karmakar, R.; Samanta, A. *J. Phys. Chem. A* **2002**, *106*, 4447.

3. Chowdhury, P. K.; Halder, M.; Sanders, L.; Calhoun, T.; Anderson, J. L.; Armstrong, D. W.; Song, X.; Petrich, J. W. *J. Phys. Chem. B* **2004**, *108*, 10245.

4. Karmakar, R.; Samanta, A. *J. Phys. Chem. A* **2002**, *106*, 6670.

5. Chakrabarty, D.; Chakraborty, A.; Seth, D.; Hazra, P.; Sarkar, N. *Chem. Phys. Lett.* **2005**, *412*, 255.

6. Grant, C. D.; Steege, K. E.; Bunagan, M. R.; Castner, E. W. *J. Phys. Chem. B* **2005**, *109*, 22273.

7. Chakraborty, A.; Seth, D.; Chakrabarty, D.; Setua, P.; Sarkar, N. *J. Phys. Chem. A* **2005**, *109*, 11110.

8. Das, K.; Jain, B.; Patel, H. S. *J. Phys. Chem. A* **2006**, *110*, 1698.

9. Gustavsson, T.; Cassara, L.; Gulbinas, V.; Gurzadyan, G.; Mialocq, J. C.; Pommeret, S.; Sorgius, M.; van der Meulen, P. *J. Phys. Chem. A* **1998**, *102*, 4229.

10. Królicki, R.; Jarzeba, W.; Mostafavi, M.; Lampre, I. *J. Phys. Chem. A* **2002**, *106*, 1708.

11. Chudoba, C.; Nibbering, E. T. J.; Elsaesser, T. *Phys. Rev. Lett.* **1998**, *81*, 3010.

12. Chudoba, C.; Nibbering, E. T. J.; Elsaesser, T. *J. Phys. Chem. A* **1999**, *103*, 5625.

13. Nibbering, E. T. J.; Tschirschwitz, F.; Chudoba, C.; Elsaesser, T. *J. Phys. Chem. A* **2000**, *104*, 4236.

14. Palit, D. K.; Zhang, T. Q.; Kumazaki, S.; Yoshihara, K. *J. Phys. Chem. A* **2003**, *107*, 10798.

15. Prince, B. D.; Chakraborty, A.; Prince, B. M.; Stauffer, H. U. *J. Chem. Phys.* **2006**, *125*, 044502.

16. Prince, B. M.; Prince, B. D.; Slipchenko, M. N.; Stauffer, H. U. *manuscript in preparation; to be submitted to J. Chem. Phys.* **2007**.

17. Weiner, A. M. *Rev. Sci. Instrum.* **2000**, *71*, 1929.

18. Kovalenko, S. A.; Ruthmann, J.; Ernsting, N. P. *Chem. Phys. Lett.* **1997**, *271*, 40.

19. McCreery, R. L. Raman Shift Frequency Standards; URL: http://www.chemistry.ohio-state.edu/~rmccreer/freqcorr/shift.html#shiftdir, 2007.

20. Prince, B. D.; Prince, B. M.; Slipchenko, M. N.; Stauffer, H. U. *manuscript in preparation; to be submitted to J. Chem. Phys.* **2007**.

21. Tauber, M. J.; Mathies, R. A.; Chen, X. Y.; Bradforth, S. E. *Rev. Sci. Instrum.* **2003**, *74*, 4958.

22. Roothan, C. C. J. *Rev. Mod. Phys.* **1951**, *23*, 69.

23. Schmidt, M. W.; Baldridge, K. K.; Boatz, J. A.; Elbert, S. T.; Gordon, M. S.; Jensen, J. H.; Koseki, S.; Matsunaga, N.; Nguyen, K. A.; Su, S. J.; Windus, T. L.; Dupuis, M.; Montgomery, J. A. *J. Comp. Chem.* **1993**, *14*, 1347.

24. Young, D. C. *Computational Chemistry: A Practical Guide for Applying Techniques to Real World Problems*; Wiley, 2001.

25. Bacskay, G. B.; Saebo, S.; Taylor, P. R. *Chem. Phys.* **1984**, *90*, 215.

26. Komornicki, A.; McIver, J. W. *J. Chem. Phys.* **1979**, *70*, 2014.

27. Vogel, E.; Gbureck, A.; Kiefer, W. *J. Molec. Struct.* **2000**, *550*, 177.

28. Mukamel, S. *Principles of Nonlinear Optical Spectroscopy*; Oxford University Press: New York, 1995.

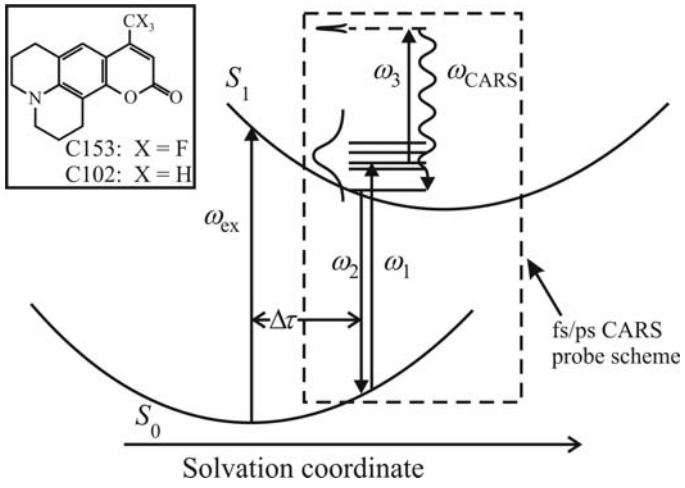

Fig. 4.1: Excitation-(fs/ps CARS) probe scheme employed in these experiments on C153 and C102 (depicted in inset). A pulse at 400 nm (ω_{ex}) electronically excites the coumarin molecules. After a time delay, $\Delta\tau$, the optimized fs/ps CARS probe allows detection of excited-state CARS spectra of the evolved coumarin/solvent environment. This probe scheme consists of broadband ω_2 (~550 nm) and ω_1 (~510 nm) pulses that initiate the CARS probe process and a narrowband ω_3 pulse (~800 nm) that completes the three input pulse interactions and scatters the output ω_{CARS} field, which is spectrally dispersed to reveal the vibrationally resolved CARS spectrum. The optimized relative timings of the ω_1, ω_2, and ω_3 pulses are fixed in these experiments; therefore, only $\Delta\tau$ is adjusted to probe the temporal dynamics of the vibrationally-resolved excited state CARS spectrum.

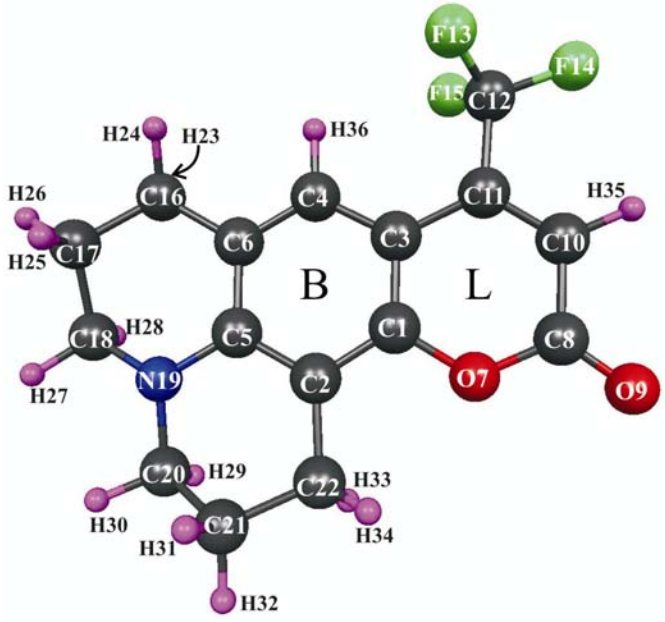

Fig. 4.2: Optimized structure of C153 in the ground state, depicting the numbering scheme used in the text. The following color scheme is used: black—carbon atoms; red—oxygen atoms; blue—nitrogen atom; green—fluorine atoms; pink—hydrogen atoms (hydrogen 23 is obscured by carbon 16). The numbering scheme employed for coumarin 102 is identical except that C153 fluorines 13, 14, and 15 are replaced by hydrogens labeled 13, 14, and 15. The benzene (B) and lactone (L) rings, used to describe calculated vibrational modes, are labeled as such.

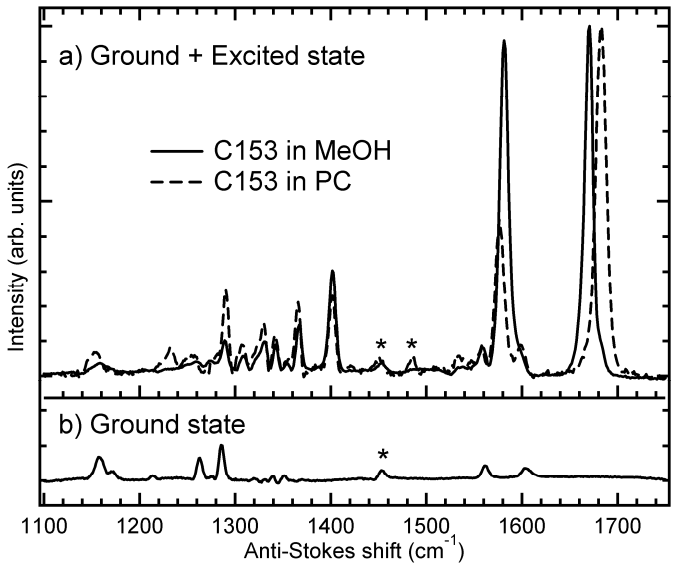

Fig. 4.3: Experimental fs/ps CARS spectra of the 1100-1750 cm^{-1} region for C153 in methanol (MeOH, solid curve) and propylene carbonate (PC, dashed curve): a) Excited state + ground state spectra taken at a long-time excitation-probe delay ($\Delta\tau$ = 20 ps). Discussion in the text focuses on the highest observed frequency in this range (1671 cm^{-1} for C153/MeOH; 1684 cm^{-1} for C153/PC); b) Ground state spectrum in MeOH; note that the relative scales of a) and b) are left unchanged to depict the observed relative intensities of ground and excited state peaks. The asterisks (*) denote solvent peaks.

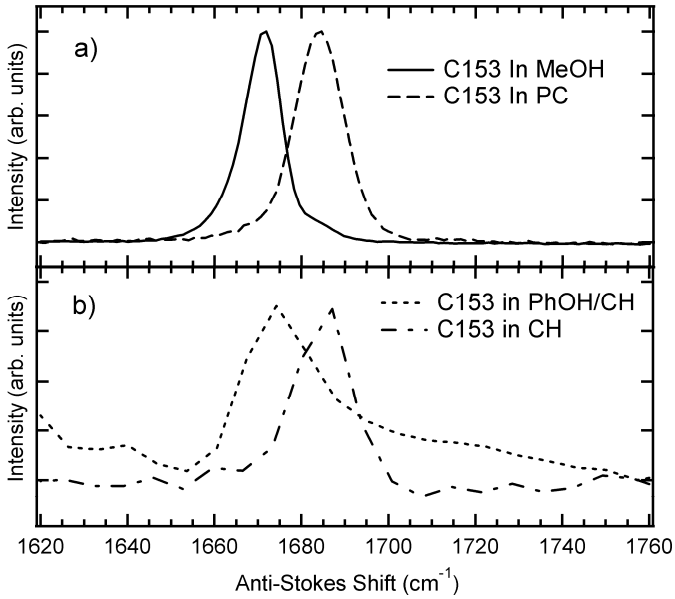

Fig. 4.4: a) Expanded view of excited-state fs/ps CARS spectra of C153 in MeOH (solid curve) and PC (dashed curve) at excitation-probe delay, $\Delta\tau$, of 20 ps. b) Low-resolution fs/ps CARS spectra of C153 in PhOH/CH (dotted curve) and CH (dotted-dashed curve) at excitation-probe delay, $\Delta\tau$ = 30 ps. A large red-shift (from 1684 cm^{-1} to ~1670 cm^{-1}) is observed in the presence of the H-bonding phenol, analogous to results observed in pure H-bonding solvents.

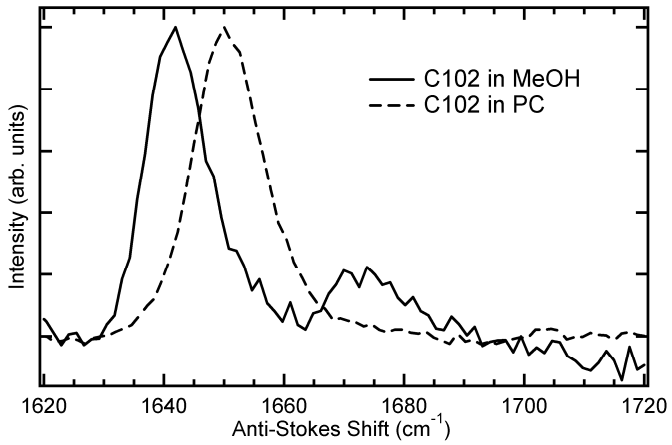

Fig. 4.5: Solvent dependence of excited state fs/ps CARS spectra of C102 at $\Delta\tau = 35$ ps excitation-probe delay in methanol (solid curve) and in propylene carbonate (dashed curve). The observed peaks are at 1642 cm^{-1} and 1651 cm^{-1} respectively. The frequency red-shift in the presence of hydrogen-bonding solvent is quite similar to that observed for C153 solutions (~13 cm^{-1}).

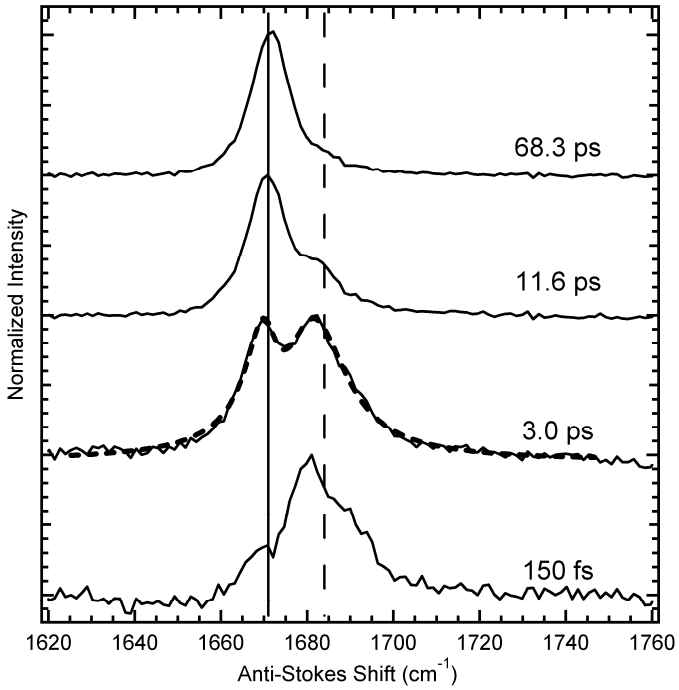

Fig. 4.6: Excited state fs/ps CARS spectra in the mid-1600 cm^{-1} range for C153 in methanol. Data shown for four specific excitation-probe delay times, including 150 fs, 3.0 ps, 11.6 ps, and 68.3 ps; these signals have been offset for clarity and have all been normalized to a uniform peak intensity for this figure. Both the non-H-bonded species and the H-bonded species can be clearly observed in these data, the relative intensities of which evolve in time. Bold dashed curve on 3.0 ps data show the quality of the least squares fitting of these data to the squared magnitude of the sum of two complex Lorentzian lineshapes, as detailed in the text. For reference, vertical lines depict long-time equilibrated frequencies observed in this region for C153 in methanol (1671 cm^{-1}, solid line) and in both propylene carbonate and cyclohexane (1684 cm^{-1}, dashed line).

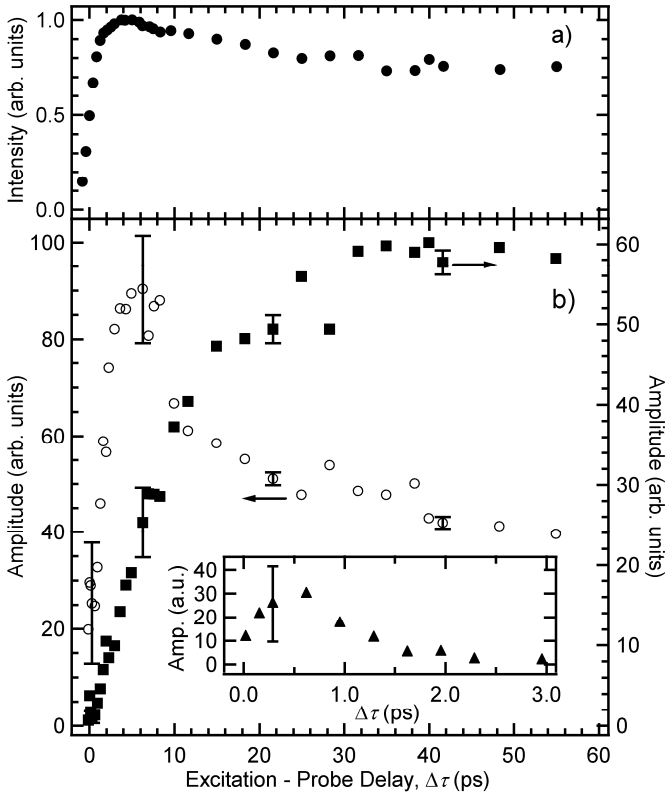

Fig. 4.7: a) Transient gain data for C153 in MeOH measured at the ω_2 pulse frequency (549 nm); b) Peak evolution as a function of electronic excitation-fs/ps CARS probe delay for non-H-bonded (open circles, left axis) and H-bonded (filled squares, right axis) for C153 in methanol. Inset depicts evolution of additional blue-shifted peak observed near 1690 cm^{-1} at early delays. Data correspond to state amplitude coefficients, A_j, extracted from least squares fitting to the functional form described in the text. Error bars represent uncertainties associated with least squares fitting, depicting the typical fit quality at several time delays.

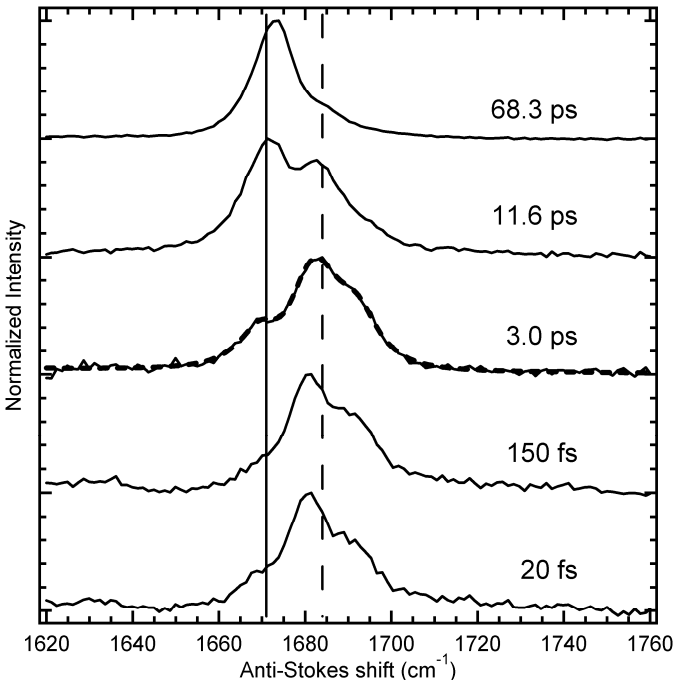

Fig. 4.8: Excited state fs/ps CARS spectra in the mid-1600 cm^{-1} range for C153 in ethanol. Data shown for five specific excitation-probe delay times, including 20 fs, 150 fs, 3.0 ps, 11.6 ps, and 68.3 ps; these signals have been offset for clarity and have all been normalized to a uniform peak intensity for this figure. Bold dashed curve on 3.0 ps data shows a least squares fitting of these data to the squared magnitude of the sum of two complex Lorentzian lineshapes, as detailed in the text. For reference, vertical lines depict long-time equilibrated frequencies observed in this region for C153 in methanol (1671 cm^{-1}, solid line) and in both propylene carbonate and cyclohexane (1684 cm^{-1}, dashed line).

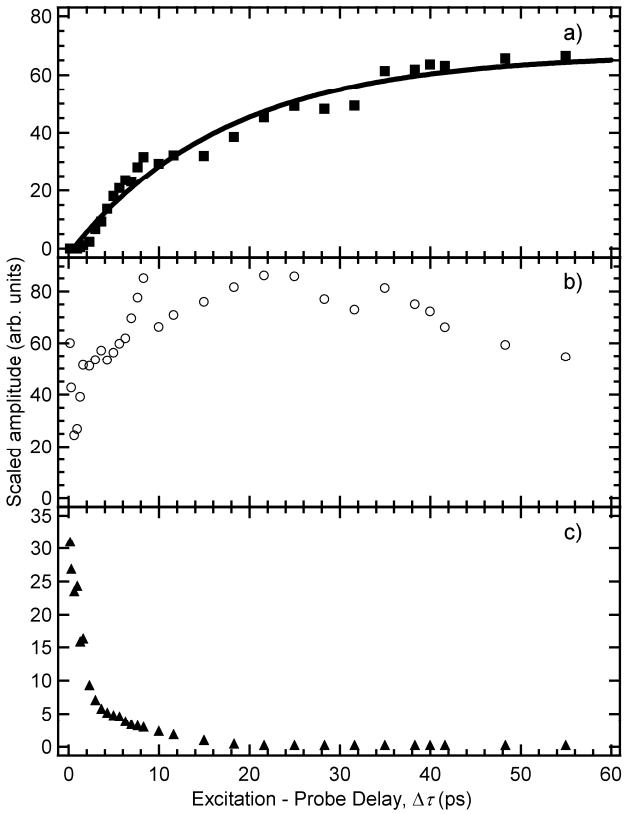

Fig. 4.9: Peak amplitude evolution for C153 in ethanol. Amplitudes shown as a function of electronic excitation-fs/ps CARS probe delay for H-bonded mode near 1671 cm^{-1} (panel a) and two apparent non-H-bonded modes near 1684 cm^{-1} (panel b) and near 1690 cm^{-1} (panel c). Data correspond to state amplitude coefficients extracted from least square fitting to the squared magnitude of a sum of complex Lorentzian lineshapes, subsequently scaled by the observed fluorescence intensity, as described in the text. Solid curve corresponds to an exponential fit to the H-bonded peak, yielding a 17.3 ± 1.6 ps long timescale rise.

TABLE 4.1: Ground state C153 Calculated Frequencies and Predicted Spectroscopic Activities

Mode	Mode description	Freq.[a)]	Raman Int.[b)]	IR Int.[c)]	O9 Disp.[d)]	Freq.[a)] (MeOH present)	Frequency Difference Due to MeOH	C102 Freq.[a)]	C153 – C102 Freq. Diff.
90	H_2C18 & H_2C20 scissor	1508.3	14.2	0.91	0.002	1509.1	0.8	1499.6	8.8
91	C-C(B) + C-C(L) str.	1570.1	282.7	2.91	0.006	1568.9	-1.2	1565.5	4.6
92	C-C(B) str.	1614.7	589.7	11.45	0.013	1612.7	-2.0	1611.5	3.2
93	C8-O9 + C-C(L) str.	1657.8	255.1	0.28	0.039	1653.9	-3.8	1637.2	20.6
94	C8-O9 str.	1795.3	186.1	23.66	0.142	1776.4	-18.9	1795.5	-0.2

a) Scaled (by 0.8970) calculated frequency (freq.) (in cm^{-1})
b) Predicted Raman intensity (Int.), in $Å^4$/amu.
c) Predicted infrared intensity, in $D^2/(amu \cdot Å^2)$
d) Displacement (Å) defined as the square root of the squares of the Cartesian displacements $(x^2 + y^2 + z^2)^{½}$

CHAPTER 5: ULTRAFAST EXCITED STATE RAMAN INVESTIGATION OF COUMARIN DYES USING A FS/PS CARS PROBE: EXCITED STATE INTENSITY DYNAMICS

Benjamin D. Prince, Abhijit Chakraborty, Mikhail N. Slipchenko,

and Hans U. Stauffer

5.1 Abstract

The excited state population dynamics of the first singlet state in coumarin 153, 35, and 102 are probed via pump-fs/ps CARS and transient gain spectroscopy. Slow solvent dependent rise times of the acquired CARS signal are rationalized in terms of excess energy and solvent reorganization effects on the hyperpolarizability and thus Raman intensity of the observed signal. These effects appear to be absent in the completely non-polar cyclohexane but observed in polar solvents with timescales that seem to correlate with known longer time solvent reorganization times.

5.2 Experimental Methods

5.2.1 Pump-fs/ps CARS

Full details of the instrument setup can be found in chapter 2. Briefly, a Ti:Sapphire laser system generates 800nm pulses of ~ 50 fs duration with a 1 kHz repetition rate and pulse powers of 2.1 mJ. The pulse is beam split to generate two femtosecond broadband visible pulses (ω_1 = 515 nm, 19420 cm^{-1}) and (ω_2 = 555 nm, 18020 cm^{-1}) via optical parametric amplification and subsequent frequency mixing with the fundamental 800 nm. A second portion is used to generate a narrowband, ps pulse ($\Delta\omega$ = ~ 16 cm^{-1}) by means of a

grating-stretcher setup with an adjustable slit to select the desired bandwidth. A final portion is used to generate a 400 nm pulse (ω_{ex}) for use as a pump pulse in excited state experimental work.

For all of the experimental work performed using the pump-fs/ps CARS technique, the pulse scheme energetics are identical to those displayed in chapter 4 figure 1. Schematically, the 400 nm beam excites the coumarin dye electronically to S_1 where the ω_2 pulse is resonant with the $S_0 \leftarrow S_1$ transition. The time overlapped ω_1 pulse is then resonant with the $S_1 \leftarrow S_0$ transition. Finally, the non-resonant ω_3 pulse interacts with the sample and a fourth wave (ω_{CARS}) is scattered and detected. All beams had identical polarizations in these experiments.

The three CARS beams (ω_1, ω_2, and ω_3) are directed into the sample using the folded-BOXCAR geometry and the spatially filtered output beam is directed and focused into a spectrometer (Ocean Optics USB-2000, 0.7 nm resolution). The pump pulse (ω_{ex}) is directed into the sample and the delay is managed via a computer controlled delay stage. This scheme generates vibrationally resolved spectra of Raman active modes while maintaining sub-picosecond temporal resolution associated with time resolved CARS. Due to the bandwidth of the ω_3 pulse and the limited spectral resolution of the spectrometer, the detected ω_{CARS} signal is processed by fitting to gaussian lineshapes to monitor the time evolution of the detected Raman peaks in terms of frequencies, intensities, linewidths and integrated intensities as a function of excitation (ω_{ex}) time delay. Given the detection setup, the experimentally obtained frequencies are expected to be certain within 6 cm^{-1}.

5.2.2 Transient Gain Experiments

Transient gain experiments were employed that monitored the electronic resonances from S_1 by using the 400 nm excitation beam as a pump and either the ω_1 or ω_2 pulse as a probe. The gain signal was detected by means of a photodiode and directed into a lock-in amplifier synchronized to an optical chopper located in the excitation beam pathway. An additional setup was also used in a pump-dump-probe style experiment where 400 nm excitation is used as a pump, ω_2 as a dump and ω_1 as the probe with the ω_2 pulse (dump) being chopped. The polarization conditions were matched to the conditions employed in the fs/ps CARS experiments (parallel) to facilitate direct comparison.

5.2.3 Materials

Coumarin 102, 153, and 35 were used as purchased from Exciton. Generally solutions of about 2-6 mM were made by dissolving in commercially available solvents which included methanol, acetonitrile, acetone, propylene carbonate, cyclohexane and butanol and had optical densities of 0.7 to 1.5 OD at 400 nm. The samples were held in a motorized rotating sample cell with 2 mm thick fused silica windows with a 220 μm spacer where the sample was inserted to completely refresh each laser shot..

Typical beam powers were about 2-6 uJ for the excitation beam in all of the coumarins. ω_1 was typically held below 1 μJ and ω_2 varied from approximately 1 μJ for C153 to 4 μJ in C102. The non-resonant ω_3 pulse was generally about 3 μJ in all experiments.

5.3 Results

5.3.1 Static Absorption/Emission and Time-resolved Transient Gain

The static absorption and steady state emission spectra for the three coumarins are displayed in Figure 5.1. All three coumarins absorb strongly near 400 nm with absorption maxes occurring at 421 nm for C153, 391 nm for C102, and 400 nm for C35. Approximating the low energy FWHM energy as the 0-0 transition, the amount of excess energy applied for the various coumarins can be predicted. For C153, the low energy FWHM is located at 457 nm, and would result in approximately 3100 cm^{-1} excess energy input as a result of 400 nm excitation. Using the same methodology, C35 excitation would result in approximately 2000 cm^{-1} excess and 900 cm^{-1} excess for C102. Fluorescence maxes in methanol occur at 564 nm for C153 and 488 nm for C102.

Transient gain experiments were performed for both ω_1 and ω_2 in the various solvents and coumarins. Figure 5.2 displays the transient gain results for C153 in methanol and propylene carbonate. Pulse limited rise times constitute the earliest timescales for these traces and a generally faster decay is observed for the ω_1 pulse than the ω_2 as the solvation process occurs. Since the focus of this study is not on the electronic transitions themselves (transient absorption/transient gain) and instead on the vibrational behavior of the solute after electronic excitation and owing to the breadth of the study on the dynamic stokes shift for coumarin dyes, the transient gain spectra are used only as a guide for predicting the relative strength of the resonances employed in the pump-fs/ps CARS experiments detailed below.

Given the pulse sequence used to generate excited state spectra for pump-fs/ps CARS in this experiment, the strength of the ω_1 transition after the interaction with the ω_2 pulse is of interest as it may contribute to the observed dynamics. To probe this resonance, a

pump/dump/probe experiment was employed that detected the ω_1 pulse while the ω_2 pulse was chopped, time-overlapped and used as a dump pulse from the $S_0 \leftarrow S_1$ transition. The results of this experiment are displayed in figure 5.3 for C153/MeOH. The resulting data is generated as a function of the ω_1 signal with and without the time-overlapped ω_2 dump pulse as a function of the ω_{exc} delay. In the absence of the ω_2 pulse, the ω_1 pulse shows transient gain signal (see gray dotted line in Figure 5.2). When the ω_2 pulse is present, it appears to attenuate the ω_1 signal at a constant value (within experimental noise) but no time dependence or increased absorption (transient absorption) as a function of time.

5.3.2 Pump-fs/ps CARS results

5.3.2.1 Coumarin 153

A typical pump-fs/ps CARS spectrum generated is displayed in figure 5.4 for C153 in methanol solvent. Several fingerprint region Raman active ground state modes (solid) are observable without inclusion of the excitation beam. Excited state spectra (dotted) are recorded when the excitation beam is present. In the figure, the excited state spectra at pump-CARS delay of 20 ps is presented. The excited state is the resulting spectra observed with the ground state contribution subtracted off. Several excited state frequencies are observed in this range including ~1674, 1584, 1400, and 1366 cm^{-1} for the region studied in this experiment.

The intensity evolution of these modes as a function of pump delay is portrayed in figure 5.5 for C153 in methanol. Assuming Gaussian spectral profiles for the Raman peaks, the resulting statistical information with regards to intensity, frequency, and full width half max (FWHM) are plotted. A generally slow growth timescale is found for all prominent modes, which does not fit well to any simple exponential timescales (roughly fit to 9 ps). Max value is attained in 20-25 ps, where typically a long slow decay is observed. The

FWHM character of these modes suggests for the most part that there is little change for the 1584/1400 modes as a function of pump-probe delay but the 1674 mode experiences a much broader initial character before settling at about 20 cm^{-1} at long times. The only notable frequency evolution of these prominent modes is found in the 1674 mode where a large upshift in frequency (~12 cm^{-1}) is detected at very early times (sub-ps) before a downshift of approximately 4 cm^{-1} over a scale of picoseconds.

For simplification, the mode near the 1700 cm^{-1}, assigned as C=O+C=C symmetric stretch in chapter 4, (1671 in alcohols, 1684 in non-alcohols) region is used as the representative mode for each C153/solvent system. The resulting intensity profiles for a variety of solvents are displayed in the upper panels of figure 5.6 with x-axes that differ for each C153/solvent system. Additionally, the lower panel of each solvent system depicts the electronic transient gain spectra of the ω_1 and ω_2 used in each respective experiment. The intensity profiles depicted have not removed the concentration squared dependence of CARS intensity and thus must be thought of as the population squared behavior of the excited state population. The solvent dependant intensity profiles with the fastest rise time's solvents are the acetonitrile and acetone solvents with exponential timescales of approx 4 ps and 3 ps respectively while the slowest studied is butanol with a single exponential timescale of approximately 50 ps. It is clearly seen that in every case with the exception of cyclohexane, the transient gain spectra rise faster than the CARS data. The rise response of the ω_1 transient gain trace is always pulse limited and usually has a solvent dependent decay profile (this is a function of the fluorescence band dynamically shifting to longer wavelengths). If the ω_2 trace was to be used as a template of how CARS intensity should be observed, a small rise time should be observed in every solvent.

5.3.2.2 Coumarin 102 and Coumarin 35

Example spectra from the ground and excited state of C102 using fs/ps CARS are displayed in figure 5.7. Similar modes are observed in the ground state of C102 as were found in C153 (~1560 and 1600 cm^{-1}). The prominent excited state peaks are located at 1638 and 1559 cm^{-1} respectively (compare figure 5.4). Like the alcohol/non-alcohol character of the C=O+C=C mode in C153, C102 has a band at 1638 cm^{-1} for the alcohols studied and a band at 1651 for the non-alcohols, and is assigned to the same mode downshifted compared to C153. The intensity profile of the C102 C=O+C=C mode for MeOH/PC is displayed in figure 5.8. Rise times are well fit to a single exponential with a tau value of 4.4 ps.

To fully compare the three dyes, experiments were undertaken to find the role of excess energy in the coumarin molecules versus one fixed solvent system. The choice of solvent was methanol which allows for a slower response time (in C153) and allows the greatest signal to noise setup for the laser system being used (due to the strongly red shifted fluorescence for these three coumarins). A comparison of the excited state spectra obtained at 45 ps excitation time is shown in figure 5.9. The excited state spectrum of C35 is very similar to that obtained for C153 which strongly differ from the spectrum obtained in C102 in the 1650 region. Figure 5.10 shows the comparison of the 1650 region intensities for these three coumarins as a function of excitation delay. A clear difference is observed in the rise times with the C153/MeOH system rising the slowest and C102/MeOH the quickest.

Discussion

The transient gain experiments offer insight into the existence of the molecular resonance which these experiments utilize. As has been observed in other work using coherent Raman spectroscopy on excited state species[1-5], the detected signal is directly correlated to the strength and existence of these resonances. Considerable effort has been employed in both experiment and theory on C153 to elucidate the fundamental solvent reorganization dynamics upon electronic excitation. Experimental work using fluorescence upconversion, super-continuum transient gain and non-resonant degenerate four wave mixing techniques have been used to elucidate reorganization times[6-10]. The transient gain slices shown here are not meant to provide insight into the solvent reorganization dynamics directly (as only a small portion of an evolving system is selected) but to gauge the strength and existence of the resonances which will affect the signal detected using pump-fs/ps CARS. It is sufficient to say here, that for all experiments, the ω_2 beam at 555 nm is typically a constant value upon rising for the entirety of the timescales monitored in this experiment.

What might be expected for the pump-fs/ps CARS signal is for the intensity traces to follow the resonance of ω_2 (or in other words, map out the transient gain trace for ω_2). This was the expectation at the beginning of the experiments. The results for C153 intensities suggest that this is far from the case as each solvent generates its own timescale, which is always much slower than the observed transient gain trace for the solute/solvent system. Given the distinct solvent dependence on timescales, it would not be hard to invoke the solvation process as a rationale for the unique timescales. While some solvents (notably the alcohols) mesh reasonably well with solvation timescales measured in other experiments, most notably the fluorescence upconversion experiments of ref 8 and the transient grating

experiments of ref 7, there is a distinct slowness of the fs/ps CARS results for all non-alcohol solvents. More concerning, however, is that the observed solute modes which are being monitored here are dependent on the solvent being essentially finished with the solvation process, by comparing to known long time solvent reorganization timescales (see ref. 8), in C153 before the maximum signal is observed. This becomes even more complicated when the results of C102 with regard to methanol and propylene carbonate are examined. C102 is electronically very similar to C153/C35 with three hydrogens replacing three fluorines, however, the dipole moment change is very similar for these systems[11]. It might be expected that C102 would then undergo the same dipole-dipole dominated solvation dynamics as C153 and C35 and the intensity of the observed peaks would mirror the results found for C153/solvent systems. In the solvents studied here, the intensity growth of the peaks is always faster in C102 versus C153 with C35 being the intermediate suggesting that either the solvation process is not the whole answer or it is related to another process completely.

A possible explanation for the peak intensities is that the signal may rely instead on the second field interaction (the ω_1 pulse). While the ω_2 transient gain traces suggest a nearly constant signal level (in methanol), it is possible that the resonance to reabsorb from $S_1 \leftarrow S_0$* and generate the excited state signal varies as a function of time between the pump and the time-overlapped ω_1 and ω_2 pulses. To test this possibility, the pump-dump-probe experiments were performed. If the signal depended on an increasing resonance of the ω_1 pulse at late times (seen through an increasingly negative going difference between dump on/dump off over tens of picoseconds) compared to early times, it should manifest itself by showing a marked decrease in the transient gain signal of the ω_1 pulse (because of extra absorption) at late times compared to those of early times. The difference wave only shows a

slight difference at the very earliest times, suggesting that the ω_1 re-absorption process upon ω_2 dumping is essentially equally strong throughout the timescales studied here. This would presumably remove the argument that the signal comes from the complicated resonance scheme employed.

Another possibility is that since both field interactions are resonant from the excited state to the ground state, potentially the signal observed is that of a vibrationally hot (excited vibrational) ground state (potentially labeled as S_0') being accessed by coherences generated after both initial (ω_1 and ω_2) field interactions act in a downward fashion as in the right side of figure 5.11. The resulting signal would then increase with time because the overlap with the ground potential would presumably increase as the solvent environment equilibrates around the excited state coumarin dipole environment. This is a difficult possibility to experimentally separate but several other experimental observations suggest some difficulties with this hypothesis. The first issue is the established decay times of Ernsting and coworkers of a vibrationally hot ground state relaxing to the ground vibrational state of the S_0' potential are on a sub 80 fs timescale[12]. If the hot ground state were observed a linewidth on the order of 100 fs, would result in a roughly 75 cm^{-1} detected linewidths. This would be in contrast to the observed linewidths in the near 20-30 cm^{-1} regime. A second issue would arrive from the difficulty in the observed peak frequencies. If the modes observed would result in overtone frequencies, it would require that the anharmonicity of the C=O stretch to be smaller for the hydrogen bonding mode than the non-hydrogen bonded mode. The C=O stretch is the only mode observed above 1650 cm^{-1} in C153, and is 1738 cm^{-1} in the non-hydrogen bonded case and 1720 cm^{-1} in the hydrogen bonded case (compare C153 excited state as 1674/1687). For completeness, the mode detected as 1674/1687 is not believed to be the C=O stretch, but

instead a combination band involving the C=O and the conjugated double bond. The justification for this is found in the previous chapter and details the hydrogen bonding characteristics of these coumarin dyes.

Given the decreasing nature of the timescales for intensity growth for the three coumarin dyes in methanol as less excess energy is pumped and the finding of Ernsting and co-workers in references 9 and 12 of Raman active excited state modes detected in PSCP experiments with frequencies of 1590 cm^{-1} and 1400 cm^{-1} (both frequencies observed within experimental error in the fs/ps CARS experiments), we believe that we are observing the $\nu = 1 \leftarrow 0$ vibrational state of the evolving/equilibrated excited electronic state. The slowness in the growth reflects the excess energy placed into the coumarin dyes, where C153 with the most excess requires the largest amount of time to get population into the lowest vibrational states. Considering the nearly 9-10 ps rise time for C153, roughly 6 ps for C35 and 3.4 ps for C102 as well as the approximate 3100 cm^{-1} excess energy for C153, 2000 for C35 and 900 cm^{-1} for C102 upon electronic excitation at 400 nm, one could expect potentially 2 quanta of 1674 and 1584 to be populated initially as the molecule undergoes the very rapid IVR often assumed for large molecules, one quanta for the C35 species and the excess is below the threshold that would result in overtone quanta being populated for C102. It is obvious from figure 6 that the slow growth is not solely responsible from the excess energy applied to the solute/solvent system which should show methanol and acetonitrile with very similar timescales. There is an obvious solvent dependence on these timescales so a model in which the relaxation involves only intramolecular pathways cannot be reasonably fashioned, one must then turn to a solvent assisted relaxation process.

We believe the timescales measured reflect a timescale which includes energy transfer from the excited vibrational manifold of the coumarin dyes to solvent modes of the respective solvents. It would appear the solvation times of the solvents are of importance, suggesting that vibrational energy transfer may be more efficient once solvent reorganization is completed (we measure no timescale faster than the 1/e times for solvation reported in reference 8). A study of vibrational energy transfer from an excited electronic solute with initial vibrational energy in vibronically coupled modes (presumably one to a few modes) to a solvent undergoing reorganization due to dipole-dipole interactions has not been undertaken to the authors' attention. We emphasize the apparent importance of the solvation process equilibrating because of the unexpected results obtained for C153 in cyclohexane. It is understood that cyclohexane experiences no to little dynamic stokes shift upon excitation of the coumarin due to its non-polar nature, however, as noted in reference 8, no spectral relaxation is observed due to excess energy. The same appears to be evident with the fs/ps CARS data. 400 nm excitation is accessing a higher lying vibrational state according to the absorption spectrum but the relaxation appears to be very quick or non-existent in the fs/ps CARS data. It would then appear that either cyclohexane is a stronger coupled solvent in terms of vibrational energy transfer from solute to solvent, the actual process of reorganizing for the polar solvents influences (i.e. slows down) the vibrational energy transfer efficiency, or some other intermolecular interaction is dynamically involved in signal strength.

An interesting area of emerging research discusses the importance of the solvent on the solute dipole[13-15] and its influence on the hyper-polarizability of organic molecules. While cyclohexane has little concern for changes in either magnitude or direction of the coumarin dye's excited state dipole, the other solvent molecules are dynamically effected by

changes in direction (and possibly magnitude) of the dipole vector. It is well known that molecules with larger hyper-polarizabilities result in generally larger Raman signal. If one could define a dynamic hyper-polarizability as polarizability that changes as a function of solvent reorganization, it could be expected that a molecule, such as coumarin, would show a time dependant Raman intensity profile until an equilibrium is restored.

This postulated response alone cannot be used to completely explain the results observed here because the experiments on the three coumarin dyes in an identical solvent (methanol) should show an identical behavior since all three coumarin dyes have very similar dipole angle and magnitude changes. It is clear that excess energy has some role that is not completely yet understood.

5.5 Conclusions

The intensity behavior of the excited state peaks observed in coumarins 153, 35, and 102 has been probed by pump-fs/ps CARS. The behavior of all solvents with any polar character show a slow rising component that is far slower than the transient gain detected in electronic spectroscopies. Utilizing the same solvent, a pattern of rise times has been observed that seem to correlate with amount of excess energy. Excess energy cannot be the sole cause of the slow rising signal as C153 in cyclohexane shows an immediate rise which maps out exactly the transient gain results despite having excess energy. An additional component of the molecular response has been hypothesized that involves the change dynamically of the hyper-polarizability as a function of solvent response. This dynamic hyper-polarizability should mirror the behavior of the solvent response in that it should no

longer be dynamic when the solvent has returned to an equilibrium condition in its now lowest energy conformation of the new excited state coumarin molecule.

5.6 References

1. Nagae, H.; Kuki, M.; Zhang, J.; Mukai, Y.; and Y. Koyama, *J. Phys. Chem. A*, 2000, **104**, p. 4155.

2. Yoshizawa, M.; Aoko, H. and H. Hashimoto, *Phys. Rev.*, 2001, **63**: 013808/1.

3. Hogiu, S.; Werncke, W.; Pfeiffer, M.; and T. Elsaesser, *Chem. Phys. Lett.,* 1999, **312**: 4073

4. Funk, J.; Schmitt, U.; Kiefer, W. and A. Materny, *J. Raman Spec.*, 2000, **31**: 743.

5. Siebert, T.; Maksimenka, R.; Materny, A.; Engel, V.; Kiefer, W. and M. Schmitt, *J. Raman Spec.*, 2002, **33**: 844-854.

6. Underwood, D. F. and D. A. Blank, *J. Phys. Chem. A.*, 2005, **109**(15): 3295-3306.

7. Joo, T. H.; Jia, Y. W.; Yu, J. Y.; Lang, M. J. and G. R. Fleming, *J. Chem. Phys.*, 1996, **104**(16): 6089-6108.

8. Horng, M. L.; Gardecki, J. A.; Papazyan, A. and M. Maroncelli, *J. Phys. Chem.*, 1995, **99**(48): 17311-17337.

9. Kovalenko, S. A.; Ruthmann, J. and N. P. Ernsting, *Chem. Phys. Lett.*, 1997, **271**(1-3): 40-50.

10. Park, S.; Flanders, B. N.; Shang, X. M.; Westervelt, R. A.; Kim, J. and N. F. Scherer, *J. Chem. Phys.***,** 2003, **118**(9): 3917-3920

11. Cave, R. J. and E. W. Castner, *J. Phys. Chem. A*, 2002, **106**(50): 12117-12123.

12. Kovalenko, S. A.; Ruthmann, J. and N. P. Ernsting, *J. Chem. Phys.***,** 1998, **109**(5): 1894-1900.

13. Frediani, L.; Ågren, H.; Ferrighi, L. and K. Ruud, *J. Chem. Phys.,* 2005, **123**, 144117.

14. Sun, W.F.; McKerns, M. M.; Lawson, C. M.; Gray, G. M.; Zhan C. L. and D. Y. Wang, *Proceedings of the Society of Photo-optical Instrumentation Engineers (SPIE)*, 2000, **4106**, 280-288.

15. Luo, Y.; Norman, P.; Macak, P. and H. Ågren, *J. Chem. Phys.*, 1999, **111**, 9853.

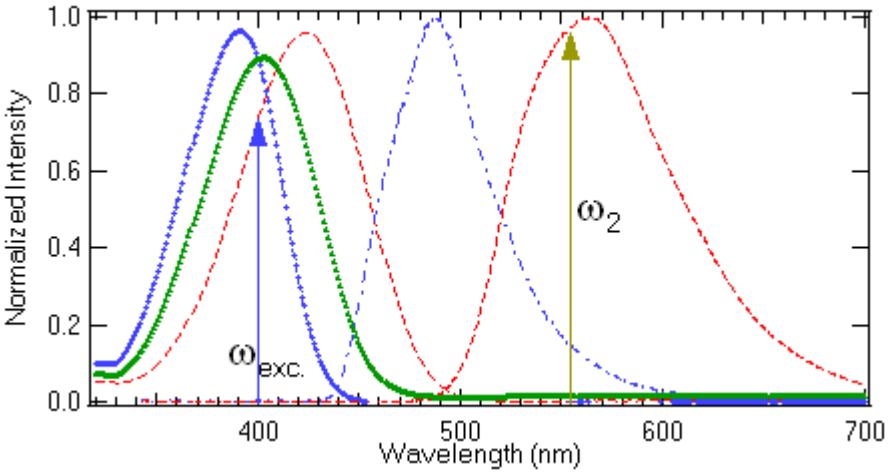

Figure 5.1: Absorption (shorter wavelengths) and emission (longer wavelengths) spectra for C153 (red dashed line), C35 (green dotted line) and C102 (blue dot-dash line). The location of the excitation pulse (400 nm, ω_{exc}) and the first field interaction for pump-fs/ps CARS (555 nm, ω_2) are marked with solid lines and arrows.

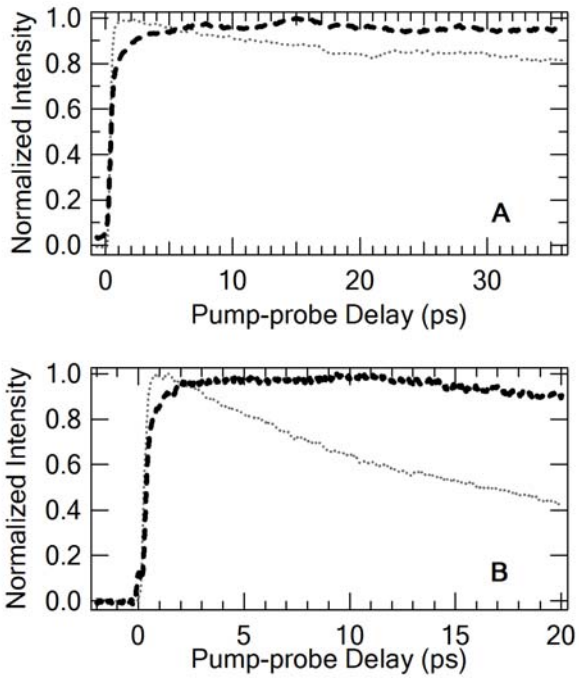

Figure 5.2: Transient gain results for pump (400 nm) and probe (ω_1 = 505 nm, gray, dotted and ω_2 = 555 nm, black, dashed) for C153/PC (A) and C153/MeOH (B). Both wavelengths selected are approximately 10nm slices of the fluorescence band. Pulse limited rise times are observed for all sets of data followed by dynamics specific to the solute/solvent combination studied.

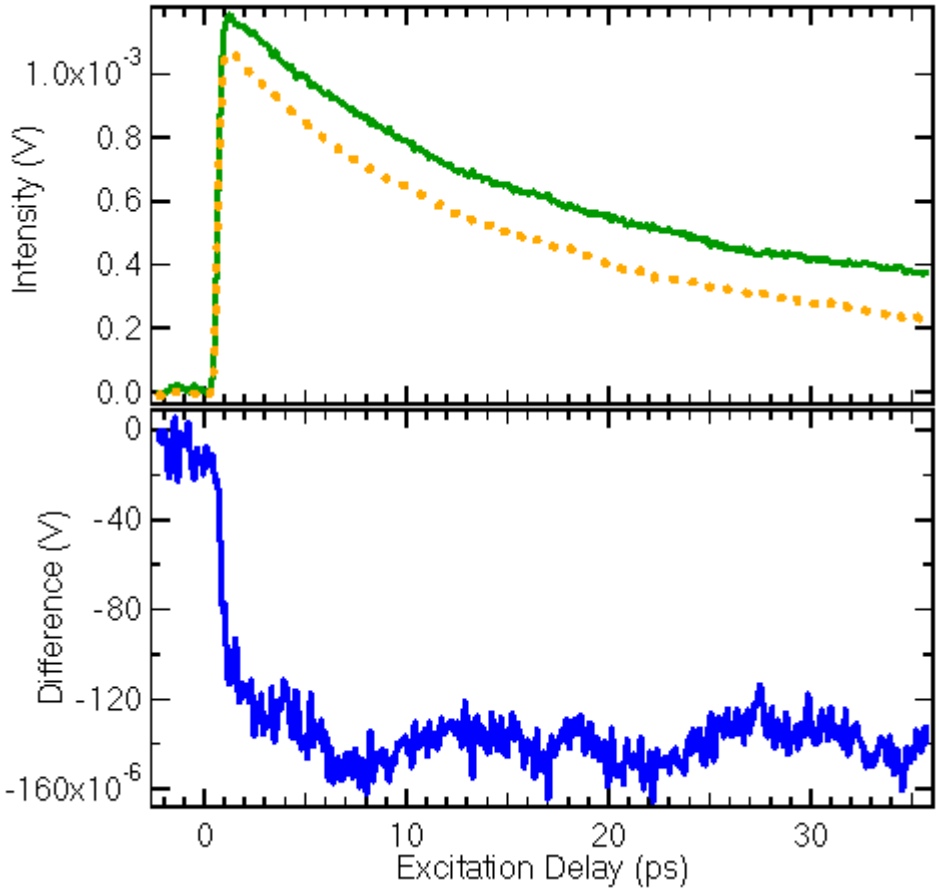

Figure 5.3: Pump-dump-probe results for C153/MeOH. A) Raw transient gain traces without the dump pulse present (green) and with the dump pulse present (orange) The pump is the ω_{exc} pulse while the dump and probe pulses are ω_2 and ω_1 respectively. The x-axis is defined as the time between the excitation pulse and the ω_1 and ω_2 overlapped pulses B) The difference signal is generated as the difference in ω_1 with and without the time-overlapped ω_2 pulse present. The effect of the dump pulse appears to be a constant decrease in population with no evident increase in ω_1 reabsorption as a function of time.

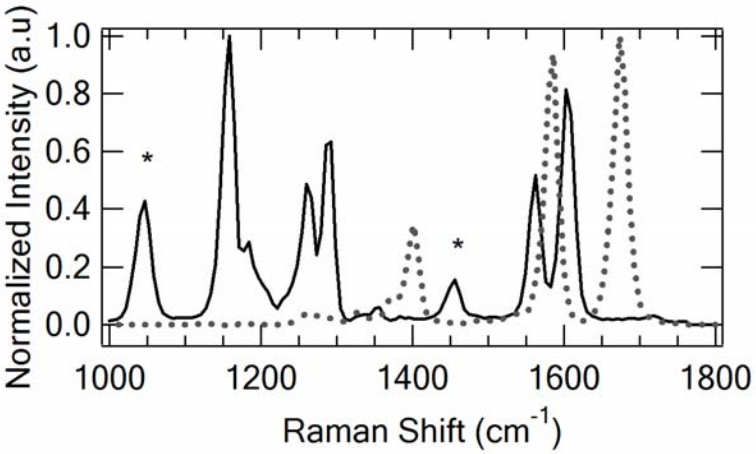

Figure 5.4: Example spectra generated using fs/ps CARS and pump-fs/ps CARS for C153/MeOH. Ground state spectra (solid, black) generated without the pump (ω_{exc}) pulse. Solvent modes are indicated with an asterisk. Excited state frequencies (dotted, gray) are generated with the presence of the excitation pulse and displayed after subtraction of the ground state spectrum. The excited state spectra displayed in this figure was taken at pump-CARS delay of 20 ps. The signal has been normalized to the max band in each individual spectrum (for relative scaling see Chapter 4)

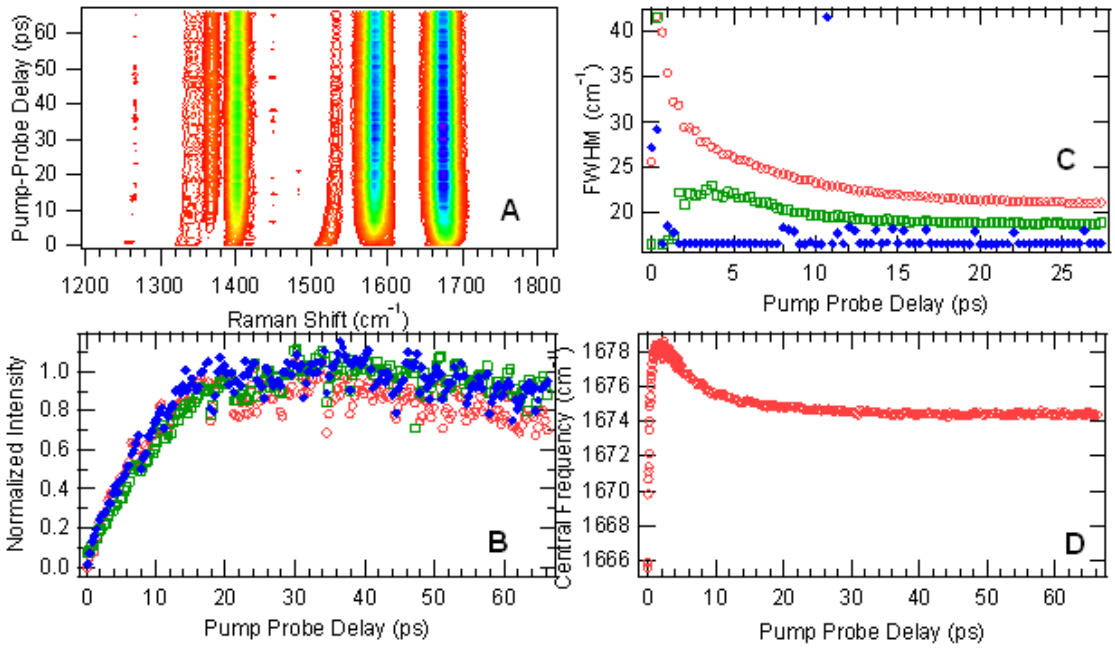

Figure 5.5: Pump-fs/ps CARS results for C153/MeOH. A) Contour plot shows the acquired signal as a function of pump delay. Strong modes are observed at 1674, 1584, and 1400 cm^{-1}. B) The evolution of the intensity of these modes is normalized (1674 peak, red circles; 1584 peak, green squares; 1400 peak, blue diamonds) . All three modes display very similar timescales of growth, which for the C153/MeOH appears non-exponential (roughly fit to 9 ps) but reaching a max in roughly 20-25 ps. C) FWHM Evolution of the same modes, the broadness of the 1674 is believed to be due to the existence of both non-hydrogen bonded and hydrogen bonded populations at early times. Further insight into hydrogen bonding in excited state Coumarins can be found in the chapter 4 D) Frequency evolution of the 1674 mode when fit at low resolution with Gaussian lineshapes.

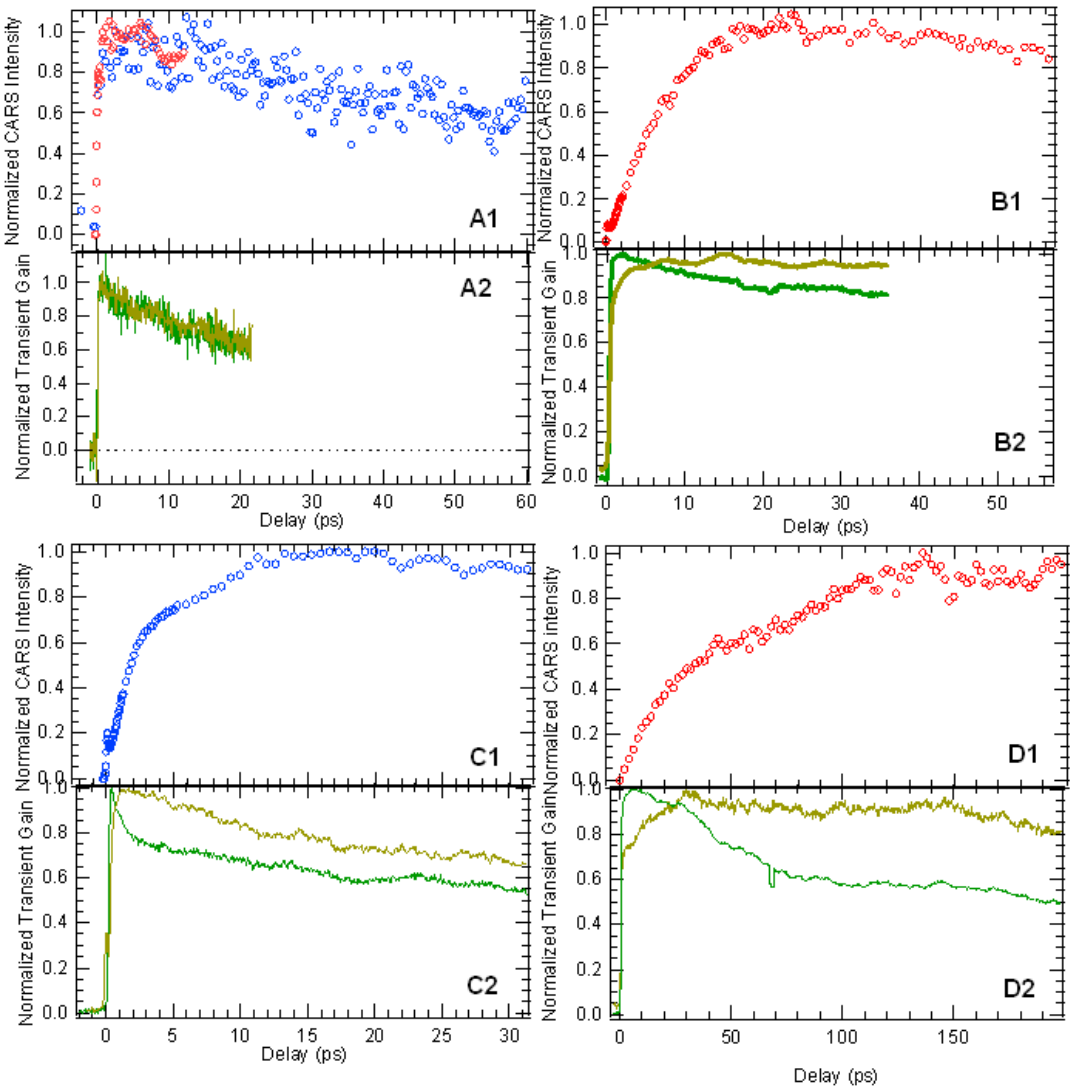

Figure 5.6: Pump-fs/ps CARS intensity results for the 1671/1684 peak (x1) and transient gain spectra (x2) for ω_1 (green lines) and ω_2 (yellow lines) for C153 in various solvents: a) cyclohexane b) propylene carbonate c) acetonitrile and d) 1-butanol. Note the different x axis ranges for each solvent. With the exception of the cyclohexane data, the CARS intensity shows a considerably slower rise time that appears to have some correlation to solvent viscosity (and known long-time solvent response timescales, see discussion)

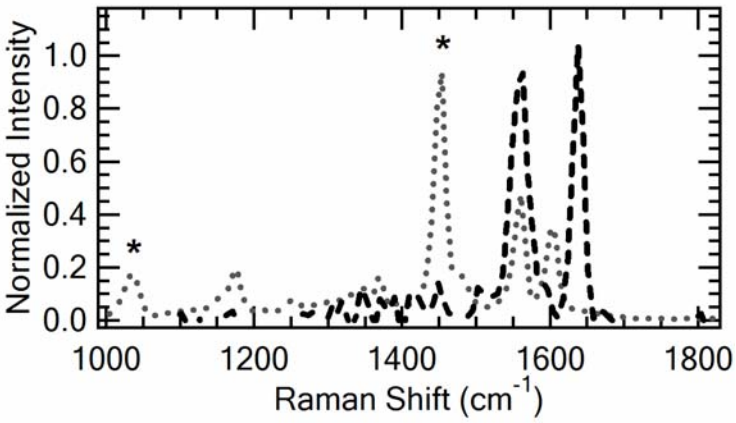

Figure 5.7: Ground (gray, dotted) and excited (pump delay 20 ps, black, dashed) fs/ps CARS spectra of C102 in MeOH. Similar modes to C153 are observed in the ground state (methanol modes denoted by asterisk) while the excited state shows two prominent modes. The two modes are located at approximately 1638 and 1559 cm^{-1} respectively (compare Figure 5.4).

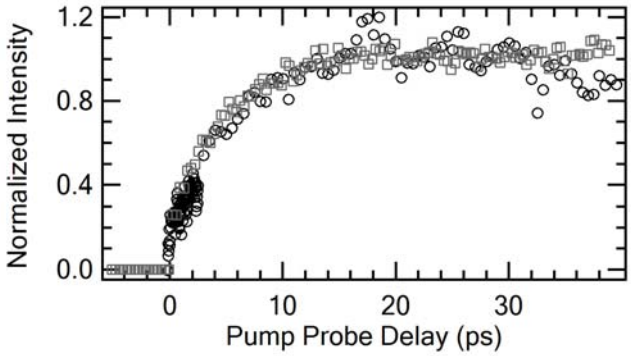

Figure 5.8: Intensity growth of the 1638/1651 mode of C102 in MeOH/PC. C102/MeOH (black circles) and C102/PC (gray squares) rise with very similar timescales which fit well to single exponentials of approximately 4.4 ps. In C153, the rise times in methanol and PC are also comparable with rise times near 9 ps (see fig 5.6 (B1) and fig 5.5 (B)).

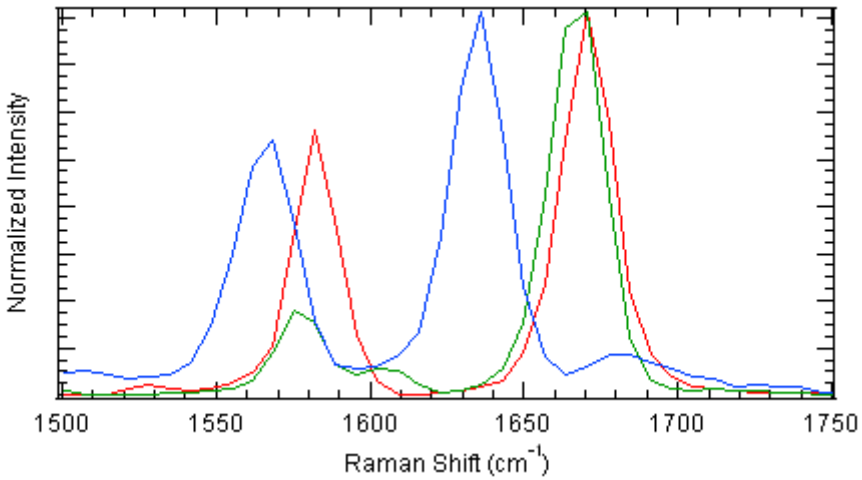

Figure 5.9: Pump-fs/ps CARS results for C153/MeOH (red), C35/MeOH (green), and C102/MeOH (blue) taken 25 ps after electronic excitation. C35 and C153 have very similar frequencies while C102 is generally red shifted in frequency for the same modes in the excited state. The intensities have been normalized to the peak in the 1600-1700 region.

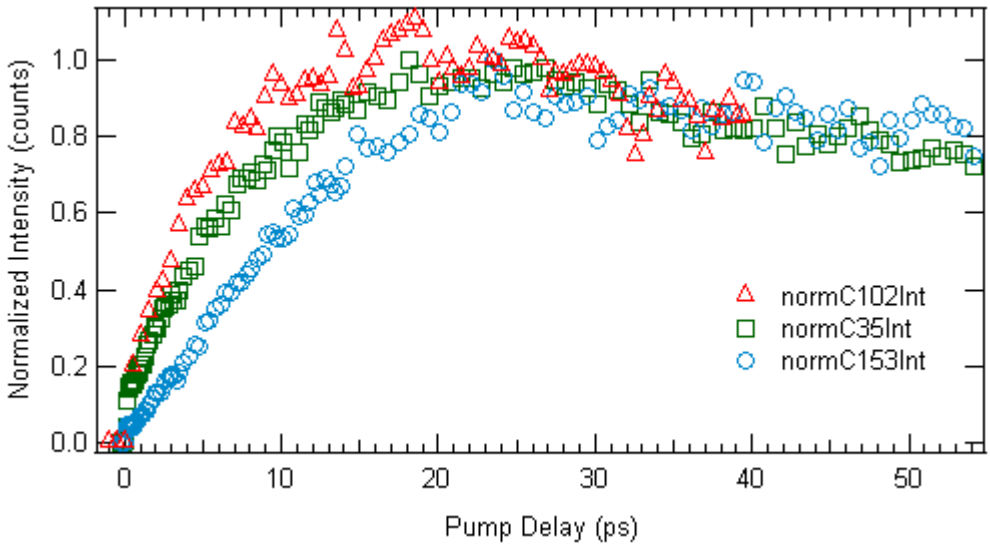

Figure 5.10: Intensity growth of the 1671 (C153/C35)/1636 (C102) peaks in methanol. Red triangles denote C102 , green squares C35, and blue circles C153. Clear differences can be seen from the C153 to C35 rise times whereas smaller differences can be seen in the rise time of C35 and C102.

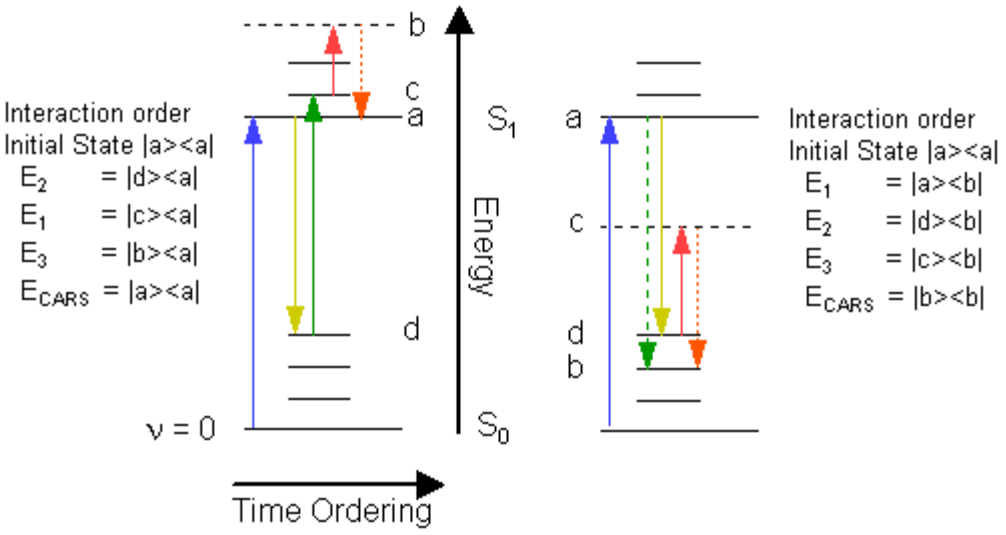

Figure 5.11: Two potential four-wave mixing diagrams for obtaining CARS signal under the resonance conditions of the coumarin dyes from the first excited state (signal originating from the ground state is ignored). On the left side, ω_{exc} acts to transfer some population to the excited state S_1, where some time later, the time overlapped ω_2 and ω_1 then act in a downward and subsequent upward fashion (both ket evolution) where ω_3 (ket evolution) scatters off generating ω_{CARS} containing excited state vibrational information. The right hand side is the required scheme for observing vibrationally hot ground state vibrational modes and still fulfilling the requirement of CARS signal in the direction $k_{CARS} = k_1 - k_2 + k_3$. ω_1 acts in a downward fashion (bra evolution) to some ground state vibrational mode, while ω_2 acts also in a downward fashion (ket evolution) to another vibrational mode where ω_3 (ket) then scatters to generate ω_{CARS}.

CHAPTER 6: ULTRAFAST EXCITED STATE INVESTIGATION OF N,N-DIMETHYL-*p*-NITROANILINE USING FS/PS CARS

Benjamin D. Prince, Ji Hyun Jun, and Hans U. Stauffer

A paper to be submitted to the *Journal of Physical Chemistry A*

6.1 Abstract

The excited state dynamics of N,N-dimethyl-para-nitroaniline (DMPNA) are probed using fs/ps CARS for the first singlet excited state. The resulting spectrum shows only small changes in geometry, as evidenced by the vibrational frequencies, in polar solvents but a more significant change in slightly polar toluene. The intensity decay profiles appear to be solvent viscosity and polarity independent with a lifetime of ~500 fs . The role of the nitro group as a probe of solvent environment is discussed in the ground state via experiment and DFT calculations employing the Polarizable Continuum Model (PCM).

6.2 Introduction

N,N-dimethyl-para-nitroaniline (DMPNA, fig 5.) is a member of a subset commonly referred to as "push-pull" molecules. The opposite position of electron donor (in the case of DMPNA, $N(CH_3)_2$) and electron acceptor (NO_2) create a conjugated π system that has provided a wealth of experimental and theoretical work to discuss the large (hyper)polarizabilities, solvent effects, relaxation pathways and substitution effects of donor and acceptor groups on properties of these molecules (see ref. [1-15] for DMPNA, see ref. [16-32] for a subset of para-nitroanilines more generally) . The goal of this research is to

exploit these properties for use of non-linear optical devices with the hopes of replacing inorganic crystals and other related media [33].

A common model used to describe the "push-pull" behavior of conjugated polyenes, and extended to aromatic systems, is to employ two basis states, with one extreme being a "neutral" basis and the other a "zwitterionic" basis[34-42]. This is extended also to the first charge transfer excited state with the neutral heavily representing the ground electronic state and the zwitterionic representing the charge transfer excited electronic state. An example for the case of DMPNA is shown in Figure 6.5. The relative weightings of the two basis sets make up a linear combination that is used to rationalize the structure of the molecule in a given environment. It is expected that as the solvent becomes more polar the contribution of the zwitterionic basis in the ground state would increase and represent more closely the electronically excited state.

Previous experimental work for DMPNA has assigned excited state lifetimes to the optically active electronically excited state in polar solution via the pump-supercontinnum probe technique (PSCP) which after analysis using the band integral method yielded three timescales: a fast $-NO_2$ twisting component (~50 fs), internal conversion (~700 fs) and then ground state cooling[10]. Resonance and spontaneous Raman has been used to probe the symmetric NO_2 stretch Raman shift as a function of solvent polarity where it was shown that, in the case of Resonance Raman, the detected NO_2 stretch frequency was directly related to which color was used to probe[4]. Terazima and co-workers followed this up with a comparison of spontaneous Raman NO_2 frequencies and absorption spectra as a function of solvent polarity for a large number of solvents, ionic liquids and supercritical fluids and found a direct correlation between the obtained frequency and the polarity of the

environment irrespective of solvents hydrogen bond donating ability[9]. Hyper-Rayleigh scattering was used to determine that in DMPNA no site specific interactions (hydrogen bonding) occurred in a large group of solvents and solvent mixtures[6].

These experiments generally found some agreement and some differences between DMPNA and its simpler relative PNA. Both spontaneous Raman and Resonance Raman with sufficient resolution found two symmetric NO_2 stretches in PNA with a solvent dependent intensity in all solvents except cyclohexane and other non-polar solvents but found little frequency dependence on solvent[4, 26]. These two peaks have been discussed in terms of mode coupling between the pair of C-N bonds[43] or unique solvent environments[29]. The PSCP experiments for PNA found generally that the excited state decayed twice as fast as that in DMPNA and was suggested to be a result of the different number of hydrogen bonds the two species could form. However, the qualitative dynamics remained much the same with regard to twisting, internal conversion and cooling. In the case of PNA in water, a coherent oscillation assigned to the $-NO_2$ torsional mode was detected at 61 cm^{-1} in the band integral analysis. Ernsting and coworkers had previously calculated using the semiempirical SAM1 Hamiltonian the ground and first excited state of PNA and found in water an important $-NO_2$ twist angle of 60^o in the excited state that allowed internal conversion via conical intersection between the charge transfer state and the ground electronic state[18]. Tretiak, Kelley, and Moran also extended their Resonance Raman results into theoretical modeling that suggested $-NO_2$ twisting in the excited state was predicted in acetonitrile but not in cyclohexane or dichloromethane[27].

How much this twisting speaks of a TICT state is unclear, as in the case of DMPNA, previous work had expressed some doubt about the likelihood of TICT formation[3]. If

twisting is occurring in the electronic excited state, it might be expected to show some sort of solvent dependence in terms of timescales due to viscosity or solvent stabilization (lowering) of a TICT energy barrier akin to discussion found elsewhere (get the "right" references)

The purpose of this work is to investigate the changes in the excited state by direct observation of Raman active vibrational bands in the first excited singlet state. These changes will be discussed relative to previous experimental work referenced above and comparison to trends observed in the ground state as it relates to the polarity of the solvent environment.

6.3 Experimental Methods

6.3.1 Calculations

Calculations were performed using GAMESS[44] and visualized using MacMolPlt[45]. Calculations at the B3LYP/6-31++G(2d,p) level were performed on DMPNA in both the gas phase and solvated environments utilizing the Polarizable Continuum Model (PCM) built into GAMESS. PCM solvents included cyclohexane, toluene, acetone, methanol, acetonitrile, and water with all of the relevant solvent parameters being used as default in GAMESS with the exception of acetonitrile where the dielectric constant was used as 35.94 taken from ref. [46]. Hessian calculations were performed on all optimized geometries to obtain vibrational frequencies for comparison to experiment and to verify a stationary state was located. The calculated frequencies are reported unscaled.

6.3.2 Experimental

The laser system was used as described in detail in reference[47]. Briefly, the fundamental output (800 nm) of an amplifier was split into several beams. One portion was used to generate mid-IR beams via optical parametric amplification and subsequently mixed

with another portion of 800 nm to generate visible light, ω_1 centered at 511 nm ($\Delta\omega$ ~ 250 cm^{-1}) and ω_2 centered at 544 nm ($\Delta\omega$ ~ 300 cm^{-1}). This setup probes Raman active modes centered from ~950 cm^{-1} to ~1500 cm^{-1}. A third portion, ω_3, of the fundamental was used in a pulse shaper described in reference 47, and in these experiments had bandwidth of ~7.5 cm^{-1} although for some solvents, notably ethylene glycol and toluene, the bandwidth was approximately 13 cm^{-1}. A final portion of the fundamental was used to generate the excitation pulse and was doubled (ω_{exc} = 400 nm) and placed along a variable computer controlled delay line. Typical powers used were 0.1 μJ for ω_1, 0.5 μJ for ω_2, 2 μJ for ω_3, and 3 μJ for ω_{exc}.

The four beams were aligned into a rotating sample cell of ~220 μm sample thickness (2 mm windows) and focused by means of a large focusing mirror to a beam size of ~ 160 μm (ω_{exc} ~ 200 μm). The spatially overlapped beams relative timings were selected to minimize the non-resonant signal contribution to the output four wave mixing signal. Notably, ω_1 and ω_2 are time overlapped and the max intensity of ω_3 is delayed using the procedure outlined in previous work. The OKE cross-correlation between ω_{exc} and ω_1, ω_{exc} and ω_2 and convolution fits to the output data give an instrument response time for the pump-fs/ps CARS setup of ~125 fs.

The outputted four-wave mixing signal is directed into a spectrometer where it is dispersed by means of a grating before being collected by a 1340x100 element CCD (Princeton Instruments) operating in vertical binning mode. The detected signal is then returned to the computer and averaged. Data from the ground state spectra are taken without the presence of the ω_{exc} pulse while the excited state data are taken at various time delays of the ω_{exc} pulse.

DMPNA samples (Acros Organics, 99%) were used without further purification as obtained. Samples were generally dissolved to ~five mM concentration in commercially available solvents including methanol (Fisher, HPLC grade), propylene carbonate (99%, Alfa Aesar), toluene (Fisher, ACS Certified), acetonitrile (Fisher, HPLC grade), ethylene glycol (Fisher, ACS Certified) and BMIM-BF_4 (info).

Additional pump-probe experiments were performed using ω_1 and ω_2 as separate probe beams as a function of ω_{exc} delay to detect the stimulated emission resulting from the excited electronic state and the subsequent ground state recovery. The directly detected probe beam was aligned into a photodiode (Thorlabs, DET-210) connected to a lock-in amplifier (Stanford Research Systems, SR810) running at half the laser output frequency by means of a mechanical chopper (Thorlabs) placed in the pump (ω_{exc}) beam. The output of the lock-in amplifier was returned to a computer where the data was averaged until sufficient signal to noise was reached.

6.4 Results

6.4.1 Calculations

The numbering scheme employed in the discussion of the calculations is shown in figure 6.4. Results of the calculations at the B3LYP level in gas phase and the various PCM solvents are presented in Table 6.2. The ground state calculations show a strong dielectric dependence of the solvent on the various bond lengths, solute dipole, and obtained NO_2 symmetric stretch frequency. As solvent polarity increases, the bond between the amino-N and carbon (C5) shortens by 0.014 Å from gas phase to water while the benzene ring carbon-carbon bond lengths follow the pattern of lengthen, shorten, lengthen as solvent polarity

increases (note experimental benzene has bond lengths of 1.397 Å respectively). The C-C bond in ethane has an experimental bond length of 1.536 Å while C=C bonds in ethylene have lengths of 1.339 Å. Finally, the C-NO_2 bond length is found to shorten while the N-O bonds each lengthen. The calculated results do suggest as the solvent polarity increases, the bond alternation character of the molecule also increases but not to the point of reaching a rigidly single/double bond alternation.

The increased dipole character of the solute when surrounded by a dielectric continuum shows the very significant importance of the solvent dipolar characteristics on the relative weightings of the neutral and zwitterionic basis states of the two state model for molecules of this type. On going from gas phase to water, the dipole increases ~55% of its gas phase value. A similar solvent dependence is observed for the shift of the NO_2 symmetric stretch calculated at 1342 cm^{-1} in the gas phase to 1302 cm^{-1} in water.

Table 6.3 presents various Raman active modes (determined from the Raman calculations in the gas phase) in the region of interest for the CARS experiments. The same selection of solvents are shown and the resultant vibrations are shown unscaled and in cm^{-1}. Apart from the apparent differences between gas phase and any PCM solvent, the only mode with greater than 6 cm^{-1} difference is the symmetric -NO_2 stretch which shows a large shift.

6.4.2 Experimental

Ground and excited state fs/ps CARS spectra were obtained for DMPNA in a variety of solvents. Excited state spectra were recorded at 120 fs before the initial CARS beams and the resulting CARS spectra for the region of 1000-1600 cm^{-1} for DMPNA in acetonitrile are

displayed in figure 6.1 and zoomed into the 1300 region for select solvents in figure 6.5. The ground state, in the case of DMPNA in acetonitrile, obtained in this experiment is dominated by a very strong band at ~1315 cm^{-1} assigned to the NO_2 symmetric stretch via calculations and previous work and additional ground state modes observed at 1115 (phenyl-N (nitro) stretching) and 1205 cm^{-1} (ring stretching). The excited state spectrum taken at 120 fs is still dominated by a strong NO_2 contribution at 1311 cm^{-1} but has significant intensity in modes at 1112, 1450, and 1507 cm^{-1}.

The results from the solvents used in these experiments are displayed in Table 6.1. The table displays the observed NO_2 frequency in both the ground and excited state, solvent polarity, and change in NO_2 frequency between S_0 and S_1. Comparison of other observed modes does not show a marked solvent dependence although excited state signal for only the NO_2 stretch could be obtained for DMPNA in toluene.

Figure 6.2 displays the intensity dynamics from both types of experiments utilized. The pump-probe integrated trace is shown for ω = 507-518 nm in DMPNA in propylene carbonate. The pump probe signal is shown as the ratio of light out to light in and thus, a positive signal denotes stimulated emission while a negative signal denotes a transient absorption. The signal is initially dominated (top left graph) by a strong stimulated emission band which falls away with a ~500 fs time constant to be replaced with transient absorption signal that decays towards no change with a timescale of ~5 ps. The CARS spectra (figure 2, bottom left) intensity are a result of applying a two Gaussian fit to the data near 1300 cm^{-1}. The ground state frequency and full-width at half max (fwhm) are first obtained from the fitting of the ground NO_2 symmetric stretch and are held fixed when fitting the excited state data. The intensity is allowed to vary to account for changes in population as the electronic

state changes. The excited Gaussian component is unconstrained and the bottom graphs in figure 6.2 are generated by summing the intensity from the ground state and excited state component and subtracting from it the ground state intensity obtained without the excitation beam present. A significant difference from comparing the pump-probe trace to the CARS signal trace at long times is the sudden increase of signal above what is expected from the ground state alone around excitation delay of 5 ps.

Figure 6.3 shows the CARS spectra of DMPNA/PC obtained after subtraction of the ground state at three excitation delays. The signal at 0.07 ps is dominated by the strong excited NO_2 component at 1304 cm^{-1}. At 2.3 ps, DMPNA has internally converted and subtraction of the ground state results in a lineshape that can be reasoned as a mixture of bleach of ground state population (as the vibrationally hot ground electronic state relaxes) and the beginning of the rise of the signal observed at 5 ps. At 5 ps, the CARS spectrum obtained represents more of the excited state signal with a frequency center near 1304 cm^{-1} than the ground state at 1310 cm^{-1}. This identical behavior is seen in all polar solvents used (toluene S/N not sufficient to determine).

The CARS intensities of the 1510 cm^{-1} peak are displayed in figure 6.7 for several of the solvents used. CARS intensity is the related to square of the concentration of molecules in a given state. The decay timescales of the CARS signal generally fit well to approximately 250 fs +/- 50 fs.

6.5 Discussion

The ground state NO_2 frequency dependence has been experimentally observed in previous work and will not be elaborated further here except to note the similarity between

NO_2 frequency observed in the identical solvents[9]. A simple scheme which might be used to understand this frequency dependence is the use of the two resonance structures; neutral and zwitterionic, which are taken as the basis states whose weightings determine the NO_2 frequency determined. The "neutral", more gas-phase like, would be expected to dominate the ground state in the most non-polar solvents while the introduction of a strongly dipolar solvent would serve to stabilize the zwitterionic structure and allow a larger contribution in the non-CT ground electronic state. A fully zwitterionic form should be realized in the NO_2 region as a lengthening of the N-O bond distance and thus a decrease in the force constant and consequently the vibrational frequency. Additionally, one should see an increase in the quinoidal like structure, shorter bonds at the N-C's and alternating shorter/longer/shorter bonds on the benzene ring. As solvent polarity increases, the observed NO_2 frequency decreases both in experiment and calculation and would seem to be in line with an increasingly zwitterionic form of the ground state. Even with the dynamic behavior of the solvent on the NO_2 stretch, examination of Table 6.3 suggests that only small changes seem to be occurring via the vibrational spectra in this range.

Moran and Kelley note that as solvent polarity is increased, the ground and first excited states geometry should become more identical under this two basis set scheme and note, with the exception of methanol, the vibrational reorganization energy of the excited state decreases as solvent polarity increases[26]. Similarly, Kimura and coworkers noted a dependence of the FWHM of the absorption band of DMPNA in various solvents and assigned the decreasing bandwidth to a decrease in intramolecular reorganization energy as the solvent polarity increased. This led to the conclusion that with increasing solvent polarity, the displacement of the intramolecular vibrational coordinate in the ground state compared to

the excited state becomes smaller[9]. The third column of Table 6.1 reports the excited state frequency observed upon electronic excitation at a delay of 120 fs. DMPNA in toluene, the least polar solvent where acceptable signal to noise could be acquired, shows a significant shift of the NO_2 frequency from that observed in the ground state while the more polar solvents result in, generally, decreasing changes as the solvent polarity parameter is increased. In the case of the ionic liquid BMIM-BF_4 and polar propylene carbonate, the ground state frequency is extremely close to that of the excited state suggesting the similarity between the ground electronic state in polar environments and the first excited state in the same environment while those less polar environments appear more neutral in the ground state but reach the same excited state configuration as those in polar solvents..

The excited state intensity dynamics, shown in the bottom of Figure 6.2 and Figure 6.7, of the observed modes show little to no solvent dependence. All DMPNA/solvent systems studied resulted in real decay profiles nearly identical with time constants near 500 fs with variation of about ± 50 fs. The change in solvent viscosity over orders of magnitude from methanol to BMIM-BF_4 seems to generate no significant change in the excited state lifetime. The quickly decaying excited state can be discussed in terms of solvation response and the likelihood of a twisted NO_2 state existing.

In terms of solvation response, the rapidly decaying electronically excited state, with the exception of acetonitrile, disappears considerably faster than the average solvation response. Maroncelli and co-workers extensive study of solvation dynamics suggest that the only solvent with a comparable solvation timescale to the excited state lifetime is acetonitrile[48], while the others present average timescales on the order or greater than the timescale of the excited state lifetime. This slower response would suggest a dynamical

solvent environment generally having a smaller effect on the excited state geometry than a molecule with an excited state lasting on the order of picoseconds. This may explain the uniformity of both the frequency and decay timescales observed through the range of solvents studied.

. This would lend itself to the suggestion that a twisting or paddling motion of a twisting NO_2 group would seemingly be unlikely as other work has shown that solvent viscosity tends to result in differing excited state timescales, whether they be witnessed through pump-probe traces, dual fluorescence timescales or direct vibrational probing[49]. Additional evidence for the lack of twisting in the NO_2 moiety upon excitation comes from the increasingly narrowing difference between excited and ground state as solvent polarity is increased. An obvious assumption is that increasing the solvent polarity of the ground state only serves to lengthen the N-O bonds of the NO_2 group and does not twist the entire group relative to the phenyl ring. Our work on 4-dimethylamino-4'-nitrostilbene (DANS) suggests that a twisted NO_2 structure can be observed with a strong downshifting (>20 cm^{-1}) of the NO_2 frequency as compared to the ground state frequency. Finally, the similarity of the NO_2 symmetric stretch in toluene and solvents like propylene carbonate in the excited state would either lead to the conclusion that either the state is twisted in the ground state for polar solvents, which generates the red-shift in observed NO_2 frequency, and becomes twisted for all solvents in the excited state or the shift is solely due to the change in electronic configuration (namely, charge transfer) to a more zwitterionic structure. Of course, there is a third possibility that twisting of the NO_2 group is not observable via the $-NO_2$ symmetric stretch. Given the PCM calculations and their experimental counterpart, it is likely that the

ground state $-NO_2$ symmetric stretch can be assigned to changes in relative bond lengths via solvent stabilization

The two-level model of linear combinations of neutral and zwitterionic basis states thus seems a reasonable scheme for the treatment of ground and excited states in DMPNA if we consider, at least for solvents of toluene polarity and higher, that the excited state is made up of a "zwitterionic" state while the ground electronic state can be considered a sliding scale between the more "neutral" (in the case of toluene and cyclohexane) and the more "zwitterionic" (in the case of the more polar solvents). To further compare the "zwitterionic" component in the ground and excited state, an interesting behavior seems to occur after internal conversion in DMPNA in polar solvents. After internal conversion ($t_{400} > 1$ ps), the pump-probe trace shows a decaying transient absorption. Both PNA and DMPNA have seen studies using time-resolved resonance Raman as a probe of vibrational cooling by direct monitoring of the resonance Raman vibrational spectra after excitation[20, 24, 25, 28]. These studies have led to considerable understanding of timescales of energy loss and population transfer for PNA in various polar solvents. The time period after internal conversion has been assigned as funneling down of energy and population in the vibrationally hot ground electronic state.

In the bottom right graph of Figure 6.2, the signal above the dashed line is an increase over the signal level observed for the ground state only. Given the pump-probe trace behavior (top right graph), the CARS intensity signal should have similar dynamics which should be mainly dominated by a recovery of ground state intensity. The apparent increase is particularly interesting especially when taken in context of the observed frequency at the second maximum. The top trace of figure 3 shows the Raman signal obtained at $t_{400} = 5$ ps

which appears to be nearly identical to that observed for the excited state at 0.07 ps. It is unclear how to precisely define which electronic state this signal originates from since it is possible that it is a non-resonant (or resonant) CARS spectrum of the hot ground state or it could contain excited state information via reabsorbing to the excited state via the ω_1 CARS beam. Considering the low input power of ω_1 (~1/30th of the ω_{exc}), the concentration squared dependence on CARS signal, and the long period of time the excess signal (>5 ps) exists for, it is unlikely to be due to the excited electronic state and more likely due to a resonance ground state CARS spectra. Observations from time-resolved resonance Raman studies on PNA resulted in a growth of several modes with some differing timescales after internal conversion. Careful examination of the NO_2 stretch observed in these experiments nearly always results in a slightly downshifted frequency which ultimately ends at the ground state frequency. Therefore it is possible the CARS peak observed around 5 ps can be thought of as a $v_2 \leftarrow v_1$ transition and thus downshifted because of anharmonicity like the resonance Raman spectra or it may be indicative of the relaxing ground electronic state being significantly similar in geometry to the excited state initially due to the solvent first beginning reorganization about a stronger dipole in the electronically excited state and then reverting to the original ground state equilibrium condition. The fact that it can be seen in CARS, with concentration squared signal dependence, suggests that a large number of molecules are built up in a common state, for example a $v = 1 \leftarrow 0$ transition, which then utilizes the ω_1 absorption from the hot ground state to generate a resonantly enhanced ground state CARS spectrum. That this signal decays while the pump-probe trace changes little suggests that the molecules making up this signal are proceeding to another state or otherwise relaxing. It is complicated by the fact that the ground state spectra obtained (at equilibrium in

the ground state) are non-resonant CARS spectra, whereas the signal near 5 ps is resonantly enhanced by the ω_1 at 507-518 nm being absorptive for the relaxing ground electronic potential but not for the completely relaxed ground state. It is clear that by 30 ps the ground state has recovered completely except the apparent offset observed in the pump-probe trace.

6.6 Conclusions

The excited state dynamics of DMPNA in various solvents were probed using pump-probe and fs/ps-CARS. The pump-probe traces show a short-lived emissive band for ω_1 and ω_2 with time constants on the order of 500 fs while fs/ps CARS reveals an excited state geometry very similar to the ground state in all cases studied with the NO_2 frequency showing the most interesting solvent behavior when compared against the ground peak. The two basis state model of linear combinations of neutral and zwitterionic forms seems to adequately define the ground state as solvent polarity increases the more zwitterionic component. The excited state, with NO_2 frequency very similar to the most polar solvent/DMPNA system, would therefore be more zwitterionic in character even for slightly polar toluene.

Solvent choice has little effect on the resultant excited state NO_2 frequency as well as the observed intensity dynamics over a very large viscosity range which suggests that, coupled with the similar NO_2 vibrational frequencies, little or no twisting of the NO_2 group upon excitation and thus no formation of a TICT state. The fast internal conversion would most likely be related to the extremely close geometry of the excited state to that of the "hot" vibrational ground state where at times after internal conversion, a recurrence of excited state like NO_2 frequency could be observed. This recurrence of signal is most likely indicative of

the similarity before full relaxation of the NO_2 in the ground state and the NO_2 seen in the excited state rather than an overtone of the ground state NO_2 symmetric stretch.

6.7 References

1. Balakina, M.Y. and S.E. Nefediev, *International Journal of Quantum Chemistry.*, 2006. **106**(10): p. 2245-2253.

2. Davis, D.; Sreekumar, K.; Sajeev, Y. and S. Pal, *J. Phys. Chem. B*, 2005. **109**(29): p. 14093-14101.

3. Dobkowski, J.; Herbich, J.; Waluk, J.; Koput, J. and W. Kuhnle, *Journal of Luminescence*, 1989. **44**(3): p. 149-160.

4. Fujisawa, T., M. Terazima, and Y. Kimura, *J. Chem. Phys.*, 2006. **124**(18).

5. Helburn, R.; Bartoli, M.; Pohaku, K.; Maxka, J.; Compton, D.; Creedon, B. and C. Stimpson, *J. Phys. Org. Chem.*, 2007. **20**(5): p. 321-331.

6. Huyskens, F.L., P.L. Huyskens, and A.P. Persoons, *J. Chem. Phys.*, 1998. **108**(19): p. 8161-8171.

7. Jodicke, C.J. and H.P. Luthi, *J. A. C. S.*, 2003. **125**(1): p. 252-264.

8. Kimura, Y.; Fukuda, M; Kajimoto, O. and M. Terazima, *J. Chem. Phys.*, 2006. **125**(19).

9. Kimura, Y., T. Hamamoto, and M. Terazima, *J. Phys. Chem. A*, 2007. **111**(30): p. 7081-7089.

10. Kovalenko, S.A.; Schanz, R.; Hennig H. and N. P. Ernsting, *J. Chem. Phys.*, 2001. **115**(7): p. 3256-3273.

11. Mhin, B.J. and B.H. Park, *Chem. Phys. Lett.*, 2000. **325**(1-3): p. 61-68.

12. Penner, G.H.; Bernard, G. M.; Wasylishen, R. E.; Barrett, A. and Curtis, R. D., *J. Org. Chem.*, 2003. **68**(11): p. 4258-4264.

13. Penner, G.H. and A. McCullough, *J. Org. Chem.*, 2006. **71**(23): p. 8794-8799.

14. Ye, A.J. and J. Autschbach, *J. Chem. Phys.*, 2006. **125**(23).

15. Ye, A., S. Patchkovskii, and J. Autschbach, *J. Chem. Phys*, 2007. **127**(7).

16. Cammi, R.; Frediani, L.; Mennucci, B. and K. Ruud, *J. Chem. Phys.*, 2003. **119**(12): p. 5818-5827.

17. Champagne, B., *Chem. Phys. Lett.*, 1996. **261**(1-2): p. 57-65.

18. Farztdinov, V.M.; Schanz, R.; Kovalenko, S. A. and N. P. Ernsting, *J. Phys. Chem. A*, 2000. **104**(49): p. 11486-11496.

19. Faustino, W.M. and D.V. Petrov,. *Chem. Phys. Lett.*, 2002. **365**(1-2): p. 170-175.

20. Gunaratne, T., J.R. Challa, and M.C. Simpson,. *Chemphyschem*, 2005. **6**(6): p. 1157-1163.

21. Jonsson, D.; Norman, P.; Agren, H.; Luo, Y.; Syvester-Hvid, K. O. and K. V. Mikkelsen, *J. Chem. Phys*, 1998. **109**(15): p. 6351-6357.

22. Kaatz, P. and D.P. Shelton, *J. Chem. Phys.*, 1996. **105**(10): p. 3918-3929.

23. Kovalenko, S.A.; Schanz, R.; Farztdinov, V. M.; Hennig, H and N. P. Ernsting,. *Chem. Phys. Lett.*, 2000. **323**(3-4): p. 312-322.

24. Kozich, V.; Werncke, W.; Dreyer, J.; Brzezinka, K. W.; Rini, M.; Kummrow, A. and T. Elsaesser, *J. Chem. Phys.*, 2002. **117**(2): p. 719-726.

25. Kozich, V.; Werncke, W.; Vodchits, A. I. and J. Dreyer, *J. Chem. Phys.*, 2003. **118**(4): p. 1808-1814.

26. Moran, A.M. and A.M. Kelley, *J. Chem. Phys.*, 2001. **115**(2): p. 912-924.

27. Moran, A.M., A.M. Kelley, and S. Tretiak, *Chem. Phys. Lett.*, 2003. **367**(3-4): p. 293-307.

28. Schrader, T.; Sieg, A.; Koller, F.; Schreier, W.; An, Q.; Zinth, W. and P. Gilch, *Chem. Phys. Lett.*, 2004. **392**(4-6): p. 358-364.

29. Shigeto, S., H. Hiramatsu, and H. Hamaguchi, *J. Phys. Chem A*, 2006. **110**(10): p. 3738-3743.

30. Thomsen, C.L., J. Thogersen, and S.R. Keiding,.*J. Phys. Chem. A*, 1998. **102**(7): p. 1062-1067.

31. van Gisbergen, S.J.A., J.G. Snijders, and E.J. Baerends, *J. Chem. Phys.,* 1998. **109**(24): p. 10644-10656.

32. Wang, C.K.; Wang. Y. H.; Su. Y. and Y. Luo, *J. Chem. Phys.*, 2003. **119**(8): p. 4409-4412.

33. Burland, D.M.*, Chem. Rev.*, 1994. **94**(1): p. 1-2.

34. Thompson, W.H., M. Blanchard-Desce, and J.T. Hynes, *J. Phys. Chem. A.,* **102**(39): p. 7712-7722.

35. Thompson, W.H., M. Blanchard-Desce, and J.T. Hynes, *Abstracts of Papers of the American Chemical Society*, 1999. **218**: p. U521.

36. Thompson, W.H.; Blanchard-Desce, M.; Alain, V.; Muller, J.; Fort, A.; Barzoukas, M. and J. T. Hynes, *J. Phys. Chem. A*, 1999. **103**(19): p. 3766-3771.

37. Blanchard-Desce, M. and M. Barzoukas, *Journal of the Optical Society of America B-Optical Physics*, 1998. **15**(1): p. 302-307.

38. Lu, D.Q.; Chen, G. H.; Perry, J. W. and W. A. Goddard, *J. A. C. S.*, 1994. **116**(23): p. 10679-10685.

39. Chen, G.H., D.Q. Lu, and W.A. Goddard, *J. Chem. Phys.*, 1994. **101**(7): p. 5860-5864.

40. Perry, J.W.; Bourhill, G.; Marder, S. R.; Lu, D.; Chen, G. and W. A. Goddard, *Abstracts of Papers of the American Chemical Society*, 1994. **208**: p. 218.

41. Lu, D.Q., G.H. Chen, and W.A. Goddard, *J. Chem. Phys.*, 1994. **101**(6): p. 4920-4930.

42. Painelli, A. and F. Terenziani, *Chem. Phys. Lett.*, 1999. **312**(2-4): p. 211-220.

43. Kumar, K. and P.R. Carey, *J. Chem. Phys.*, 1975. **63**(9): p. 3697-3707.

44. Schmidt, M.W.; Baldridge, K. K.; Boatz, J. A.; Elbert, S. T.; Gordon, M. S.; Jensen, J. H.; Koseki, S.; Matsunaga, N.; Nguyen, K. A.; Su, S. J,; Windus, T. L.; Dupuis, M. and J. A. Montgomery , *J. Comp. Chem.*, 1993. **14**(11): p. 1347-1363.

45. Bode, B.M. and M.S. Gordon, *Journal of Molecular Graphics & Modelling*, 1998. **16**(3): p. 133.

46. Boes, E.S., P.R. Livotto, and H. Stassen, *Chem. Phys.*, 2006. **331**(1): p. 142-158.

47. Prince, B.D.; Charkaborty, A.; Prince, B. M. and H. U. Stauffer, *J. Chem. Phys.*, 2006, **125**(4): 044502.

48. Horng, M.L.; Gardeki, J. A.; Papazyan, A. and M. Maroncelli, *J. Phys. Chem.*, 1995, **99**(48): p. 17311-17337.

49. Grabowski, Z. R.; Rotkiewicz, K. and W. Rettig, *Chem. Rev.*, 2003, **103**(10), p. 3899-4031.

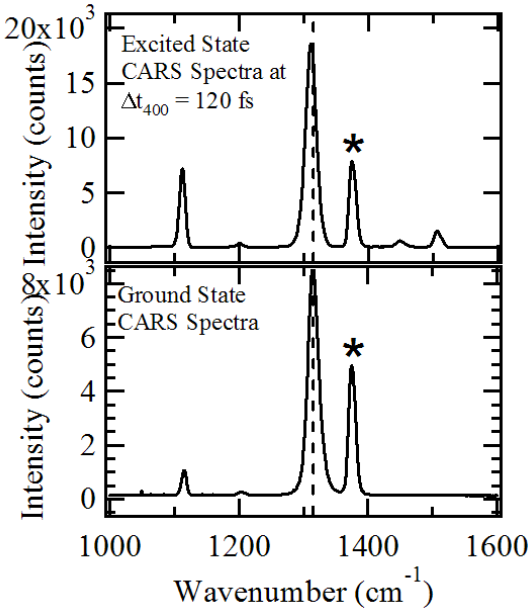

Figure 6.1: Ground and Excited fs/ps CARS spectra for DMPNA in acetonitrile. Bottom graph: CARS spectra obtained for non-resonant CARS with laser details specified in the experimental section. Dotted line shows the ground state position of the NO_2 symmetric stretch in this solvent. Top graph: CARS signal obtained 120 fs after electronic excitation with 400 nm. The NO_2 stretch (shown next to dotted line) is still the significant contributor to intensity but slightly shifted from the ground state frequency and nearly 2.5 times more intense under the resonance conditions described in the experimental section. A solvent peak has been denoted with an asterisk.

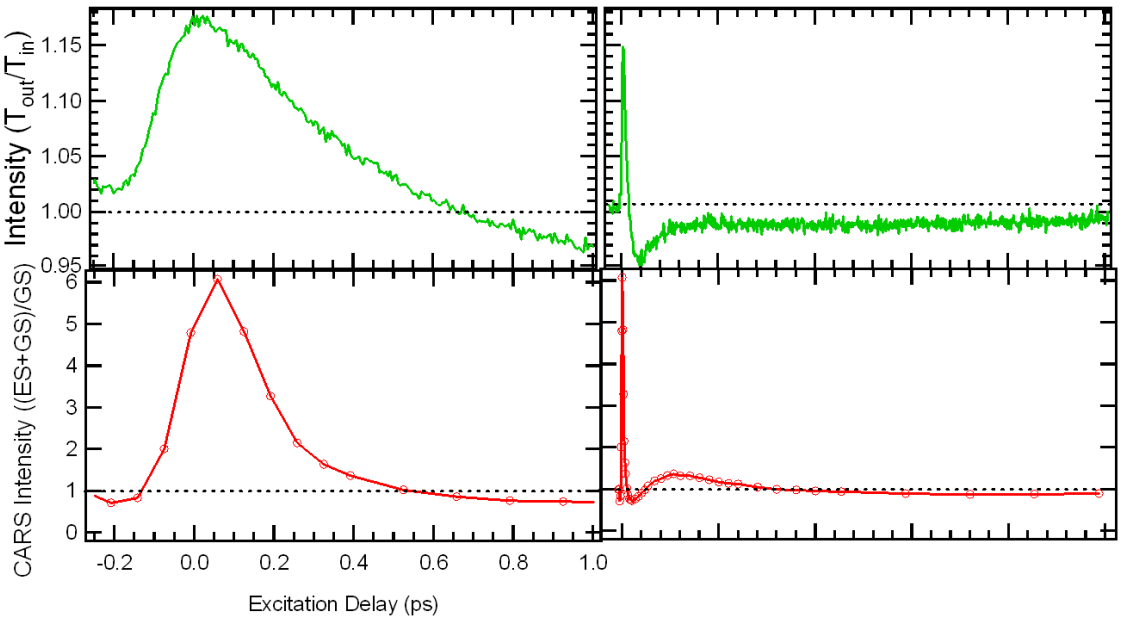

Figure 6.2: Top Graphs: Pump-probe trace at early times for ω = 507-518 nm for DMPNA in propylene carbonate. Signal greater than 1 is a stimulated emission band while signal lower than 1 is absorption from the vibrationally hot ground electronic state. Bottom Graphs: Sum of the State Intensity of the NO_2 symmetric stretch upon electronic excitation (see text for details). Dashes placed as visual aid to show changes from absorption to emission and excited signal to bleaching for pump-probe and CARS respectively.

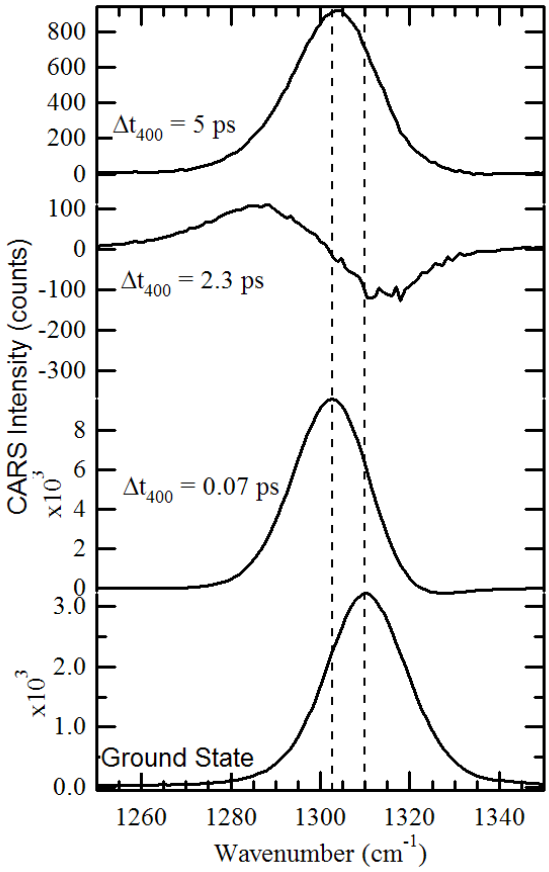

Figure 6.3: CARS spectra obtained at various excitation delays after subtraction of ground state signal. The bottom component shows an example ground state spectrum. The dashed lines denote the ground state central frequency and the excited state central frequency.

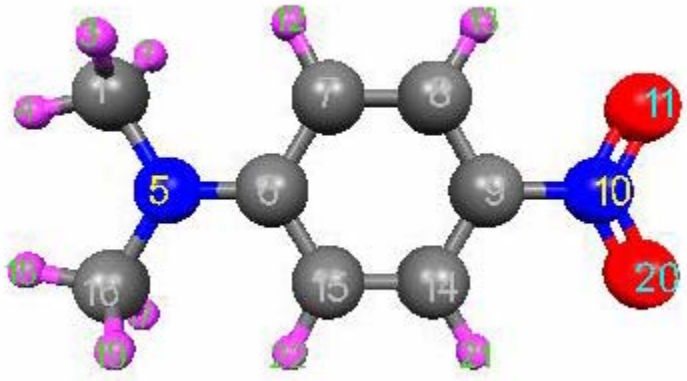

Figure 6.4: Numbering scheme used for DMPNA calculations

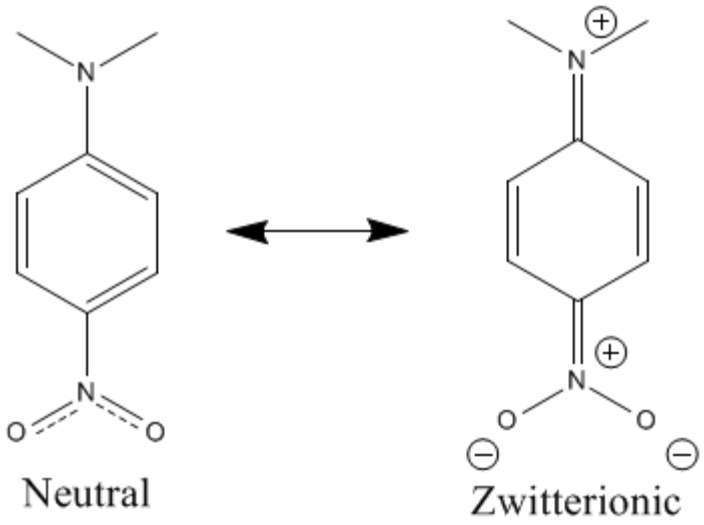

Figure 6.5: Two component basis states in the two state model for DMPNA.

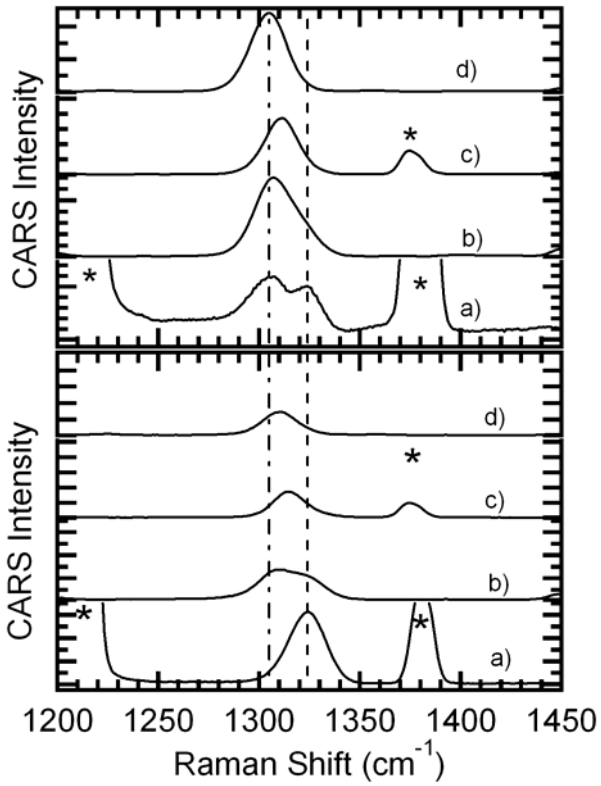

Figure 6.6: Ground (bottom) and excited+ground (top) CARS spectra zoomed in on the NO_2 symmetric stretch. Intensity axes have been normalized to the signal obtained at Δt_{exc} = 120 fs for each solvent with DMPNA in a) toluene, b) methanol, c) acetonitrile and d) propylene carbonate. Asterisks mark solvent bands and dashed line marks the frequency obtained for DMPNA/toluene in the ground state (1324 cm^{-1}) and the dashed-dotted line for the frequency obtained in the excited state for DMPNA/PC (1304 cm^{-1}).

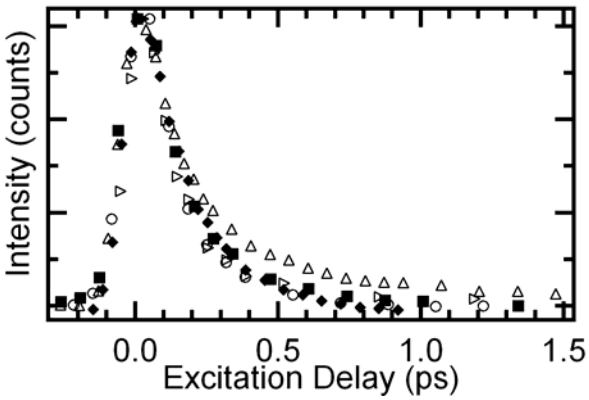

Figure 6.7: CARS Intensity dynamics of the 1510 cm^{-1} band in the excited state of DMPNA (top triangles: Ethylene Glycol, circles: acetonitrile, diamonds: methanol and right facing triangles: propylene carbonate). All solvents shown show similar timescales with a slightly slower decay time observed in ethylene glycol.

Table 6.1: List of solvents used and resultant NO_2 symmetric stretch frequencies in ground and excited state (Need help on this name….)

Solvent	NO_2 freq. ground	NO_2 freq. excited	Difference	$\pi^{a,b}$
BMIM-BF4	1311	1307	-4	0.99
Prop. Carb.	1310	1304	-6	0.83
Acetonitrile	1315	1311	-4	0.66
Methanol	1315	1307	-8	0.60
Toluene	1324	1306	-18	0.49

[a] BMIM-BF4 polarity parameter obtained from Matsumoto, H.; Yanagida, M.; Tanimoto, K.; Nomura, M.; Kitagawa, Y.; Miyazaki, Y. *Chem. Lett.* **2000**, 922. [b] Other solvents polarity parameters obtained from Horng, Maroncelli etc *J. Phys. Chem.* **1995**, 99, 17311.

Table 6.2: Calculated bond lengths (BL in Å), dipoles (in Debye), NO_2 symmetric stretch frequency (in cm^{-1}) and experimental dielectric constant employed in the PCM calculations

Solvent	C5-N6 BL	C6-C7 BL	C7-C8 BL	C8-C9 BL	C9-N10 BL	N10-O11 BL	Dipole (D)	NO2 Freq.	Dielectric Constant
Gas	1.368	1.419	1.381	1.393	1.453	1.230	8.55	1342.76	0
Cyclohexane	1.364	1.424	1.382	1.398	1.440	1.236	10.32	1331.01	2.023
Toluene	1.362	1.424	1.381	1.399	1.438	1.237	10.66	1327.14	2.379
Acetone	1.355	1.428	1.378	1.403	1.425	1.243	12.96	1303.8	20.7
Methanol	1.354	1.428	1.378	1.404	1.424	1.243	13.11	1302.81	32.63
Acetonitrile	1.354	1.428	1.378	1.404	1.424	1.243	13.14	1302.61	35.94[a]
Water	1.354	1.428	1.378	1.404	1.423	1.244	13.27	1301.84	78.39

[a] taken from *Chem. Phys.* 331, **(2006)** 142, remainder of dielectrics employed as pre-set in GAMESS.

Table 6.3: Calculated Raman active frequencies (gas phase, in cm^{-1}) for DMPNA in the gas phase and selected PCM solvents.

Solvent	NO_2 Sym. Stretch Freq	NO_2 Bend	Ring ip CH Bend+C-Nitro	Ring Stretch 19a'+C-N5	C=C ring stretch
Gas	1342.76	861.59	1124.31	1536.04	1632.84
Cyclohexane	1331.01	858.99	1134.85	1541.34	1641.93
Toluene	1327.14	858.40	1135.03	1541.12	1641.40
Acetone	1303.80	853.65	1136.43	1540.19	1639.47
Methanol	1302.81	853.29	1136.55	1540.18	1639.42
Acetonitrile	1302.61	853.22	1136.57	1540.23	1639.40
H20	1301.84	852.87	1136.61	1540.20	1639.43

CHAPTER 7: CONCLUSIONS

The development of fs/ps CARS was detailed in chapter 2 where it was shown that by simply pulse shaping the ω_3 CARS electric field, the experimentally outputted signal transforms from complex and difficult to analyze into a more amenable and easily acquired result. This change is particularly important because of the length of time required to take a single spectra in the purely femtosecond time domain due to the requirement of scanning with very small steps the entire dephasing time of the signal as well as the requirement that some knowledge already exists as to what the real frequencies are. The fact that only difference frequencies are measured in fs CARS (rather than the fundamental frequencies themselves) makes it very difficult to utilize in the excited state of molecules with several Raman active modes. Additionally, it was shown that this technique can reach low frequency regions, currently unavailable to femtosecond IR studies. The technique retains all of the benefits of CARS which include the background free nature, coherent output beam for rejecting fluorescence, as well as the very controlled energetic scheme typical of all four wave mixing processes. By implementing a sinc like ω_3 pulse, it was shown that non-resonant signal could be removed by positioning the max intensity of the ω_3 after the first two CARS electric fields.

In chapter 3, the basis for ultrafast time-resolution and increased spectral resolution of fs/ps CARS was detailed. At the "minimum" non-resonant position it was shown that experimental resolution is improved over that obtained by spontaneous Raman or conventional ps CARS (which measure 2Γ) and becomes more similar to 1.2Γ. This increased resolution allows for better resolution of close lying peaks (as was the case of the

hydrogen bonded/non-hydrogen bonded components seen in the excited state of C153, chapter 4). Because of the complex interaction of light fields with the same frequency and the interference generated, this improved resolution can simplify analysis of the experimental data as well as reduce the interference seen in outputted CARS spectra. It was experimentally shown that the position of the ω_3 pulse should be carefully controlled (using a sinc pulse) since positioning the max intensity of the ω_3 field to late after the first two CARS fields can result in lineshapes that are quite difficult to interpret. The time resolution was shown to depend on the cross correlation of the excitation pulse and first two fields of the CARS pulses (fs in duration in fs/ps CARS). This was shown explicitly for DMPNA in acetonitrile with an excited state lifetime of ~600 fs where, monitoring the intensity dynamics, the outputted CARS signal was a direct convolution of a 540 fs decay after instantaneous rise with the instrument response function of 125 fs.

In chapter 4, the first application of the fs/ps CARS probe to the excited state was performed on the excited state of Coumarin 153. The long lived excited state showed significant Raman intensity in several bands, most notably a C=O+C=C vibrational mode in the 1670-1690 cm^{-1} region. It was shown that the frequency of this mode was different in alcohols than aprotic solvents which led to the conclusion of a long lived hydrogen bonded structure in the excited state with an energy spacing of ~13 cm^{-1}. High resolution experiments in alcohol solvents were performed to elucidate the early time dynamics of this region. The resulting fs/ps CARS spectra revealed a complex early time behavior with the non-hydrogen bonded complex dominating initially but a slow rising hydrogen bonded component rising with a relatively slow time constant. At long time, the hydrogen bonded

component clearly dominates but the free component still exists, suggesting an equilibrium condition at later times.

Of particular interest in the case of C153 was the behavior of the intensity growth observed in the fs/ps CARS experiments. Unlike all other molecules studied in our lab, C153 had exceptionally slow rise times for all modes observed. Chapter 5 attempted to address the issue behind this slow growth and while not completely free of some speculation determined that excess energy does play some role in the observed dynamics. This was discovered by using three similar coumarin dyes with identical solvent systems (C153, C35, and C102). The growth time of the CARS signal steadily decreased as the amount of excess excitation energy was removed. It was clear that excess energy could not be the only reason behind this because of the case of C153 in non-polar cyclohexane which returned dynamics exactly predicted by the transient gain experiments (and hypothesized to be correct for all solvents). A large amount of excess excitation energy was still applied in this case, so it was hypothesized that the solvation timescales have some role in this behavior. Two particular focuses were on the fact that the rise times seemed to be related to longer known timescales in these solvents from other experiments and some theoretical work on the effect of molecular dipole changes on the dynamic behavior of hyperpolarizabilities. It was hypothesized that in the case of C153 in polar solvents, the hyperpolarizability (and thus CARS signal) had a non-constant behavior that mirrored the solvent response and resulted in slow rising signal.

In chapter 6, the application of fs/ps CARS to a simple push-pull charge transfer molecule was undertaken to determine the changes in excited state structure and provide insight into more complicated push-pull chromophores studied in our laboratory. It was

shown in the ground state via calculation and experiment that the NO_2 symmetric stretch could be a good indicator of solvent polarity and followed a well defined behavior consistent with increasing the zwitterionic character of the molecule with respect to the neutral case. The obtained excited state spectra generated an excited state lifetime of approximately 500-600 fs in each solvent irrespective of solvent viscosity. The spectra show a downshifted NO_2 symmetric stretch in the excited state but resulted in nearly the identical frequency in the solvent range from toluene to more polar solvents. This suggests that the excited state does not have the same mixture of zwitterionic versus neutral conformations and instead resembles a very polar ground state structure which can be thought of as considerably zwitterionic. It was discovered that shortly after internal conversion to the ground state that a recovery of excited state like frequencies occurred. This recovery suggests that the two states (excited state and hot ground state) are very similar in structure and may offer insight into the fast internal conversion.

ACKNOWLEDGEMENTS

It goes without saying that none of this work would even be possible without the support and direction of my major professor, Dr. Hans Stauffer. From the first days when our laser table was sparsely populated with optics to its current state so complex that it seems to overwhelm visiting students, our research has expanded and is being applied in exciting ways to molecules that have quite interesting behaviors (even if we don't always understand those behaviors!). I can genuinely say that there were very few days I walked away thinking I did not learn something useful, whether it came from our spirited discussions in group meetings to what makes a good poster. It has been a pleasure working here for the last four years and the guidance and helpful suggestions you have provided. I am grateful for being introduced to so many different phases of research, from designing LabView code to learning every little nuance about femtosecond laser systems to Igor macroing and the personal dread of mine, CorelDraw and curvy lines!

My gratitude also goes out to other members of my committee: Dr. Mark Gordon, Dr. Xueyu Song, Dr. Victor Lin, and Dr. William Jenks. This group of excellent scientists offered a good deal of insight and guidance into my research as well as helping to make the bureaucracy of scheduling things like final defenses and orals as painless as possible.

I would like to personally thank and acknowledge Dr. Gordon for instilling in me an excitement for the use and application of GAMESS to solving chemically relevant problems. I can honestly state that attacking chemical questions from both sides, experiment and computationally, has been one of the most enjoyable and fruitful activities of my graduate career and look forward to continuing it into the future. A special note must also go out to Dr.

Mike Schmidt who responds to what I felt a large amount of clueless emails sent on my part to try and sort out any issues I might be having using calculations in GAMESS, from CIS vectors issues to TDDFT! The depth of knowledge you seem to have regarding the code in GAMESS is just shocking to me, I cannot state enough how many times I might have given up trying to accomplish a particular calculation without the advice of both Dr. Gordon and you.

I cannot thank enough my fellow lab mates for the years (literally!) of time in the trenches! Most notably, I am grateful for the early years of my research when we were just trying to figure out all the fine details about the best way to setup and run our experiments. I would like to thank Dr. Abhijit Chakraborty, our first post-doc, for all of the discussions and being there while we moved forward with our experiments. My coworker and wife, Beth Prince, who has been absolutely perfect company in all the ups and downs of graduate research. I could not have done this without your support, discussions, organization and most of all, amazing persistence in painting everything as glass half full when I would say it was half empty. Also, our second post-doc, Dr. Mikhail Slipchenko, who had an amazing ability to make "stuff" work when it seemed like it wouldn't. Finally, our younger grad students in the group, Alex Blom and Ji Hyun Jun, for their hard work in picking up in the middle projects that needed to get done.

Finally, I would like to thank all of the faculty members I have been a teaching assistant for, for providing me so many unique and insightful perspectives on teaching undergraduates. It should also be noted the amazingly organized and helpful people in the chemistry department who "get things done", for someone as disorganized as myself I can only say it would be a lot harder without all of your efforts.